Wheel Spinning of Fibres for Wound-care Applications

A thesis submitted to the University of Manchester for the degree of

Doctor of Philosophy

in the Faculty of science and engineering

2022

Zhongda Chen

Department of materials, School of natural science

List of contents

List of figures

List of tables

Abstract

Wet spinning has been developed as one of the most mature technologies in the textile industry. Recently, it draws increasing attention from academia, especially in fabricating fibres for various advanced materials.

In this thesis, a novel “wheel spinning set-up” based on wet spinning technology has been designed and developed. The key factor for the wheel spinning machine (WSM) is to utilize the fluid to draw and twist the fibre in situ, which enables fibre a higher mechanical performance and unique surface morphology.

Wound is the issue that people often encounter in our daily life. The way to heal wounds timely and efficiently is the same goal for both patients and researchers. In the last decade, there are over 10,000 research reports regarding wound dressing development and design. However, little researches focus on the improvement of wound care and wound management.

This thesis also discussed the development of wound-care dressing materials via the WSM. Firstly, a wheel-spun alginate fibre has been fabricated and demonstrated its higher mechanical performance. It has advantages over the traditional wound dressing, regarding the knitting structure of wound dressing that enables patients to have a more comfortable and efficient healing environment. Secondly, a wheel-spun alginate-silk fibroin composite fibre has been fabricated and provided a controllable vascular endothelial growth factor (VEGF) release ability for better healing of the actual wound.

In conclusion, the wheel-spinning technique presented in this thesis provided an innovative and potential way to develop wound-care materials for an advanced wound healing process.

Declaration

No portion of the work referred to in the thesis has been submitted in support of an application for another degree or qualification of this or any other university or other institute of learning.

Copyright statement

The following four notes on copyright and the ownership of intellectual property rights must be included as written below:

i. The author of this thesis (including any appendices and/or schedules to this thesis) owns certain copyright or related rights in it (the "Copyright") and s/he has given The University of Manchester certain rights to use such Copyright, including for administrative purposes.

ii. Copies of this thesis, either in full or in extracts and whether in hard or electronic copy, may be made only in accordance with the Copyright, Designs and Patents Act 1988 (as amended) and regulations issued under it or, where appropriate, in accordance with licensing agreements which the University has from time to time. This page must form part of any such copies made.

iii. The ownership of certain Copyright, patents, designs, trademarks and other intellectual property (the "Intellectual Property") and any reproductions of copyright works in the thesis, for example graphs and tables ("Reproductions"), which may be described in this thesis, may not be owned by the author and may be owned by third parties. Such Intellectual Property and Reproductions cannot and must not be made available for use without the prior written permission of the owner(s) of the relevant Intellectual Property and/or Reproductions.

iv. Further information on the conditions under which disclosure, publication and commercialisation of this thesis, the Copyright and any Intellectual Property and/or Reproductions described in it may take place is available in the University IP Policy (see http://documents.manchester.ac.uk/DocuInfo.aspx?DocID=24420), in any relevant Thesis

restriction declarations deposited in the University Library, The University Library's regulations (see http://www.library.manchester.ac.uk/about/regulations/) and in The University's policy on Presentation of Theses

Acknowledgments

The work presented in this thesis relates to an interdisciplinary project which was completed in the University of Manchester. This project could not be accomplished smoothly without the support of so many people.

First, and most of all, I would like to thank my PhD supervisor Prof. Henry Yi Li, for his expertise, assistance, guidance, and patience throughout the process of writing this thesis. He leads me to the right directions and guides me to think independently. I am extremely grateful for the opportunity to do the research and it was a great privilege and honor to work and study under his guidance. I would also like to thank him for his friendship, empathy, and great sense of humor. I have achieved so much in the past four years at the University of Manchester, not just academically. I cannot express enough thanks to my supervisors, without you, I could never have reached this level of success.

In addition, I am eternally grateful to my co-supervisor, Dr. Olga Tsigkou, for her enlightening guidance and valuable helps. I have learned so much from her comments and encouragement over the years. I really enjoy and cherish my research period with her.

I would like to express my eternal appreciation towards my wife, Mrs. Xiaowen Peng, for her all-unconditional supports and patience, especiallyat the stage I was infected by the COVID virus. Thank you for being ever so understanding and never-ending motivations I've been getting all this while.

I would like to sincerely thank Prof. Julie Gough and Prof. Sarah Cartmell for their valuable suggests on the research plan. My great thanks give to Dr. Louise Carney, Dr. Li Jiashen, Dr. Patrick Hill, Dr. Andrij Zadoroshnyj, Ms. Marie O’Brien and Ms Jasmine Fernley for their help

from experimental support.

I am grateful to all of those whom I have had support and encouragement from during the last four years. They are Dr. Jun Song, Dr. Kewen Pan, Mr. Yumin Xia, Dr. Lulu Xu, Mr. Yangyang Fan, Dr. Muhammad Umar, Dr. Lu Jin, Mr. Zekun Liu, Mr. yangpeiqi Yi Mr. Zhangchi Liu and Miss. Sirui Yao.

Last but not least, I give my most appreciation to my parents and all family members for their generous supports to my PhD study. Their understanding and unconditional love are the source of my strength to complete my PhD study.

List of Publications

1. **Chen, Z.**, Song, J., Xia, Y., Jiang, Y., Murillo, L.L., Tsigkou, O., Wang, T. and Li, Y., 2021. High strength and strain alginate fibers by a novel wheel spinning technique for knitting stretchable and biocompatible wound-care materials. ***Materials Science and Engineering: C***, p.112204.
2. J. Song. [1], **Z. Chen.** [1], Z. Liu., Y. Yi., O. Tsigkou., J. Li., Y. Li., 2021. Controllable release of vascular endothelial growth factor (VEGF) by a novel wheel spinning alginate/ silk fibroin fibre for wound healing. ***Materials & Design***: 110231.
3. **Z. Chen.**, Murillo, L.L. Xu, L., Z. Liu., H. Zhai., Liu, J. Song., Y. Xia. Y. Fan. Y. Li., 2021 Collagen/cellulose - reduced graphene oxide sensor for arteriosclerosis monitor and chronic wound dressing for diabetics. (submitted to ***Biosensors and Bioelectronics***)
4. **Z. Chen.,** Y. Xia., Y. Li., Wheel Spinning technique for wet-spun fibre fabrication with unique drawing and twisting effect. (submitted to ***Materials & Design***)
5. Song, J., **Chen, Z.**, Murillo, L.L., Tang, D., Meng, C., Zhong, X., Wang, T. and Li, J., 2021. Hierarchical porous silk fibroin/poly (L-lactic acid) fibrous membranes towards vascular scaffolds. ***International Journal of Biological Macromolecules***, 166, pp.1111-1120.
6. Y. Xia., **Z Chen.** , Y. Li., Mechanical Properties Tests of Wet-spun Pure Alginate Filament and Yarns, in ***11th Textile Bioengineering and Informatics Symposium Proceedings***, 2018.
7. **Z. Chen**, Y. Li, O. Tsigkou, and X. Liu, "A Review on Skin Regeneration and Silk Fibroin," in ***10th Textile Bioengineering and Informatics Symposium Proceedings***, 2017.

Abbreviations

$(NH_4)_2SO_4$	Ammonium sulfate
Alg	Alginate
BMP-2	Bone morphogenetic protein-2
$CaCl_2$	Calcium chloride
CVDs	Cause cardiovascular diseases
DAPI	Diamidino-2-phenylindole
DMEM	Dulbecco's Modified Eagle Medium
EDX	Energy-dispersive X-ray spectroscopy
ELISA	Enzyme-linked immunosorbent assay
EGF	Epidermal growth factor
FFT	Fast Fourier transform method
FGF	Fibroblast growth factor
FE-SEM	Field emission scanning electron microscopy
FTIR/FT-IR	Fourier transform infrared
FDM	Fused Deposition Modelling
GF	Gauge factor
GO	Graphene oxide
GulA	Guluronic acid
HCAEC	Human coronary artery endothelial cells
HDF	Human dermal fibroblasts
HaCaT	Human keratinocytes
LSD	Least significant difference
LiBr	Lithium bromide
LEF-1	Lymphoid enhancer factor-1
M-6-P	Mannose-6-phosphate
ManA	Mannuronic acid
PBS	Phosphate buffered saline
PDGF	Platelet-derived growth factor
PLA	Polylactic acid
pPy	Polypyrrole
PW	Pulse wave
PWV	Pulse wave velocity
RHLC	Recombinant human-like collagen
rGO	Reduced graphene oxide
$\Delta R/R_0$	Relative resistance
rpm	Revolutions Per Minute
SEM	Scanning electron microscope
SF	Silk fibroin
NaAlg	Sodium alginate

Na_2CO_3	Sodium carbonate
Shh	Sonic hedgehog
TERM	Tissue engineering and regenerative medicine
TGF	Transforming growth factor
Tyr	Tyrosine
VEGF	Vascular endothelial growth factor
WAC	Water contact angle
WSM	Wheel spinning machine
XRD	X-ray diffraction

Chapter 1 Introduction

1.1 Overview of the thesis

This study examines the design and development of wheel spinning technique in wound-care applications. Wheel spinning technique is a fibre fabrication technique based on wet-spun technology. This chapter sets the background for this Ph.D. project and provide an overview for the subsequent chapters of this thesis.

The rest sections in this chapter is organized as follows: the section 2 is a background of wet spinning technology and wound-care applications. Then, the research motivations are found out based on literature review and presents in the section 3. Furthermore, in the section 4 and 5, several research gaps are summarized and transferred as objectives of this project. Each objective is solved at each separately chapter. Finally, the outline of the whole thesis is presented as a flow chart in the section 6.

1.2 Background

The injury of skin is the most common situation in everyone's life. However, the healing of wound leaking of guide will cause infection, fester, delay of healing and scar remaining. Also, for a chronic wound, the only function for current dressings is to protect the wound but cannot monitor the wound situation and complications for patients.

Wet spinning, a traditional technology from industry of textile, could produce by inject polymer solution into the coagulation bath to form the fibre. benefitted from its continuous production, fixed drawing rate and low-cost, it is a good method to fabricate micro fibres. However, it seriously relays on the accuracy fit of a series of rollers to drawing the fibre. Also, the surface

of fibre is usually flat and polymer's orientation is usually along the fibre's direction. Both of which caused the fibre cannot obtain various properties including mechanical strength, degradations behaviour, surface morphology and electric conductivity.

1.3 Motivations

This section discusses the three factors that motivate the project started and undertaken, which are summarized below:

(1) The wet spinning technology is a "developed technology" and has industrialized over more than 50 years. As a mature technology, it not been taken enough concern by the academic world recent years (Fig. 1.1).

(2) Wound-care process is always a crucial treatment need to be developed. Although wound dressing has been used by Ancient Egypt 3000 years ago, the developing of smart dressing and pursuing of a perfect healing process is unstopped. There are hundreds of researches undertaken every year.

(3) Smart textile is a new and vigorous research topic in the last few years. But less of them applied onto the wound-care area.

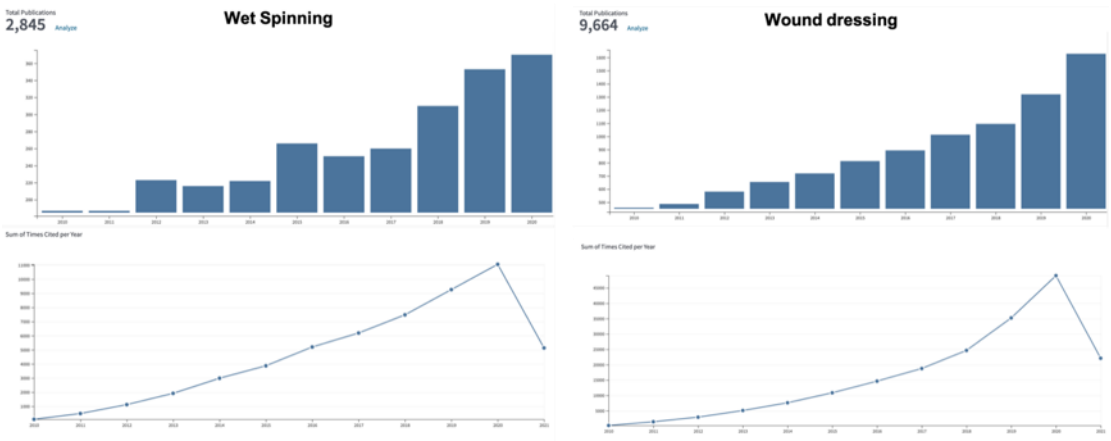

Fig. 1.1 Total of publishes and citations in SCI index of wet spinning and wound dressing (from web of science)

1.4 Research gaps

Based on the motivations and after a literature review for the aspect of wet spinning, wound healing, controlled release, natural materials, 2d materials and smart textile, the following research gaps are summarized:

(1) During the wound healing, how to guide the healing process need a comprehensive understand and review.

(2) The leaking of enough mechanical strength and unique structures of traditional wet spinning natural fibre cause its unable to be developed as a smart dressing. A new-design of fibre spinning technique is necessary.

(3) The relationship of parameter of fibre spinning and fibre mechanical strength need to study.

(4) The relationship of parameter of fibre spinning and growth factor release behaviour from fibre need to study.

1.5 Objectives

In order to fill the research gaps mentioned at 1.4, the following research objectives are developed:

(1) Have a literature review on wound healing process, how growth factors guides the wound healing process and controlled drug release systems.

(2) To development a unique wheel spinning machine, then analysis the mechanism of wheel-spun fibre's formation and compare their properties with normal wet-spun fibres.

(3) To fabricate a knitting structure alginate fibrous fabric as gentle wound-care dressing,

to provide a moisture environment for wound area. Also obtain a systemic study for the wheel-spun alginate fibre, including mechanical properties, degradation process and biocompability test. Give out the relationship between wheel spinning machine parameter setup and fibre's tensile and biodegradation properties.

(4) To fabricate an alginate-silk fibroin composite wheel-spun fibrous nonwoven mat as a growth factor (VEGF in is project) loaded wound dressing for actual wound healing. Also, build a systemic study for VEGF release speed and give out the relationship between wheel spinning machine parameter setup and fibre's VEGF release and biodegradation properties

1.6 Project significance and originality

This project focus on wound-care applications by using the fibre structure material made from the wheel spinning machine. The specific originally contributions are list below:

(1) A unique device setup call "wheel spinning machine" was developed and optimized

(2) By using the wheel spinning machine, fibre made from natural materials (alginate, silk fibroin and cellulose) could be fabricated with a high drawing rate and a unique self-twisting effect.

(3) A comprehensive theoretical analysis for the wheel spinning machine factors and the fibre drawing and twisting effect.

(4) Wheel-spun alginate fibre was knitted as fabric for wound dressing material.

(5) Wheel-spun alginate-silk fibroin fibre was fabricated for VEGF controlled release for actual wound healing.

(6) DoE was introduced to analysis the wheel spinning machine parameter and fibre

properties.

1.7 Thesis outline

In this project, I reviewed the wound healing process and related controlled release system, as a theoretical basis for the remaining parts, which presents in chapter 2.

Then, I state the design and development of the wheel spinning machine and presented the calculation of wheel spinning machine's drawing rate, twisting rate and fibre force analysis, which presents in chapter 3.

After that, I made 3 kinds of wound dressing material for different situations of wound healing. Both of them are made from the wheel spinning machine via different materials. The first is a knitting fabric general wound dressing made by pure alginate fibre, with better mechanical properties, biodegradation behaviour and biocompability, which presents in chapter 4. The second is a VEGF loading wound dressing made from alginate-silk fibroin composite fibre for actual wound, which presents in chapter 5.

This project's outline is presented as a flow chart, shown in Fig. 1.2.

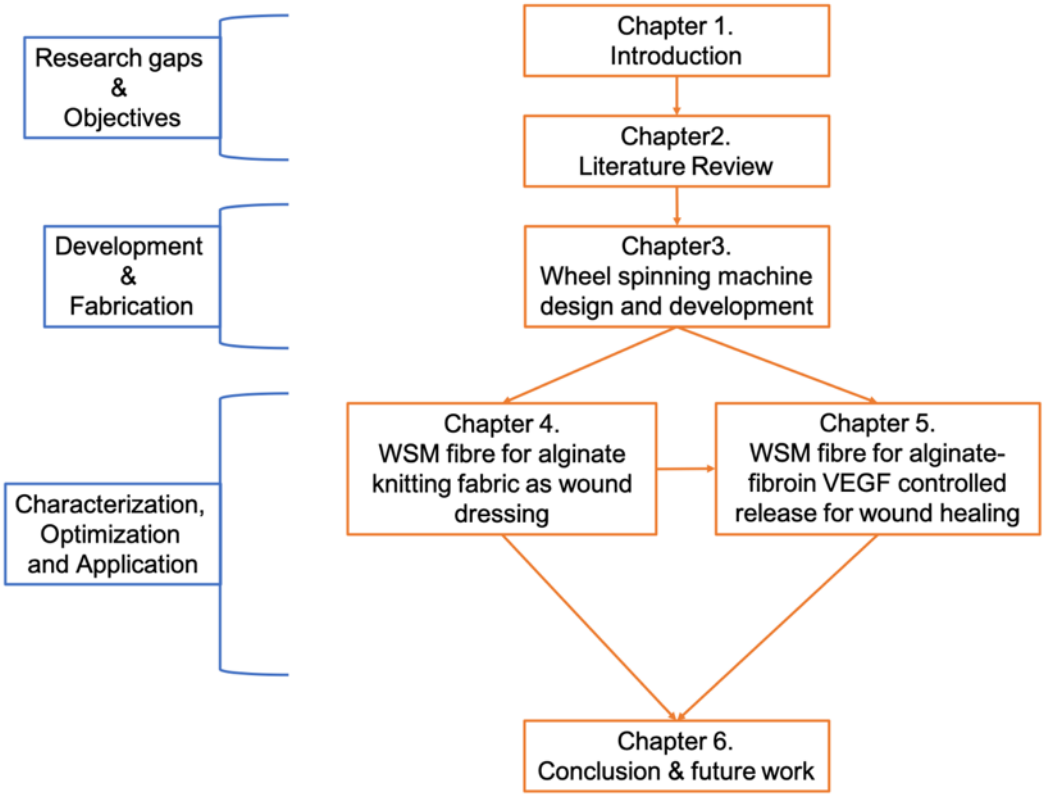

Fig. 1.2 Diagram of thesis outline

Chapter 2 Literature review

Sections 2.2.2, 4.1 and 4.2 of this chapter are directly cited from the following published work I co-authored:

Title: A review on skin regeneration and silk fibroin

Authors: Zhong-Da Chen, Yi Li*, Olga Tsigkou, Xu-Qing Liu

Journal: Proceedings of 10th Textile Bioengineering and Informatics Symposium (2017)

DOI: 10.3993/tbis2017: PP18-27

2.1 Background

This chapter presents an overview of research related to natural materials for fibre fabrication, the wet-spinning technique and wound healing across a range of disciplines. Fundamental theory, alongside previous contributions and my evaluations of these, is presented in this review. It is organized into three sections:

A. Literature related to certain various **natural materials** will be discussed in Section 2, including alginate, silk fibroin and cellulose.

B. Literature related to the **wet-spinning technique** will be discussed in Section 3, including its principle and biomedical applications.

C. Literature related to **wound healing and wound dressings** will be discussed in Section 4, including the healing process, dressing functions and the drug-delivery system.

The structure of this literature review is presented as a flow chart in Fig. 2.1.

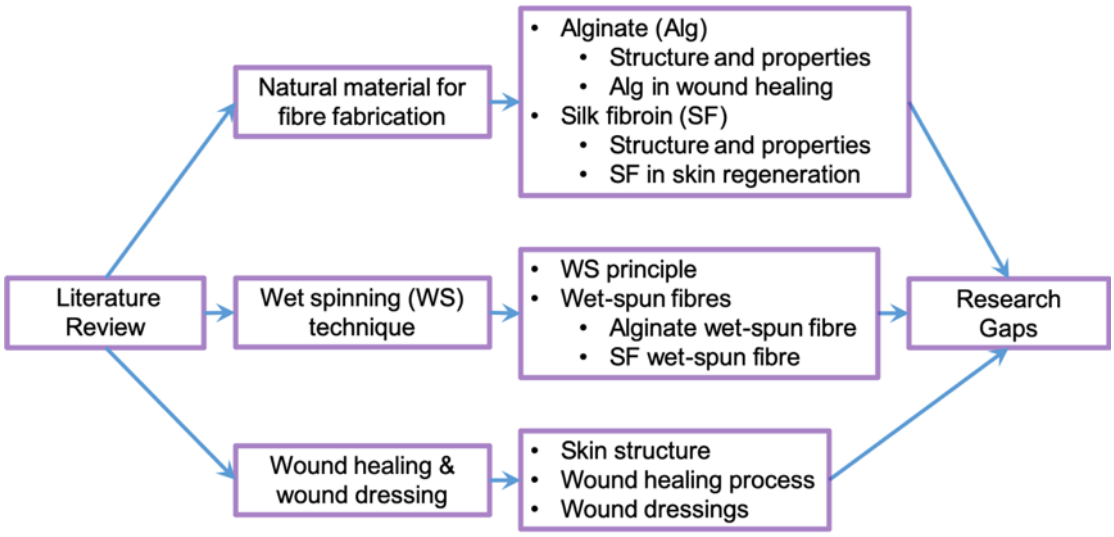

Fig. 2.1 Flow chart depiction of the literature review.

2.2 Natural materials for fibre fabrication

2.2.1 Alginate

2.2.1.1 Structure and properties

Alginate can be extracted from many types of brown algae, such as Laminaria digitata, Ascophyllum nodosum, and stems of Laminaria hyperborean[1]. Alginic acid was found, produced and patented by Stanford in 1881 and applied in the food, textile printing, medication, and paper industries, as well as many other novel end uses. Alginate exhibits a chain of (1,4) linked β-D-mannuronic acid (M) and α-L-guluronic acid (G) monomers [2] (Figure 2-2). These two monomers reveal a distinction at C-5 in stereo-chemical conditions[1]. These sugar acids are distributed in blocks and possess extensively varying proportions and sequences. The homopolymeric regions of M and G, known as M and G blocks, combine as an alternating structure. Typically, the blocks are composed of three different forms of polymer segments: GG, MM and MG residues, among which MG leads to hydrogels [3]. The proportion of M and G blocks, as well as the ratio of GG, MM and MG residues, could influence physical performance such as the degradation speed and drug-release rate of alginate [4–6]. This is caused by the difference among M and G blocks in the ability of binding the calcium ions. It has been reported that the G block swells slightly and forms a stronger gel, meaning that only a G block can take part in the intermolecular process with divalent cations, including Ca^{2+}, in order to form gels[7].

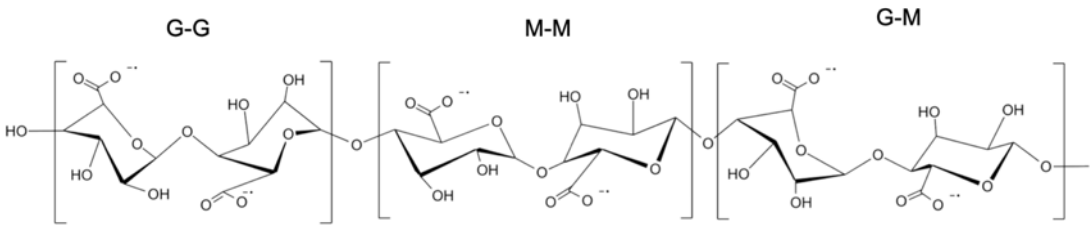

Fig. 2.2 The structure of α-L-guluronic acid (G) and β-D-mannuronic acid (M) monomers in alginate, and G-G, M-M and G-M blocks.

As a natural material, alginate is a kind of biocompatible and biodegradable polymer, which is also renewable and non-toxic[8]. Alginate was widely used in the manufacturing of wound dressings in the 1980s and approved at the second conference on medical textiles in 1999 [9]. However, the relatively high price, poor mechanical strength and chemical instability under alkaline conditions during bleaching have inhibited further development [10]. Recently, alginate has returned to the purview of researchers who have been applying physical modifications [11] and mixing it with other non-toxic materials such as graphene oxide and chitosan [12,13]. Biocompatibility is one of alginate's remarkable properties, such that it has been extensively applied in tissue engineering and other biomedical applications, especially for alginate-based fibre materials [14–20]. Although it is non-degradable in mammals, because of a lack of alginase [21], alginate can be extracted via ion-exchange reactions, in turn meaning that alginate is biodegradable.

2.2.1.2 Alginate in wound healing

Alginate also has swelling properties and can convert into a hydrogel form, creating a moist environment. Exploiting this property, it has recently been used in wound management as a novel content for developing 'moist-healing' products [22,23], as well as in regeneration medicine and drug delivery [23,24]. Beside the generation of a moist environment, the ion-exchange reaction

of alginate allows the dressing to absorb exudate from the wound [25]. Alginate fibres form a gel to prevent the wound from becoming dry, in turn enhancing the healing process and preventing scar formation [26]. When calcium ions are released into the wound, this stimulates platelet activation and blood coagulation [27]. Alginate dressings have good permeability concerning gas and water content, as they imitate natural skin, resulting in the wound remaining moist throughout the healing process [25].

2.2.2 Silk fibroin

2.2.2.1 Structure and properties

Silk fibroin (SF) is a kind of natural protein from the cocoon of *Bombyx mori* (domestic silkworm) (Fig. 2.3). In silk from a silkworm cocoon, SF accounts for about 70% and sericin about 25%. SF consists of 18 types of amino acid residue and shows no bioactivity [2-12,13].

Fig. 2.3 *Bombyx mori* and its cocoon.

The primary structure of SF includes three sub-units, namely, a heavy chain (H-chain), a light chain (L-chain) and a glycoprotein (P25). All of them connect with each other via a disulphide

bond. The molecular weight of SF is about 444,000, which includes about 391,000 for the H-chain, about 28,000 for the L-chain and about 25,000 for P25. The H-chain consists of 5,263 amino acid residues and the L-chain consists of 266 amino acid residues. Table 2-1 sets out the proportion of each type of amino acid within SF [28–34].

Table 2. 1 Proportion of each amino acid within native and regenerated SF[35].

Amino acid	Native (mol %)	Regenerated (mol %)
Asp	5.11	4.67
Thr	0.44	0.4
Ser	10.58	10.37
Glu	0.9	0.73
Gly	29.81	28.84
Aal	42.27	43.1
Val	0.88	1.17
Cys	N/A	N/A
Ile	0.41	0.43
Leu	0.41	0.44
Tyr	5.11	5.47
Phe	0.34	0.37
Lys	0.13	0.13
His	0.9	0.8
Arg	2.72	2.55
Pro	trace	0.53

2.2.2.2 SF in skin regeneration

(Cite directly from TBSI 2017)

SF composite material has been reported in relation to skin regeneration, as SF-alginate scaffolds sufficiently enhanced re-epithelization in a full-thickness rat wound model [36]. Otherwise, nanofibrous silk-chitin [37], silk-collagen [38], silk-elastin [39] and intermolecular cross-linked recombinant human-like collagen (RHLC) with fibroin[40] have also been applied successfully in skin repair, with these natural materials acting as cell scaffolds and displaying good biocompatibility. Shellac wax, beeswax and carnauba wax have been reported as successfully coating SF material, providing wound dressings with a hydrophobic surface[41] and protecting the wound from infection. Polyethyleneimine has been reported as having antibacterial properties when it was blended with an electrospinning fibroin scaffold[42].

SF material has been widely used in wound healing. It can be fabricated in various forms (e.g., matrix[36], microsphere, nanoparticle [43] and film or membranes [44], because SF material supports human keratinocytes and fibroblasts well[45]. In full-thickness burns, gelatine microspheres were impregnated with the antibiotic gentamycin sulphate, and the microspheres were then embedded in a SF matrix to fabricate GS/GM/SF scaffolds, which effectively inhibited injection during dermal regeneration[46]. SF coated with polypyrrole (pPy), via chemical polymerization, has been investigated, revealing that this method can improve mechanical resistance [47]. An SF electrospinning scaffold was also reported to improve vascular growth by using human aortic endothelial and human coronary artery smooth muscle cells [48]. An SF electrospinning scaffold is a kind of degradable material; it can be degraded 65% by protease

within 24 days [49] and fully degraded within 21 days in the case of an aqueous-derived scaffold [50].

Bioprinting technology has been applied for the fabrication of an 3D artificial extracellular matrix (ECM) for skin repair. Sha Huang et al. demonstrated that a 3D-printed artificial ECM made by a mixture of cells, epidermal growth factor (EGF) and homogenates could lead to sweat gland regeneration in a rat mould [51]. Dextran hydrogel scaffolds made by Guoming Sun and colleagues involving a mice mould showed an improvement in angiogenic formation [52]. Noting that scar reduction a significant task to undertake, Chouhan et al. [53] indicated that their SF mat functionalized with EGF could facilitate scarless healing treatment. This may be caused by EFG initiating the degradation of collagen I [54], while SF nanofibres can significantly inhibit TNF-α expression[55,56]. Otherwise, Ponrasu et al. reported their Isabgol (psyllium husk) and SF 3D composite scaffolds can accelerate cellular activity in order to heal wounds faster with minimal scar formation [57]. SF derived from various kinds of worm has been used for research purposes, such as by Baba et al., who documented that SF accelerates cutaneous wound healing, an effect which is enhanced by over-expression of RG sequence SF (TG-SF) [58]. Table 2.2 summarizes some weighted outcomes from 2016, while each of their achievements and limitations are listed on Table 2.3 [53,55–60].

Table 2.2 Some SF-fabricated wound dressings [53,55–60]..

Material	Morphology	Method	Antimicrobial way	Cell
SF nanofibers	Membranes	Thiol-maleimide coupling	Immobilized antimicrobial peptide (Cys-KR12)	Human keratinocytes (HaCaT) Human dermal fibroblasts (NHDF) Murine monocytes (Raw264.7)
SF/gelatine nanofibers	Mat	Electrospinning	Ceftazidime	Human skin fibroblast cells
SF fibre	Mat	Electrospinning	Coated ciprofloxacin hydrochloride	Full-thickness cut rabbit model HaCaT and NHDF cells
SF nanoparticles Sodium-carboxymethyl	Hydrocolloid dressing	Membrane grinding Ball milling	Exchange dressing	Second-degree burn rat model 3T3 fibroblast cells
Isabgol (psyllium husk) SF	3D scaffold	Freeze drying	Not mentioned	Full-thickness cut wound rat model
SF fibre	Nanomatrix	Electrospinning	Not mentioned	Second-degree burn rat model
Amorphous SF Transgenic worms Wild-type worm	Film	Not mentioned	Not mentioned	Full-thickness skin wounds on mice NHDF cells

Table 2.3 Achievements and limitations of SF-fabricated wound dressings [53,55–60].

Achievements/limitations
Significantly inhibited TNF-α expression
Only one-week antimicrobial activity retained at body temperature (37℃)
Good antibacterial effect
Drug-release activity highly depends on water
Functionalized with EGF and scarless healing tendency
The rate of drug release not even, up to 60% released within the first 10 h
Addition of SF nanoparticles enhances tensile strength and increases the density of collagen fibres and PCNA expression
Cannot close wound within three weeks
Enhanced fluid uptake ability with enough fibroblast attachment and good viability, causing dense collagen fibres and neovascularization
The ability of cell migration may not be great
Accelerates re-epithelialization and wound closure in burn wounds, with scarless wound healing by regulating TGF-β1 expression
No antimicrobiology method refers
Wound closure accelerates (transgenic worms), granulation tissue thicker and larger, and neovascularization promoted significantly (wild-type silkworm)
Not mentioned

2.3 Wet-spinning technology

2.3.1 The principle of wet spinning

The wet-spinning technique emerged in the 1930s and has been introduced into the textile industry for the fabrication of synthetic polymeric fibres including nylon, spandex and acrylic fibres. In short, wet-spun fibre is generated by extruding a polymer solution in a controlled manner through a nozzle into a corresponding coagulation bath[61]. The coagulating process for polymeric fibres is caused by polymer desolvation, due to a solvent/non-solvent exchange. Finally, a two-phase structure is formed from the original polymer solution with thermodynamical stability[62]. The two-phase structure comprises a polymer-lean phase and a polymer-rich phase under a critical composition. From this structure, a microporous morphology of the solidified polymer is formed. The morphology of the fibre's inner structure can be strongly affected by thermodynamic conditions and coagulation kinetics[62,63]. Pore size, geometry and distribution are regarded as changeable factors when controlling wet-spinning parameters, because these changes lead to different coagulating speeds at the surface of the fibre, in turn entrapping the solvent and non-solvent inside the fibre13-15. Beside this, other parameters including nozzle size, concentration of polymer and coagulation solution, additives, solution feed rate and winding velocity can affect the fibre's properties and morphology[63].

2.3.2 Wet-spun fibres

2.3.2.1 Wet-spun alginate fibre

Wet spinning is a mature and reliable method for the production of alginate fibre. A sodium alginate aqueous solution is extruded into a divalent ion coagulation bath (normally calcium

chloride), after which the insolvable calcium alginate forms the fibre. When sodium alginate is squeezed into a calcium chloride bath, the buckle of the glucuronic acid unit acts as a two-dimensional structure similar to a corrugated egg-shaped box, with gaps that can encapsulate and coordinate calcium ions. The structure of the egg-box dimer has been widely acknowledged and is presented in Fig. 2.4 [7,67–69]

Recently, to some extent, alginate-based biomaterials have been associated with the traditional wet-spinning method, which uses $CaCl_2$ or $MgCl_2$ to solidify the alginate and generate the gel-form materials[7,70–72]. Some newer techniques such as 3D printing and microfluidics have been introduced. However, studies on biomedical applications using alginate materials are more focused on functionality in terms of biodegradation, cell adhesion and drug release. Given the leak of any post-spinning drawing of the fibre and the tendency towards slow gel formation, the mechanical properties of these materials are relatively low level (breaking stress is about 500 kPa-10 mPa) [73–75]. Thus, for alginate fibre fabrication, how to enhance its tensile strength stills need more interrogation.

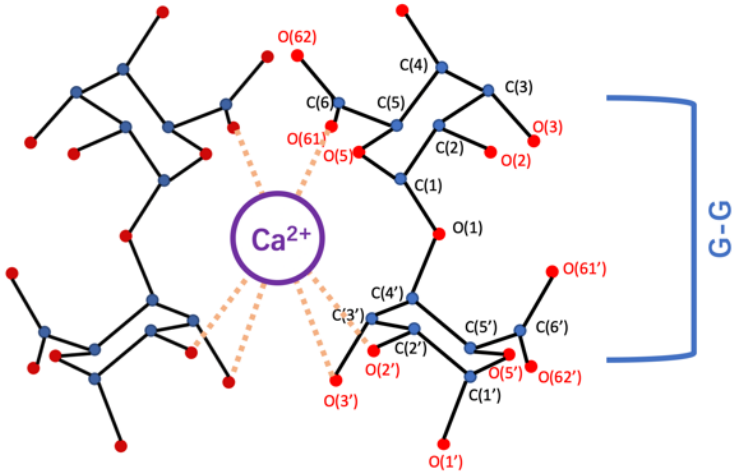

Fig. 2.4 The egg-box dimer structure of alginate.

2.3.2.2 Wet-spun SF fibre

As early as 1960, in the first public report of artificial spinning with regenerated silk protein, mulberry silk was dissolved in a high-concentration magnesium nitrate solution and, after dialysis and concentration, wet spinning was performed in a coagulation bath of saturated ammonium sulphate solution, where the strength and strain for the regenerated SF fibres on breaking were 0.28 GPa and 20%~25% [76,77].

In the late 1980s, researchers used phosphoric acid as a solvent to dissolve mulberry silk, after which it was subject to wet spinning in regenerated SF solution in a coagulation bath mixed with ammonium sulphate and sodium sulphate solution. By investigating the additives in the regenerated SF solution, the coagulation bath composition and temperature, as well as post-stretching treatment and other factors, it was found that the maximum strength and strain of the obtained regenerated fibroin fibres on breaking was about 0.23 GPa and 10%. However, the use of magnesium nitrate or phosphoric acid as a solvent for silk was reported to cause severe degradation of SF, which is why such solutions have rarely been used as spinning dope in subsequent studies [78].

Using lithium bromide (LiBr)/water-ethanol/water as a solvent, a regenerated mulberry SF solution with a concentration (mass fraction) of 16% or 20% can be obtained, which is close to the concentration of the natural-spinning original solution from a silkworm. By using methanol, ethyl ferment and isobutanol as coagulation baths, the regenerated SF salt solution is directly spun without dialysis. After post-stretching in air and water, various regenerated SF fibres have also be produced. Their strength and strain on breaking were about 0.12 GPa and 11% [79,80].

It has also been reported that regenerated SF solution obtained by dissolving $Ca(NO_3)_2/H_2O/CH_3OH$ is dialyzed. When salt-free regenerated SF aqueous solution is obtained, then freeze-dried and dissolved in a 95% solution of formic acid or anhydrous trifluoroacetic acid, regenerated SF solution with a highest concentration of 13% was obtained. When pure methanol was used as a coagulation bath for wet spinning, and after a certain period of post-drawing treatment, the strength and strain for the obtained regenerated SF fibres on breaking could reach 0.90~0.95 GPa and 18%~29.3%, with Young's modulus around 33 GPa, far exceeding that of natural silk fibres (0.57GPa, 26% and 11GPa, respectively). Noting that this has never been repeatedly prepared by future generations, the reported fibre diameter (4.3-12.1 d) is much larger than that of natural silk (0.95 d). This result could be considered as a miscalculation [77].

The main process for the wet spinning of regenerated SF is to inject the spinning stock solution into the coagulation bath; and through the double diffusion of water in the stock solution and the solvent in the coagulation bath, the regenerated silk protein is aggregated and precipitated from the stock solution, before being solidified to form primary fibres. To improve the mechanical performance of the fibres, firstly, as a basic substance, the molecular weight of the regenerated silk protein should be as large as possible; secondly, on the premise of ensuring that the solution properties are stable and have proper mobility, the concentration of the regenerated silk protein spinning stock solution should be slightly higher. Moreover, whether the coagulation solution is an inorganic salt system or an organic solvent, the effect of directly forming the fibre in the coagulation bath will not result in good tensile properties. Finally, and more importantly, the post-drawing process can, to a large extent, improve the mechanical

properties of regenerated SF fibres.

The function of the coagulation bath is to precipitate the regeneration of SF through a difference in solubility in order to form a certain amount of B-sheet structure in situ. In this process, factors such as the type and temperature of the coagulation bath, the type and concentration of the spinning dope, and the spinning speed, which affect the double-diffusion rate of the solvent and its difference, will determine the morphology and properties of the as-spun silk protein fibres. Due to the high degree of entanglement for the internal SF molecular chains and the disordered arrangement of the folded structure, the primary fibres are often brittle. Therefore, post-stretching is performed to increase the orientation of the molecular chains and the B-fold region, thereby improving the regenerated silk protein. By changing the orientation of the molecular chains, the mechanical properties (especially toughness) can be improved. At the same time, post-drawing also reduces fibre diameter.

2.4 Wound healing and wound dressing

2.4.1 Skin structure

(Cite directly from TBSI 2017)

Skin coats the entire surface of human body; it is the biggest organ, contributing 16% of the whole body's weight. Skin consists of the epidermis layer, the dermis layer, subcutaneous tissue (hypodermis) and cutaneous appendages including sebaceous glands, sweat glands, hair and fingernails (Fig. 2.5).

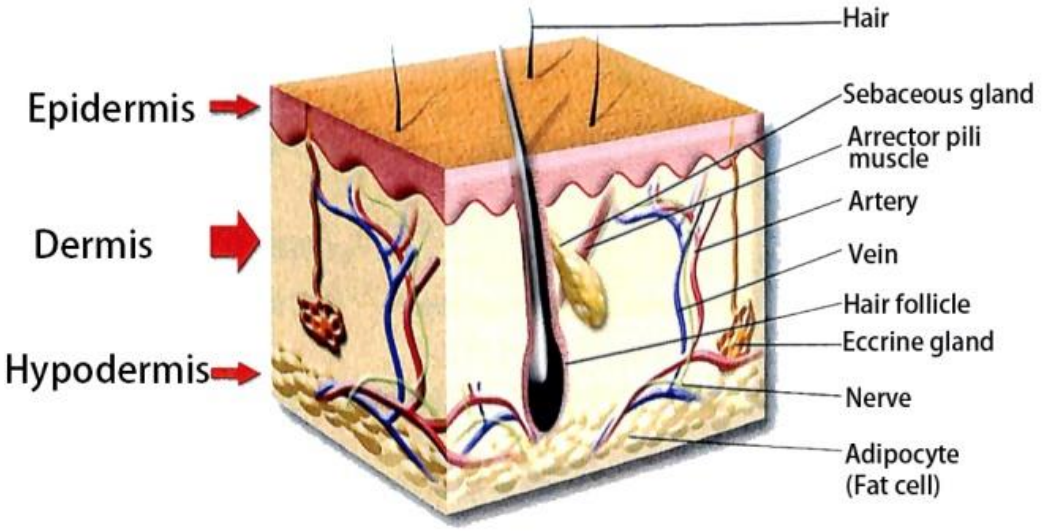

Fig. 2.5 The structure of skin.

2.4.1.1 Epidermis

The epidermis, located on the surface of skin, has several strata: stratum basale, stratum spinosum, stratum granulosum, stratum lucidum and stratum corneum. This structure is shown in Figure 2. All of strata consist of keratinocytes with different morphologies which take part in keratinization and produce keratin, with the stratum corneum consisting of dead keratinocytes while its thickness depends on specific parts of the skin (usually 40-50 layers on the palm and five-10 layers on the face). Usually, it will take 14 days for the stratum corneum to move from the stratum basale and then to the stratum granulosum, and another 14 days from the stratum granulosum to the stratum corneum.

Melanocyte, Langerhans cells and Merkel cells exist in the epidermis. Melanocyte is usually located in the stratum basale, affects the colour of skin and has the function of providing ultraviolet-ray resistance and protecting deeper tissues. Melanocyte is a kind of transparent cell with plenty of dendritic apophysis and contains many melanosomes produced by the Golgi complex, which can form a compound with melaningeanule as a result of using tyrosine (Tyr). Melaningeanule migrates from the melanosomes to the dendritic apophysis.

A Langerhans cell is a type of immunocompetence cell which originates from macrophagocyte. It is usually located in the strata basale and spinosum and occupies about 10% of all cells in the former stratum. It has a similar function to T lymphocyte which focuses on recognizing IgG, IgE, FcR and C3b receptors and MHC III, CD4, CD45 and S-100 antigens, meaning that it can play an important role in contact allergy, antiviral infection and allograft rejection.

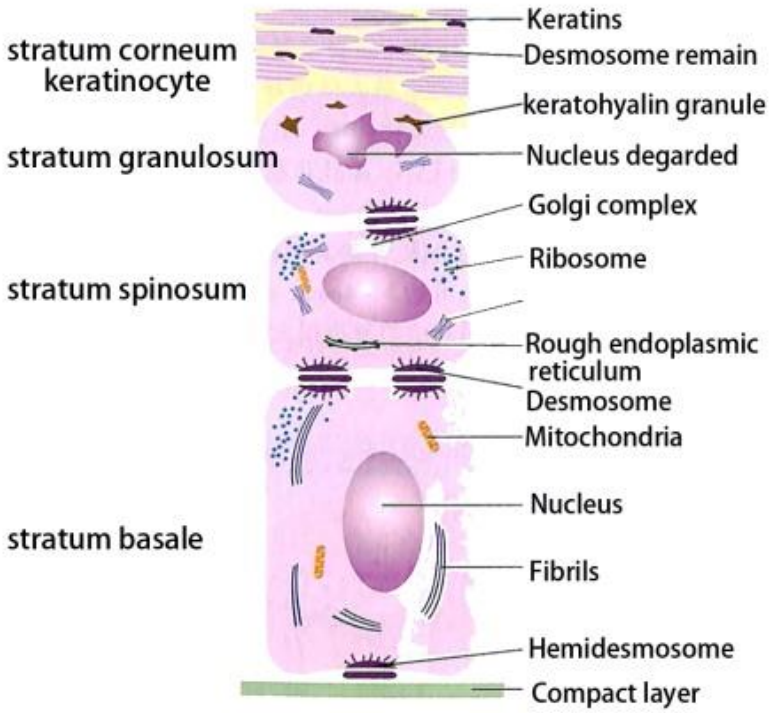

Fig. 2.6 Structure of the epidermis.

Merkel cells are only located in the stratum basale and never migrate. Their functions are, to some extent, unclear, but they are often considered to have a close connection with sense, because their density is relative higher in sensitive areas such as fingertips or apex nails. In these areas, nerve fibre loses its myelin sheath and connects with Merkel cells by a chemical synapse, known as a Merkel cell-neurite complex. Some studies have revealed that Merkel cells acquire a kind of paracrine and are involved in the regulation of keratinocytes, cutaneous

appendages and nerve fibre in skin.

2.4.1.2 Dermis

Plenty of blood vessels, lymph vessels and nerves pass through the dermis which has two layers, namely, a papillary layer and a reticular layer; although there is no obvious boundary between them. The dermis is a kind of tight connective tissue and consists of fibre, ECM and cells. The papillary layer has several embossments and can connect well with the stratum basale in the epidermis and help it to obtain nutrition from blood vessels in the dermis. The reticular layer is under the papillary layer and is the main part of the dermis.

Fibres in the dermis are fabricated from collagen fibres, reticular fibres and elastic fibres. The diameter of collagen fibres is between 70-140 nm and increases along with the depth of the dermis. These fibres have higher toughness and strength, but are less elastic: reticular fibres, comprising immature Type III collagen fibres, have a fibre diameter of around 40-65 nm and are typically distributed in the papillary layer. Elastic fibres consist of elasticin and microfibrils whose diameter is between 1 and 3 nm, distributed in the reticular layer and entwined around collagen fibres, meaning that the reticular layer has higher elasticity.

The matrix in the dermis used to fill the space between fibre and cells is mainly proteoglycan. The structure of proteoglycan has many micropores which allow water, electrolyte, metabolite and nutrition pass, but large matter such as bacteria will deposit and facilitate macrophage to clear it. Immune responses within skin typically happen in the dermis. This is because most cells (e.g., macrophage, T-cell, endotheliocyte, fibroblast and mastocyte) that join in the skin's immune response distribute capillaries to the papillary layer. The interaction of these cells as well as the cytokines produced by these cells plays an important role in the repair of inflammatory injury.

2.4.1.3 Hypodermis, cutaneous appendages, nerve, vessel and muscle

The hypodermis is a part of the skin which consists of loosened connective tissue and fat, blood

vessels, lymph vessels, nerves and sweat glands. Besides this, the hypodermis can retain human heat and buffer mechanical stress. Cutaneous appendages include eccrine glands, apocrine glands, sebaceous glands, hair and nails. These are both accessories of skin and aids to cooling skin (sweat glands), protecting skin (hair and nails) and lubricating skin (sebaceous glands).

There are two kinds of nerves in skin: one is for motion, and another is for sense. Motor nerves include the cholinergic nerve and the adrenergic nerve, which are for the secretory cells in the eccrine glands and the epithelial cells in the arrector pili muscle, apocrine glands and blood vessels, respectively. Sensory nerves include free nerve endings and sensory corpuscles, mainly distributed under pileous skin and glabrous skin, respectively.

The blood vessels in skin can regulate body temperature by contraction and during diastole. They combine a network which is parallel to the epidermis involving continuous endothelial cells. Blood vessels have three layers, meaning they have poor permeability. In contrast with blood vessels, lymph vessels have one layer consisting of endothelial cells and fibre, such that immune cells could exit lymph vessels more easily. The arrector pili muscle is the most common muscle in skin, which are located near the hair follicles and can make hair stand on end when people feel cold.

2.4.2 Wound-healing process

(Cite directly from TBSI 2017)

At the cell lever, the proliferation of cells, to a large extent, is affected by the extent of cell stimulation. Of utmost importance is to promote motionless cells in the cell cycle. When injury happens, growth factors will release and stimulate cells from the same germinal layer. Skin cells are all derived from the ectoderm. For skin regeneration, numerous cell factors, such as EGF, fibroblast growth factor (FGF), transforming growth factor (TGF) and vascular endothelial growth factor (VEGF) take part in the promotion of cell growth[81]. Chalone such as

angiostatin and endostatin can inhibit the growth of capillaries. Inhibition of the epidermis is mainly through contract inhibition: when epidermises contact each other, proliferation stops.

When a burn happens, the regeneration of skin starts. Firstly, blood coagulation happens in the injury area, then inflammation appears which causes congestion and exudation of neutrophils. Sometimes, incrustation resulting from collagen and blood clots covers the surface of wound to protect it. A blood clot is caused by platelets embedded in a mesh of cross-linked fibrin fibres, together with plasma fibronectin, vitronectin and thrombospondin [82]. Then inflammatory cells are recruited in the wound site, mainly neutrophils and monocytes. During the recruitment of inflammatory cells, molecular changes take place on the surface of the endothelial cells lining the capillaries, while the selectins and the β2 class of integrins are expressed to allow for adhesion. Further, leukocytes slow down, while diapedesis occurs, which causes neutrophils to crawl out from among the endothelial cells into the extravascular space and arrive at the wound site in a few minutes [83,84]. Regarding injuries, monocytes enter the injured tissue, then grow and transfer to macrophagocytes, which is a response to the clearing of dead cells, in turn releasing some chemokines that can attract fibroblasts and epithelial cells to the injury area. Monocytes also release a chain of growth factors and cytokines[84]. Hübner et al. found that neutrophils can also provide some of the earliest signals to activate local fibroblasts and keratinocytes [85].

In the wound area, large amounts of fibres and matrices are produced by fibroblasts. During this period, various capillaries are made by epithelial cells, such that granulation tissue forms. Granulation tissue can be thought of as a substrate that provides nutrition for epidermis formation. However, cutaneous appendages cannot regenerate completely after burning. Under the granulation tissue, reconstituting epidermal cells takes place. During the process of re-

epithelialization, hemidesmosomes attached to the basal keratinocytes within the dermis are dissolved by the newly expressed integrins, causing the latter to crawl over the wound matrix[86,87]. A significant body of research has revealed that keratins play a significant role in the crawling motility of adult keratinocytes and the purse-string closure of embryonic epidermal wounds [81]. Once keratinocytes migrate to the boundary of the wound, a proliferative burst of epidermis cells occurs[88,89]. The re-epithelialization will finish when a monolayer of keratinocytes covers the wound site, followed by the cessation of epidermal migration as well as the expression of new anchoring fibrils and hemidesmosome links to the basal lamina, integrins and matrix metalloproteinases. General opinion of this phenomenon is that it constitutes contact inhibition[90]. Meanwhile, regeneration of hair and sweat glands starts with the dermis. However, if the wound is deeper than the dermis and no hair follicles remain, hair regeneration will not happen. In a mice mould-based study[81,91], lymphoid enhancer factor-1 (LEF-1), sonic hedgehog (Shh), bone morphogenetic protein-2 (BMP-2) and FGF-4 had significant effects on hair growth. Thus, the main reason why regenerating hair is not possible is because a wound to an adult epidermis does not generate such signals from the underlying wound dermis [81]. Hair follicles could improve re-epithelialization, if the remaining hair follicles are able to provide a space for the proliferation of keratinocytes, allowing them to spread out like growing islands[89]. The proliferative scar forms a barrier that prevents sweat gland regeneration, on account of the fact that the stem cells in the injured sweat glands cannot activate the latter's regeneration, while the new epidermal stem cells also fail to differentiate into sweat gland cells after scar healing [92]. Regeneration of sweat gland cells is also regulated by the same factors, because sweat gland cells are homologous with the basal epidermal stem

cells[93]. Human umbilical cord- derived mesenchymal stem cells (hUC-MSCs) can differentiate into sweat gland-like cells by the induction of keratinocyte growth factor (KGF) [94]. During this process, blood vessels and nerves grow as well. Concerning angiogenesis, VEGF and FGF-2 are released for blood vessel growth [81]. FGF is indispensable and produced from damaged endothelial cells and macrophages at the wound site, while VEGF is induced by keratinocytes and macrophages at the wound edge in response to KGF and TGF-α [95,96]. Otherwise, there is some relative evidence of capillary morphogenesis due to regulated proteolysis at the wound site matrix [97]. For neural regeneration, nerve growth factor is the direct signal for nerve overgrowth [98], and it is up-regulated by the effect of TGF-α isoforms[99]. Conversely, sprouting nerves can deliver some neuropeptides and other growth factors to the wound site, enabling stimulatory effects to support the healing process[100,101].

For a deep burn (higher than second degree), the necrotic tissue cannot be dissolved or absorbed by the body, while granulation tissue occurs. About three to four days after the wound appears, resident dermal fibroblasts proliferate, with platelet-derived growth factor and TGF-β acting as mitogens and chemotactic factors for them[88]. Granulation tissue is new connective tissue which is full of microscopic blood vessels that form on the surfaces of a wound during the healing process. When granulation tissue take shape, organization will start and, during this period, granulation tissue will mature and replace necrosis tissue [82]. A week after the wound appears, a wound clot is replaced by a new collagen-rich matrix which is produced by fibroblasts stimulated by TGF-β1[81]. The wound contraction starts and fibroblasts reduce their expression of collagen receptors and raise the amount of integrins in order to crawl into the clot[102]. At this stage, some of fibroblasts transform into myofibroblasts, which is the source of contractile

forces because of the expression of α-smooth muscle actin [82]. Finally, a scar forms. Granulation tissue plays a significate role in ECM formation, as well as the operation of the immune system and vascularization. In the case of serious burns or deep-cut wounds, scars usually remain. This is because there are large areas to regenerate and the repair rate is not satisfactory [82,103]. In order to ensure the completeness of skin tissue, the body fills these areas with granulation tissue which grows into scar . A scar has stronger mechanical strength than granulation tissue. This process is led by change in the ECM structure. Many studies have revealed that a balance between TGF-β isoforms and neutralized TGF-β1 and -β2 at the time of wounding reduces scarring [81,104]. Mannose-6-phosphate (M-6-P) directly and indirectly applied to wounds will prevent scarring[105].

2.4.3 Wound dressings

The concept of moist wound healing was introduced by George Winter in 1963[106]. According to his theory, moist wounds heal faster than dry wounds. This has been supported by the findings of many other researchers [107,108]. This is because a moisture wound environment can protect cells from death by dehydration and accelerate angiogenesis [109,110]. To play an effective role in the management of wound, current wound dressings not only protect the wound from microorganisms and secondary damage, they also provide wounds with a moisture environment by using specific materials or structures, such as cotton fibres, polyester fibres, rayon fibres, nylon fibres, polyolefin fibres, acrylic fibres, elastomeric fibres, chitosan fibres and alginate fibres in a non-woven structure [111 112].

2.5 Conclusion

From the literature presented above, the research gaps have been identified, as listed in Section 1.4 in Chapter 1. This literature review provides a solid theoretical foundation for further work proposed in the following chapters.

Reference

1. Qin, Y. Alginate fibres: an overview of the production processes and applications in wound management. *Polymer International* **57**, 171–180 (2008).

2. Qin, Y. The characterization of alginate wound dressings with different fiber and textile structures. *Journal of Applied Polymer Science* **100**, 2516–2520 (2006).

3. Gupta, B., Agarwal, R. & Alam, M. S. Textile-based smart wound dressings. *Indian Journal of Fibre and Textile Research* **35**, 174–187 (2010).

4. Song, J. *et al.* Controllable release of vascular endothelial growth factor (VEGF) by wheel spinning alginate/silk fibroin fibers for wound healing. *Materials and Design* **212**, (2021).

5. Arikado, H. NII-Electronic Library Service. *Chemical Pharmaceutical Bulletin* 2091 (2002).

6. Qin, Y. The gel swelling properties of alginate fibers and their applications in wound management. *Polymers for Advanced Technologies* **19**, 6–14 (2008).

7. Cao, L., Lu, W., Mata, A., Nishinari, K. & Fang, Y. Egg-box model-based gelation of alginate and pectin: A review. *Carbohydrate Polymers* **242**, 116389 (2020).

8. Sennerby, L., Röstiund, T., Albrektsson, B. & Albrektsson, T. Acute tissue reactions to potassium

alginate with and without colour/ flavour additives. *Biomaterials* **8**, 49–52 (1987).

9. Ruvinov, E. & Cohen, S. Alginate biomaterial for the treatment of myocardial infarction: Progress, translational strategies, and clinical outlook. *Advanced Drug Delivery Reviews* **96**, 54–76 (2016).

10. Onuaguluchi, O. & Banthia, N. Plant-based natural fibre reinforced cement composites: A review. *Cement and Concrete Composites* **68**, 96–108 (2016).

11. Daunton, C., Kothari, S., Smith, L. & Steele, D. A history of materials and practices for wound management. *Wound Practice and Research The Australian Journal of Wound Management* **20**, 174–186 (2012).

12. Bouwstra, J. A. & Honeywell-Nguyen, P. L. Skin structure and mode of action of vesicles. *Advanced Drug Delivery Reviews* **54**, S41–S55 (2002).

13. Nazarko, L. Wound healing and moisture balance: selecting dressings. *Nursing and Residential Care* **11**, 286–291 (2009).

14. Bhattarai, N., Li, Z., Edmondson, D. & Zhang, M. Alginate-based nanofibrous scaffolds: Structural, mechanical, and biological properties. *Advanced Materials* **18**, 1463–1467 (2006).

15. Tamura, H., Tsuruta, Y. & Tokura, S. Preparation of chitosan-coated alginate filament. *Materials Science and Engineering C* **20**, 143–147 (2002).

16. de Moraes, M. A., Silva, M. F., Weska, R. F. & Beppu, M. M. Silk fibroin and sodium alginate blend: Miscibility and physical characteristics. *Materials Science and Engineering C* **40**, 85–91 (2014).

17. Chen, X., Wells, G. & Woods, D. M. *Production of Yarns and Fabrics from Alginate Fibres for Medical Applications*. *Medical Textiles* (The Bolton Institute, 2001).

doi:10.1533/9781845693145.1.20.

18. Sanchez-Ballester, N. M., Soulairol, I., Bataille, B. & Sharkawi, T. Flexible heteroionic calcium-magnesium alginate beads for controlled drug release. *Carbohydrate Polymers* **207**, 224–229 (2019).

19. Qin, Y. The characterization of alginate wound dressings with different fiber and textile structures. *Journal of Applied Polymer Science* **100**, 2516–2520 (2006).

20. de Moraes, M. A. & Beppu, M. M. Biocomposite membranes of sodium alginate and silk fibroin fibers for biomedical applications. *Journal of Applied Polymer Science* **130**, 3451–3457 (2013).

21. Lee, K. Y. & Mooney, D. J. Alginate: Properties and biomedical applications. *Progress in Polymer Science* **37**, 106–126 (2012).

22. Ruvinov, E. & Cohen, S. Alginate biomaterial for the treatment of myocardial infarction: Progress, translational strategies, and clinical outlook. *Advanced Drug Delivery Reviews* **96**, 54–76 (2016).

23. Draget, K. I. & Taylor, C. Chemical, physical and biological properties of alginates and their biomedical implications. *Food Hydrocolloids* **25**, 251–256 (2011).

24. Lee, K. Y. & Mooney, D. J. Alginate: Properties and biomedical applications. *Progress in Polymer Science* **37**, 106–126 (2012).

25. Steplewski, W., Wawro, D., Niekraszewicz, A. & Ciechańska, D. Research into the process of manufacturing alginate-chitosan fibres. *Fibres and Textiles in Eastern Europe* **14**, 25–31 (2006).

26. Shanmugasundaram, O. L. Development and characterization of cotton and organic cotton gauze fabric coated with biopolymers and antibiotic drugs for wound healing. *Indian Journal of Fibre and Textile Research* **37**, 146–150 (2012).

27. Parikh, D. v, Fink, T., DeLucca, A. J. & Parikh, A. D. Absorption and swelling characteristics of silver (I) antimicrobial wound dressings. *Textile Research Journal* **81**, 494–503 (2011).

28. TAKEI, F., KIMURA, K., MIZUNO, S., YAMAMOTO, T. & SHIMURA, K. Genetic analysis of the Nd-s mutation in the silkworm, Bombyx mori. *The Japanese Journal of Genetics* **59**, 307–313 (1984).

29. Tanaka, K., Mori, K. & Mizuno, S. Immunological identification of the major disulfide-linked light component of silk fibroin. *The Journal of Biochemistry* **114**, 1–4 (1993).

30. Chevillard, M., Couble, P. & Prudhomme, J.-C. Complete nucleotide sequence of the gene encoding the Bombyx mori silk protein P25 and predicted amino acid sequence of the protein. *Nucleic Acids Research* **14**, 6341 (1986).

31. Mita, K., Ichimura, S. & James, T. C. Highly repetitive structure and its organization of the silk fibroin gene. *Journal of molecular evolution* **38**, 583–592 (1994).

32. Zhou, C.-Z. *et al.* Fine organization of Bombyx mori fibroin heavy chain gene. *Nucleic acids research* **28**, 2413–2419 (2000).

33. Tanaka, K., Inoue, S. & Mizuno, S. Hydrophobic interaction of P25, containing Asn-linked oligosaccharide chains, with the HL complex of silk fibroin produced by Bombyx mori. *Insect biochemistry and molecular biology* **29**, 269–276 (1999).

34. Tanaka, K. *et al.* Determination of the site of disulfide linkage between heavy and light chains of silk fibroin produced by Bombyx mori. *Biochimica et Biophysica Acta (BBA)-Protein Structure and Molecular Enzymology* **1432**, 92–103 (1999).

35. Tsukada, M., Freddi, G., Gotoh, Y. & Kasai, N. Physical and chemical properties of tussah silk fibroin films. *Journal of Polymer Science Part B: Polymer Physics* **32**, 1407–1412 (1994).

36. Roh, D.-H. *et al.* Wound healing effect of silk fibroin/alginate-blended sponge in full thickness skin defect of rat. *Journal of Materials Science: Materials in Medicine* **17**, 547–552 (2006).

37. Yoo, C. R. *et al.* Effect of chitin/silk fibroin nanofibrous bicomponent structures on interaction with human epidermal keratinocytes. *International journal of biological macromolecules* **42**, 324–334 (2008).

38. Yeo, I.-S. *et al.* Collagen-based biomimetic nanofibrous scaffolds: preparation and characterization of collagen/silk fibroin bicomponent nanofibrous structures. *Biomacromolecules* **9**, 1106–1116 (2008).

39. Vasconcelos, A., Gomes, A. C. & Cavaco-Paulo, A. Novel silk fibroin/elastin wound dressings. *Acta biomaterialia* **8**, 3049–3060 (2012).

40. Khor, H. L. *et al.* Preliminary study of a polycaprolactone membrane utilized as epidermal substrate. *Journal of Materials Science: Materials in Medicine* **14**, 113–120 (2003).

41. Kanokpanont, S., Damrongsakkul, S., Ratanavaraporn, J. & Aramwit, P. Physico-chemical properties and efficacy of silk fibroin fabric coated with different waxes as wound dressing. *International journal of biological macromolecules* **55**, 88–97 (2013).

42. Çalamak, S., Erdoğdu, C., Özalp, M. & Ulubayram, K. Silk fibroin based antibacterial bionanotextiles as wound dressing materials. *Materials Science and Engineering: C* **43**, 11–20 (2014).

43. Zhou, Y. *et al.* Electrospinning of carboxyethyl chitosan/poly (vinyl alcohol)/silk fibroin nanoparticles for wound dressings. *International journal of biological macromolecules* **53**, 88–92 (2013).

44. Gu, Z., Xie, H., Huang, C., Li, L. & Yu, X. Preparation of chitosan/silk fibroin blending membrane fixed with alginate dialdehyde for wound dressing. *International journal of biological macromolecules* **58**, 121–126 (2013).

45. Zhang, X., Reagan, M. R. & Kaplan, D. L. Electrospun silk biomaterial scaffolds for regenerative medicine. *Advanced drug delivery reviews* **61**, 988–1006 (2009).

46. Lan, Y. *et al.* Therapeutic efficacy of antibiotic-loaded gelatin microsphere/silk fibroin scaffolds in infected full-thickness burns. *Acta biomaterialia* **10**, 3167–3176 (2014).

47. Aznar-Cervantes, S. *et al.* Fabrication of conductive electrospun silk fibroin scaffolds by coating with polypyrrole for biomedical applications. *Bioelectrochemistry* **85**, 36–43 (2012).

48. Zhang, X., Baughman, C. B. & Kaplan, D. L. In vitro evaluation of electrospun silk fibroin scaffolds for vascular cell growth. *Biomaterials* **29**, 2217–2227 (2008).

49. Zhou, J. *et al.* In vitro and in vivo degradation behavior of aqueous-derived electrospun silk fibroin scaffolds. *Polymer Degradation and Stability* **95**, 1679–1685 (2010).

50. Kim, U.-J., Park, J., Kim, H. J., Wada, M. & Kaplan, D. L. Three-dimensional aqueous-derived biomaterial scaffolds from silk fibroin. *Biomaterials* **26**, 2775–2785 (2005).

51. Huang, S., Yao, B., Xie, J. & Fu, X. 3D bioprinted extracellular matrix mimics facilitate directed differentiation of epithelial progenitors for sweat gland regeneration. *Acta biomaterialia* **32**, 170–

177 (2016).

52. Sun, G. *et al.* Dextran hydrogel scaffolds enhance angiogenic responses and promote complete skin regeneration during burn wound healing. *Proceedings of the National Academy of Sciences* **108**, 20976–20981 (2011).

53. Chouhan, D., Chakraborty, B., Nandi, S. K. & Mandal, B. B. Role of non-mulberry silk fibroin in deposition and regulation of extracellular matrix towards accelerated wound healing. *Acta biomaterialia* **48**, 157–174 (2017).

54. Mimura, Y. *et al.* Epidermal growth factor affects the synthesis and degradation of type I collagen in cultured human dermal fibroblasts. *Matrix Biology* **25**, 202–212 (2006).

55. Song, D. W. *et al.* Multi-biofunction of antimicrobial peptide-immobilized silk fibroin nanofiber membrane: Implications for wound healing. *Acta biomaterialia* **39**, 146–155 (2016).

56. Ju, H. W. *et al.* Wound healing effect of electrospun silk fibroin nanomatrix in burn-model. *International journal of biological macromolecules* **85**, 29–39 (2016).

57. Ponrasu, T., Vishal, P., Kannan, R., Suguna, L. & Muthuvijayan, V. Isabgol–silk fibroin 3D composite scaffolds as an effective dermal substitute for cutaneous wound healing in rats. *RSC advances* **6**, 73617–73626 (2016).

58. Baba, A. *et al.* Silk fibroin produced by transgenic silkworms overexpressing the Arg-Gly-Asp motif accelerates cutaneous wound healing in mice. *Journal of Dermatological Science* **84**, e150 (2016).

59. Lee, O. J. *et al.* Fabrication and characterization of hydrocolloid dressing with silk fibroin nanoparticles for wound healing. *Tissue Engineering and Regenerative Medicine* **13**, 218–226

(2016).

60. Safdari, M., Shakiba, E., Kiaie, S. H. & Fattahi, A. Preparation and characterization of Ceftazidime loaded electrospun silk fibroin/gelatin mat for wound dressing. *Fibers and Polymers* **17**, 744–750 (2016).

61. van Kampen, K. A. *et al.* Biofabrication: From additive manufacturing to bioprinting. *Encyclopedia of Tissue Engineering and Regenerative Medicine* **1–3**, 41–55 (2019).

62. Kim, H. C., Kim, D., Lee, J. Y., Zhai, L. & Kim, J. Effect of Wet Spinning and Stretching to Enhance Mechanical Properties of Cellulose Nanofiber Filament. *International Journal of Precision Engineering and Manufacturing - Green Technology* **6**, 567–575 (2019).

63. Puppi, D. & Chiellini, F. Wet-spinning of biomedical polymers: from single-fibre production to additive manufacturing of three-dimensional scaffolds. *Polymer International* **66**, 1690–1696 (2017).

64. Yang, Z., Peng, H., Wang, W. & Liu, T. Crystallization behavior of poly(ε-caprolactone)/layered double hydroxide nanocomposites. *Journal of Applied Polymer Science* **116**, 2658–2667 (2010).

65. Mota, C., Puppi, D., Dinucci, D., Gazzarri, M. & Chiellini, F. Additive manufacturing of star poly(ε-caprolactone) wet-spun scaffolds for bone tissue engineering applications. *Journal of Bioactive and Compatible Polymers* **28**, 320–340 (2013).

66. Lavin, D. M. *et al.* Multifunctional polymeric microfibers with prolonged drug delivery and structural support capabilities. *Acta Biomaterialia* **8**, 1891–1900 (2012).

67. Borgogna, M., Skjåk-Bræk, G., Paoletti, S. & Donati, I. On the initial binding of alginate by calcium

ions. the tilted egg-box hypothesis. *Journal of Physical Chemistry B* **117**, 7277–7282 (2013).

68. Sikorski, P., Mo, F., Skjåk-Bræk, G. & Stokke, B. T. Evidence for egg-box-compatible interactions in calcium - Alginate gels from fiber x-ray diffraction. *Biomacromolecules* **8**, 2098–2103 (2007).

69. Li, L., Fang, Y., Vreeker, R., Appelqvist, I. & Mendes, E. Reexamining the egg-box model in calcium - Alginate gels with X-ray diffraction. *Biomacromolecules* **8**, 464–468 (2007).

70. Dalheim, M. *et al.* Efficient functionalization of alginate biomaterials. *Biomaterials* **80**, 146–156 (2016).

71. Sanchez-Ballester, N. M., Soulairol, I., Bataille, B. & Sharkawi, T. Flexible heteroionic calcium-magnesium alginate beads for controlled drug release. *Carbohydrate Polymers* **207**, 224–229 (2019).

72. Delaney, J. T., Liberski, A. R., Perelaer, J. & Schubert, U. S. Reactive inkjet printing of calcium alginate hydrogel porogens - A new strategy to open-pore structured matrices with controlled geometry. *Soft Matter* **6**, 866–869 (2010).

73. Ureña-Benavides, E. E., Brown, P. J. & Kitchens, C. L. Effect of Jet Stretch and Particle Load on Cellulose Nanocrystal−Alginate Nanocomposite Fibers. *Langmuir* **26**, 14263–14270 (2010).

74. Liu, J., Zhang, R., Ci, M., Sui, S. & Zhu, P. Sodium alginate/cellulose nanocrystal fibers with enhanced mechanical strength prepared by wet spinning. *Journal of Engineered Fibers and Fabrics* **14**, 155892501984755 (2019).

75. Wu, H., Liu, J., Fang, Q., Xiao, B. & Wan, Y. Establishment of nerve growth factor gradients on aligned chitosan-polylactide /alginate fibers for neural tissue engineering applications. *Colloids and Surfaces B: Biointerfaces* **160**, 598–609 (2017).

76. Um, I. C. *et al.* Wet spinning of silk polymer: I. Effect of coagulation conditions on the morphological feature of filament. *International journal of biological macromolecules* **34**, 89–105 (2004).

77. Ha, S.-W., Tonelli, A. E. & Hudson, S. M. Structural studies of bombyx m ori silk fibroin during regeneration from solutions and wet fiber spinning. *Biomacromolecules* **6**, 1722–1731 (2005).

78. ISHIZAKA, H., WATANABE, Y., ISHIDA, K. & FUKUMOTO, O. Regenerated silk prepeared from ortho phosphoric acid solution of fibroin. *The Journal of Sericultural Science of Japan* **58**, 87–95 (1989).

79. Matsumoto, K., Uejima, H., Iwasaki, T., Sano, Y. & Sumino, H. Studies on regenerated protein fibers. III. Production of regenerated silk fibroin fiber by the self-dialyzing wet spinning method. *Journal of Applied Polymer Science* **60**, 503–511 (1996).

80. Ha, S.-W., Park, Y. H. & Hudson, S. M. Dissolution of Bombyx m ori silk fibroin in the calcium nitrate tetrahydrate− methanol system and aspects of wet spinning of fibroin solution. *Biomacromolecules* **4**, 488–496 (2003).

81. Martin, P. Wound healing--aiming for perfect skin regeneration. *Science* **276**, 75–81 (1997).

82. Clark, R. A. F. *The molecular and cellular biology of wound repair*. (Springer Science & Business Media, 2013).

83. Springer, T. A. Traffic signals for lymphocyte recirculation and leukocyte emigration: the multistep paradigm. *Cell* **76**, 301–314 (1994).

84. Mayadas, T. N., Johnson, R. C., Rayburn, H., Hynes, R. O. & Wagner, D. D. Leukocyte rolling and

extravasation are severely compromised in P selectin-deficient mice. *Cell* **74**, 541–554 (1993).

85. Hübner, G. *et al.* Differential regulation of pro-inflammatory cytokines during wound healing in normal and glucocorticoid-treated mice. *Cytokine* **8**, 548–556 (1996).

86. Paglia, P., Girolomoni, G., Robbiati, F., Granucci, F. & Ricciardi-Castagnoli, P. Immortalized dendritic cell line fully competent in antigen presentation initiates primary T cell responses in vivo. *The Journal of experimental medicine* **178**, 1893–1901 (1993).

87. Cavani, A. *et al.* Distinctive integrin expression in the newly forming epidermis during wound healing in humans. *Journal of Investigative Dermatology* **101**, 600–604 (1993).

88. Garlick, J. A. & Taichman, L. B. Fate of human keratinocytes during reepithelialization in an organotypic culture model. *Laboratory investigation; a journal of technical methods and pathology* **70**, 916–924 (1994).

89. Matoltsy, A. G. & Viziam, C. B. Futher observations on epithelialization of small wounds. in *An autoradiographic study of incorporation and distribution of H3-thymidine in the epithelium covering skin wounds* vol. 55 20 (1970).

90. Compton, C. C. *et al.* Skin regenerated from cultured epithelial autografts on full-thickness burn wounds from 6 days to 5 years after grafting. A light, electron microscopic and immunohistochemical study. *Laboratory investigation; a journal of technical methods and pathology* **60**, 600–612 (1989).

91. Zhou, P., Byrne, C., Jacobs, J. & Fuchs, E. Lymphoid enhancer factor 1 directs hair follicle patterning and epithelial cell fate. *Genes & development* **9**, 700–713 (1995).

92. Ma, K., Tan, Z., Zhang, C. & Fu, X. Mesenchymal stem cells for sweat gland regeneration after burns: from possibility to reality. *Burns* **42**, 492–499 (2016).

93. Biedermann, T. *et al.* Human eccrine sweat gland cells can reconstitute a stratified epidermis. *Journal of Investigative Dermatology* **130**, 1996–2009 (2010).

94. Xu, Y. *et al.* Role of keratinocyte growth factor in the differentiation of sweat gland-like cells from human umbilical cord-derived mesenchymal stem cells. *Stem Cells Translational Medicine* **5**, 106–116 (2016).

95. Broadley, K. N. *et al.* Monospecific antibodies implicate basic fibroblast growth factor in normal wound repair. *Laboratory investigation; a journal of technical methods and pathology* **61**, 571–575 (1989).

96. Brown, L. F. *et al.* Expression of vascular permeability factor (vascular endothelial growth factor) by epidermal keratinocytes during wound healing. *The Journal of experimental medicine* **176**, 1375–1379 (1992).

97. Fisher, C. *et al.* Interstitial collagenase is required for angiogenesis in vitro. *Developmental biology* **162**, 499–510 (1994).

98. Constantinou, J., Reynolds, M. L., Woolf, C. J., Safieh-Garabedian, B. & Fitzgerald, M. Nerve growth factor levels in developing rat skin: upregulation following skin wounding. *Neuroreport* **5**, 2281–2284 (1994).

99. Buchman, V. L., Sporn, M. & Davies, A. M. Role of transforming growth factor-beta isoforms in regulating the expression of nerve growth factor and neurotrophin-3 mRNA levels in embryonic

cutaneous cells at different stages of development. *Development* **120**, 1621–1629 (1994).

100. Nilsson, J., von Euler, A. M. & Dalsgaard, C.-J. Stimulation of connective tissue cell growth by substance P and substance K. *Nature* **315**, 61–63 (1985).

101. Lee, K.-F. *et al.* Targeted mutation of the gene encoding the low affinity NGF receptor p75 leads to deficits in the peripheral sensory nervous system. *Cell* **69**, 737–749 (1992).

102. Xu, J. & Clark, R. A. Extracellular matrix alters PDGF regulation of fibroblast integrins. *The Journal of cell biology* **132**, 239–249 (1996).

103. Brem, H. & Tomic-canic, M. Cellular and molecular basis of wound healing in diabetes Find the latest version : Cellular and molecular basis of wound healing in diabetes. **117**, 1219–1222 (2007).

104. Marx, J., Hockberger, R. & Walls, R. *Rosen's Emergency Medicine-Concepts and Clinical Practice E-Book: 2-Volume Set*. (Elsevier Health Sciences, 2013).

105. Shah, M., Foreman, D. M. & Ferguson, M. W. Neutralising antibody to TGF-beta 1, 2 reduces cutaneous scarring in adult rodents. *Journal of cell science* **107**, 1137–1157 (1994).

106. Miletic, B. & Petrovic, D. Natur e 100 ~ 91. 6–7 (1963).

107. Blume, P. A., Walters, J., Payne, W., Ayala, J. & Lantis, J. Comparison of Negative Pressure Wound Therapy Using Vacuum-Assisted Closure With Advanced Moist Wound Therapy in the Treatment of Diabetic Foot Ulcers. *Diabetes Care* **31**, 631–636 (2008).

108. Pakyari, M., Farrokhi, A., Maharlooei, M. K. & Ghahary, A. Critical Role of Transforming Growth Factor Beta in Different Phases of Wound Healing. *Advances in Wound Care* **2**, 215–224 (2013).

109. Eaglstein, W. H. Moist Wound Healing with Occlusive Dressings: A Clinical Focus. *Dermatologic*

Surgery **27**, 175–182 (2001).

110. Kerstein, M. D. Introduction: Moist wound healing. *The American Journal of Surgery* vol. 167 S1 (1994).

111. Gupta, B., Agarwal, R. & Alam, M. Textile-based smart wound dressings. *Indian Journal of Fibre & Textile Research* **35**, 174–187 (2010).

112. Mortimer, D. *Moist wound dressings and pressure relieving surfaces mechanisms , materials and a review of some cost- effectiveness findings*. (Centre for Health Program Evaluation, 2001).

Chapter 3 Wheel-spinning technique for wet-spun fibre fabrication with unique drawing and twisting effects

This chapter focuses on the second objective. The research has been completed and prepared for publication in *Materials & Design*.

Title: Wheel-spinning technique for wet-spun fibre fabrication with unique drawing and twisting effects

Authors: Zhongda Chen, Yumin Xia, Yi Li

Journal: Submission to *Materials & Design*

My contribution: I have designed both two-wheel spinning machines, designed all the experiments, performed the theoretical analysis and undertaken all the characterizations for the wheel-spun fibres. I have also prepared the tables, the figures and the entire manuscript.

Co-author contributions: Mr. Yumin Xia provided supported on WSM design and fibre fabrication. Professor Yi Li supervised the whole project in this section and revised the manuscript.

Abstract

In traditional wet spinning, drawing out fibre is realized by the speed difference of the roller, which is neither continuous nor smooth. Further, in traditional ring spinning, the twisting effect relies on the traveller's rotation, which is not easy to achieve when working in a coagulating bath for *in situ* fibre fabrication. In this research, we reported a method to fabricate wet-spun fibre with drawing and self-twisting effects *in situ* by using our unique wheel-spinning machine. The following tensile test demonstrated that the twisting effect for alginate wheel-spun fibre shows a higher strain than the non-twisting one.

Keywords

Wet spinning; twisting effect; vortex; alginate fibre; egg-box dimers

3.1 Introduction

Raw mid/over-length regenerated fibre can be fabricated by coagulation in solution, known as wet spinning, which requires a further process to stabilize character and performance because of its low tensile properties, high extension and high water shrinkage [1]. A significant body of research has been carried out into fabricated micro-fibre using the wet-spinning method, including MXene, polylactide, poly (styrene sulfonate), graphene oxide, polyvinylidene fluoride and polyacrylonitrile [2-7].

There are several studies indicated that the drawing effect for wet-spun fibre can improve mechanical performance [3,5]. Moreover, our previous study [8] demonstrated that the force given by the fluid in our wheel-spinning machine (WSM) facilitated a drawing effect during

fibre fabrication, in turn significantly increasing the strength and breaking strain of alginate fibre. Based on this WSM, an advantaged WSM device has been designed and compared with the previous iteration. The new device can also provide a twisting effect for fibre, which could further increase mechanical performance and produce a unique surface pattern for the fibre.

In this work, two WSM set-ups (A and B) based on wet-spun technology were introduced. In particular, no study, to our knowledge, has considered fabricating wet-spun fibre via the force given by the fluid to drawing and twisting the fibre *in situ*. The drawing effect is given by the drag of liquid, which is more uniform and smoother than traditional wet spinning. The drawing and twisting rate can also be controlled by controlling the parameters of the WSM set-up. The alginate-based wheel-spun fibre is then fabricated and characterized, after which its morphology, chemical property and mechanical performance are characterized in order to confirm the feasibility of any potential applications and optimize the best parameters.

3.2 Material and method

3.2.1 The fabrication of the WSM set-up

The WSMs, as a whole, are fabricated by a Fused Deposition Modelling 3D Printer (FDM-3D printer, Creality Ender 3, China), while the material to build them is polylactic acid (PLA, ESUN PLA+ 1.75mm, China). The parameters of the FDM-3D printer set-up is as follows: using a brass nozzle with a 0.4 mm diameter, the layer thickness during printing is 0.12 mm, and the nozzle and bed temperature are 220°C and 60°C, respectively.

3.2.2 WSM Set-up A

WSM Set-up A (the 3D model is available in the supporting information) consists of a regular

hexakaidecagonal (16-sided) prism configuration rotator and a bedplate (Fig. 3.1a). Sixteen blades are located behind each edge which are parallel to the vertical axis. Each blade has a 20° angle with each edge located on the horizontal plane. WSM Set-up A rotates controllably via a facile method, which has two magnets assembled on the bottom of the rotator and can be controlled by a magnetic stirrer. When the rotator rotates in clockwise, the coagulation bath liquid is pumped into the inner rotator by blades, which subsequently comes out from the holes located on the bottom boards of the rotator, forming a fluid circulation. This circulation can draw and draft the fibre formed from the needle and allow the fibre to attach to the rotator. With the completion of the spinning process, the machine with the fibre is removed from the coagulation bath and placed it into a wash bath to clean the remaining coagulation solution. After that, the rotator runs slowly anti-clockwise, and fibre is collected from the end, so that the fibre attached to the rotator can be removed and transformed to a spool for drying and storing.

3.2.3 WSM Set-up B

WSM Set-up B is (the 3D model is available in the supporting information) consists of a rotator, an impeller and a co-axis shaft to provide rotary power for each of them (Fig. 3.1b). The rotator has a diamond configuration and a flame solely to minimize how it affects the vortex. The impeller is placed under the rotator to generate the vortex so as to draft and twist the fibre. The rotator and impeller pivot relative to the same shaft. The shaft is a co-axis structure which provides an individual rotation speed for both rotator and impeller. The rotation of the rotator and impeller is derived by a respective motor. The rotator can be removed from the machine, with the fibre collected in a similar way to that mentioned above.

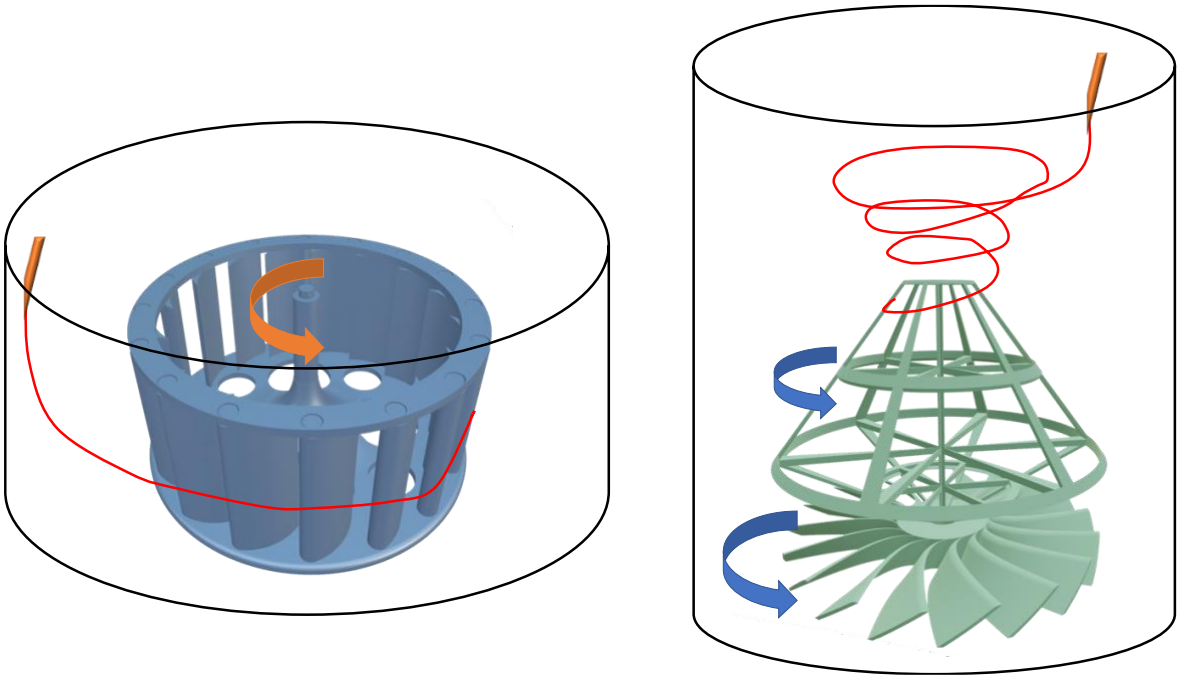

Fig. 3.1 The design of WSM (a) Set-up A and (b) Set-up B.

3.2.4 Alginate-based wheel-spun fibre fabrication

Sodium alginate powder (NaAlg, W201502) and calcium chloride ($CaCl_2$) were purchased from Sigma Aldrich, MO USA, then used as received. The alginate fibre was prepared on application of the optimized wet-spinning method. Briefly, $CaCl_2$ aqueous solution was chosen as a coagulation bath. A schematic diagram of the wet-spinning system set-up is presented in Fig. 3.1a. Sodium alginate was dissolved in deionized water with a concentration of 20 and 50 g/L and stirred for 6 h to obtain a 2% and a 5% NaAlg solution (w/v), respectively. The NaAlg solution was then inserted into the syringe pump and extruded into a 2% $CaCl_2$ coagulation bath via a needle with a 19G needle tip. The injection speed was 2 ml/min. The needle with sharp tips and perpendicular to the surface. After being drawn and collected by a roller in the coagulation bath, the NaAlg fibre was washed twice by deionized water and dried on a fume board for further conditioning and testing (ISO 139:2005).

Six groups of samples have been selected to evaluate the performance of both WSM set-ups, as presented in Table 3.1.

Table 3.1 The sample groups of wheel-spun alginate fibres.

	a	**b**	**c**	**d**	**e**	**f**
Rotator speed (rpm)	120	90	60	60	60	45
Impeller speed (rpm)	60	45	30	0	N/A	N/A
WSM set-up	B	B	B	B	A	A

3.2.5 SEM

The surface morphology of wheel-spun fibres was observed by means of a field emission scanning electron microscope (FE-SEM, Zeiss Ultra 55, Germany) at 3 kV after gold coating for 10 nm.

3.2.6 Tensile test

The mechanical performances of the wheel-spun fibre were characterized by a universal materials tester (Instron 5566, MA USA) at a crosshead speed of 2 mm/min.

3.2.7 Statistics

The results of mechanical performances were presented as means ± standard deviations. Statistical differences amongst sample groups were processed by Student's t-test in IBM SPSS (Ver. 24.000) using the least significant difference. Differences were significant (*) when $p < 0.01$.

3.3 Result and discussion

3.3.1 WSM design

3.3.1.1 Design of WSM Set-up A

This version of the WSM is able to generate circulation in the coagulation bath via rotator spinning and to cause the fluid to draw and collect the fibre from the extrusion needle. When the WSM rotates, the blenders drive the fluid move. The motion of the fluid drags the fibre from the needle to the rotator, before coiling around the rotator. With the fluid speed being greater than the speed of solution being extruded, the fibre is drawn to a significant extent during the spinning process. When the fluid starts to circulate during its rotating, the fibre can be drawn and collected without limits.

3.3.1.2 Design of WSM Set-up B

This version of the WSM can create circulation via the rotation of a centrifugal impeller. This will generate a vortex at the centre of the coagulation bath, with the water driven from the top to the bottom and then moved from the bottom to the top at the outer space of the coagulation bath. There is a beneficial effect from the vortex at the centre of the coagulation bath, when the extrusion solution is extruded into the coagulation bath, producing a fibre that is drawn by the vortex from the top edge to the middle bottom of the coagulation bath, before finally attaching itself to the collector. The collector can rotate at different speeds along with the centrifugal impeller, which ensures that the fibre can be collected properly.

As with Set-up A, WSM Set-up B not only draws but also twists the fibre via the flow. The

twisting principle of the WSM Set-up B is similar to traditional ring spinning [9]. However, it is the vortex, instead of the traveller in the ring rail, which achieve the self-rotating nature of the fibre.

3.3.2 Fibre force analysis

3.3.2.1 Force analysis of WSM Set-up A

Fibre force analysis: The extrusion solution was extruded into the coagulation bath as a result of the rotating fluid, which went towards the WSM following a spiral path. The fibre force analysis for the wheel-spun fibre in the $CaCl_2$ coagulation bath is presented in Fig. 3.2 a. After a jet of alginate and alginate-based solution was injected into the coagulation bath using the needle, the vertical buoyancy and gravity ensured that the fibre was stable in the bath. The injected solution was then quickly coagulated towards a hydrogel fibre due to the chemical reaction between alginic acid and calcium chloride. As the fibre slowly approached the centre of the bath vat, the spinning rotator applied a Coriolis force and a tangential centripetal force to the fibre [10]. Coriolis and centripetal forces can lead to polymer fibre deformation. The direction of the Coriolis force was opposite to the liquid drag of fibre. The simulations on polymer solution, which applied a Coriolis force, were mainly focused on spin-coating fabrication [11]. A specific theoretical model for wet-spinning solution or similar polymer jets, when applying a Coriolis force, has neither been established nor been well acknowledged. Thus far, it can only be confirmed that polymer viscoelasticity is the key factor influencing fibre diameter and mechanical performances [12].

Based on the force analysis, the effect of the drawing rate can be calculated:

The linear velocity of fluid at the extrusion needle is:

$$v_d = \omega \cdot r_{needle} \qquad (1)$$

where ω is the angular velocity of the WSM and r_{fibre} is the radius from the needle to the centre of the coagulating bath.

The fibre is also subject to the centripetal force and moves toward to the centre of the coagulating bath, which gives the fibre a centripetal acceleration.

$$F_c = m \cdot a_c = \frac{m{v_d}^2}{r_{fibre}} = m \cdot \omega^2 \cdot r_{fibre} \qquad (2)$$

$$a_c = \omega^2 \cdot r_{fibre} \qquad (3)$$

where m is the mass at any point within the fibre, r_{fibre} is the distance between any point from the fibre to the centre of the coagulating bath, and v_d is the linear velocity of the fibre.

Thus, the fluid speed at r direction is:

$$v_c = v_0 + a_c \cdot t = v_0 + \omega^2 \cdot r_{fibre} \cdot t \qquad (4)$$

where, typically, $v_0 = 0$. This is because the needle position is less than or equal to v_d.

The distance of any point from the fibre to the centre of the coagulating bath is changed by time:

$$r_{fibre} + \frac{1}{2} \cdot a_c \cdot t^2 = r_{needle} \quad (5)$$

Thus,

$$r_{fibre} = \frac{r_{needle}}{1+\left(\frac{\omega^2}{2} \cdot t^2\right)} \qquad (6)$$

The total speed needed to drag the fibre is:

$$\overrightarrow{\boldsymbol{v_{fibre}}} = \overrightarrow{\boldsymbol{v_c}} + \overrightarrow{\boldsymbol{v_d}} = \overrightarrow{(\boldsymbol{v_c}, \boldsymbol{0})} + \overrightarrow{(\boldsymbol{0}, \boldsymbol{v_d})} \qquad (7)$$

$$v_{fibre}{}^2 = v_c{}^2 + v_d{}^2 \qquad (8)$$

$$v_{fibre} = \sqrt{(\omega^2 \cdot r \cdot t) \cdot (\omega \cdot r)} = \left[\frac{(2 \cdot r_{needle} \cdot \omega)(1+\omega \cdot t)}{2+(\omega \cdot t)^2}\right]^{1/2} \qquad (9)$$

Thus, the fibre speed will increase fast at first then slowly drop. The WSM rotation speed, as well as the distance from the extrusion needle to the centre of the coagulating bath, will affect the drawing rate.

Drawing effect: The drawing rate is defined as the ratio of initial speed to highest speed, as the fibre does not break during the spinning process. The drawing rate can be represented as follows:

$$D = \frac{V_{extrusion}}{Max(V_{fibre})} \qquad (10)$$

3.3.2.2 Force analysis of WSM Set-up B

Pressure distribution within the coagulating bath: To understand the fibre's behaviour under the effect of the WSM MK III, it is essential to analyse the pressure distribution given by the machine.

To the wheel-spinning bath, a spinning coordinate system is introduced at any position, described as $(r,\ \theta,\ h,\ \omega)$. There is no relative motion between particles; the fluid is free of shear stresses, and the flow can be considered as inviscid.

All calculations use the International System of Units, as follows:

$$r\ (m),$$

$$\theta(°),$$

$$h(m),$$

$$\omega(°/s),$$

$$g\left(\frac{9.8m}{s}\right),$$

$$\rho\left(\frac{kg}{m^3}\right).$$

During the rotation of the WSM, under a state of relative equilibrium, the solution in the bath rotates with a constant angular velocity ω about the centre of the WMS, which is considered as the vertical axis. From the surface of the solution, the depth is h. From the centre of the WSM (as well as the centre of the vortex), the distance on the horizontal plane is r.

When the solution is static, the pressure of the solution is:

$$p = \rho g h \qquad (11)$$

where ρ is the density of the solution and g is the gravity.

When the solution starts to rotate with a constant ω, the tangential velocity v_d at r will be given by:

$$v_d = \omega \cdot r \qquad (12)$$

The centrifugal force is then generated. At the position of $(r,\ h)$, the centrifugal force applied is $F_c = m \cdot r\omega^2$, where m is the mass of flow at this point. There is no Coriolis force under the state of relative equilibrium because there is no accelerated velocity.

Based on Euler equations, in the direction of r:

$$P(r + dr, z)\delta A - P(r, z)\delta A = P\delta A dr\omega^2 r \qquad (13)$$

which means:

$$\frac{\partial P}{\partial r} = \rho\omega^2 r \qquad (14)$$

This can be integrated to give:

$$P = \frac{1}{2}\rho(r\omega^2)r + C1(z) \qquad (15)$$

In the direction of z:

$$P(r, z+dz)\delta A - P(r,z)\delta A + \rho\delta A dz g = 0 \qquad (16)$$

which means:

$$\frac{\partial P}{\partial z} + \rho g = 0 \qquad (17)$$

This can be integrated to give:

$$P + \rho g z + C2(r) = 0 \qquad (18)$$

We now combine Equation (15) and Equation (18):

$$\left[\frac{1}{2}\rho(r\omega^2)r + C2(r)\right] + [C1(z) + \rho g z] = 0 \qquad (19)$$

At any point in the spinning coordinate system, we defined:

$$\left[\frac{1}{2}\rho(r\omega^2)r + C2(r)\right] = -C \qquad (20)$$

$$[C1(z) + \rho g z] = C \qquad (21)$$

where C is a constant. The pressure distribution is given as:

$$p(r, \omega, z) = \frac{1}{2}\rho(r\omega^2)r - \rho g z + C \qquad (22)$$

The pressure on the free surface can be taken as p_0, according to the condition of the rotation centre:

$$p(0,0,h) = -\rho g h + C = p_0$$

$$\Longrightarrow C = p_0 + \rho g h \qquad (23)$$

Thus, the function of the pressure distribution is given as:

$$p(r, \omega, z) = \frac{1}{2}\rho(r\omega^2)r + \rho g(h - z) + p_0 \qquad (24)$$

From Equation (24) and Fig. 3.2c, it can be observed that the pressure outside the vortex is higher than at the centre of the vortex. This could cause a pressure difference towards the centre of the vortex. Based on the feature of the vortex, the path of the flow is following the geometrical pattern of a logarithmic spiral. Given that a normal line at any point in the logarithmic spiral will not pass the centre of the vortex, ΔP can be decomposed as tractive effort ΔP_t and centripetal force ΔP_n vectorially, as shown in Fig. 3.2b.

Fibre force analysis: Based on Bernoulli's principle

$$\frac{1}{2}\rho v^2 + \rho g h + \Delta P_t = Constant \qquad (25)$$

This means that the velocity of the flow increases along with a decrease in the pressure. The force analysis of any point of the fibre after extrusion and before collection is given in Fig. 3.2b. Where buoyancy is F_b, gravity is G, the tractive force of the needle is T_n, the tractive force of the collector is T_c, the component vortex pressure difference toward the centre is ΔP_n, and the component vortex pressure difference for fibre acceleration ΔP_t, Fig. 3.2b underlines the relationship between p, r and z at a constant ω. Considering the physical truth of the fibre-spinning process, it is balance between buoyancy and gravity as well as the tractive force of the needle and the tractive force of the collector.

$$F_b = G, T_n = T_c \qquad (23)$$

Since the path of the fibre is following the logarithmic spiral, the path projected on the transverse plane can be represented as:

$$r = ae^{k\theta}, \theta \in \mathbb{R} \qquad (24)$$

where a and k are constant in order to control the shape of the spiral.

Based on the force analysis, the effect of the drawing rate can be calculated.

The linear velocity of the fluid at the extrusion needle is:

$$v_d = \omega \cdot r_{needle} \qquad (25)$$

where r_{needle} is the distance from the centre of the coagulating bath to the extrusion needle.

The fibre is drawn by force ΔP_t, which is equal to:

$$\Delta P_t = P \cdot \tan^{-1} k \qquad (26)$$

The accelerated velocity in the tangential direction of the fibre can be given as:

$$a_t(\omega, r, z) = \frac{\Delta P_t}{m} = \frac{\left[\frac{1}{2}\rho(r_{fibre}\omega^2)r_{fibre} + \rho g(h-z) + p_0\right] \cdot \tan^{-1} k}{m} \qquad (27)$$

where m is the mass at any point within the fibre, r_{fibre} is the distance from the fibre to the centre of the coagulating bath, and h is the initial height of the needle.

Thus, the velocity in the tangential direction of the fibre can be given as:

$$v_t(\omega, r, z) = a_t \cdot t = \frac{\Delta P_t}{m} \cdot t \qquad (28)$$

where t is the time at which the fibre has been extruded.

The accelerated velocity in the centripetal direction is:

$$F_c = \Delta P_n = m \cdot a_c = \frac{m{v_t}^2}{r_{fibre}} \qquad (29)$$

$$\Delta P_n = P \cdot \cos^{-1} k \qquad (30)$$

$$a_c = \frac{\Delta P_n}{m} = \frac{m{v_t}^2}{r_{fibre}} = \frac{m \cdot \left[\left(\omega \cdot r_{needle} + \frac{\Delta P_t}{m} \cdot t\right)^2\right]}{r_{fibre}} \qquad (31)$$

Thus, the velocity in the centripetal direction of fibre can be given:

$$v_c(\omega, r, z) = a_c \cdot t = \frac{\Delta P_n}{m} \cdot t \qquad (32)$$

The accelerated velocity at z direction is constant:

$$a_z = \frac{P_z}{m} = \frac{\rho g z}{m} \qquad (33)$$

Thus, the velocity at z direction can be given as:

$$v_z(\omega, r, z) = \frac{\rho g z}{m} \cdot t \qquad (34)$$

The total speed to drag the fibre is:

$$\overrightarrow{\boldsymbol{v_{fibre}}} = \overrightarrow{\boldsymbol{v_c}} + \overrightarrow{\boldsymbol{v_t}} + \overrightarrow{\boldsymbol{v_z}} = \overrightarrow{(\boldsymbol{v_c}, \boldsymbol{0}, \boldsymbol{0})} + \overrightarrow{(\boldsymbol{0}, \boldsymbol{v_d}, \boldsymbol{0})} + \overrightarrow{(\boldsymbol{0}, \boldsymbol{0}, \boldsymbol{v_z})} \qquad (35)$$

$$v_{fibre}{}^2 = v_c{}^2 + v_d{}^2 + v_z{}^2 = \left(\frac{\Delta P_t}{m} \cdot t\right)^2 + \left(\frac{\Delta P_n}{m} \cdot t\right)^2 + \left(\frac{\rho g z}{m} \cdot t\right)^2 \qquad (36)$$

$$v_{fibre} = \left(\frac{\Delta P_t + \Delta P_n + \rho g z}{m}\right) \cdot t \qquad (37)$$

Drawing effect: Combining Equations (24), (26), (30) and (37), the pressure increases linearly together with the increase in height (it increases quadratically according to the decrease in radius). This is the key factor that causes the drawing effect of the fibre: as the flow velocity increases by a constant acceleration, the drawing effect is continuous and gentle. A change of r and ω could change the drawing effect.

The drawing effect could be given as Equation (10).

Twisting effect: The twist of the fibre is caused by its rotation in the coagulating bath, above the roller. The degree of twisting is controlled by the cycles of the rotation before the fibre is collected onto the roller, as well as the length of the fibre between the extraction needle and the roller.

When compared with the twisting effect in the ring-spinning method, there are some differences: firstly, the fibre within the coagulating bath is drawn and twisted at the meanwhile; secondly,

the self-rotating behaviour of the fibre is not tight but follows the flow which has a logarithmic spiral trajectory. As the rotation speed of the collector is faster than the flow rotating speed, when the fibre becomes tighter, the spiral pattern is transferred to the self-rotation within the fibre. The twisting effect should be uniform at every point in the fibre because the ratio of the collector to the flow rotation speed ($\frac{v_{collector}}{v_{flow}}$) is constant.

The twisting could be described as (cycle/m), as shown at Fig. 3.2d.

For the length of the fibre between the needle and the collector, the arc length of the path can be given by integrating Equation (38):

$$L_p(\theta_c - \theta_n) = \frac{\sqrt{k^2+1}}{k}\big(r(\theta_n) - r(\theta_c)\big) \qquad (38)$$

where θ_c is the position of the collector and θ_n is the position of the needle.

The actual length of the fibre between the needle and the collector is:

$$L = \frac{L_p}{\cos\left[\tan^{-1}\left(\frac{h_n - h_c}{L_p}\right)\right]} \qquad (39)$$

where h_c is the height of the collector and h_n is the height of the needle.

Combining Equations (38) and (39),

$$L = \frac{\frac{\sqrt{k^2+1}}{k}\big(r(\theta_n) - r(\theta_c)\big)}{\cos\left[\tan^{-1}\left(\frac{h_n - h_c}{L_p}\right)\right]} \qquad (40)$$

The twisting effect can be represented as:

$$T = \frac{(\theta_n - \theta_c)/2\pi}{L} \qquad (41)$$

Thus, the twisting effect depends on the needle position, the collector's diameter and height, the vortex speed and the flow angular velocity.

The twisting effect of WSM Set-up B is a combination of physical change and chemical reaction. Firstly, the extraction solution is injected into the coagulation bath, the chemical reaction happens at the interface of two solutions, and the extraction solution transform into soft fibre with a solid surface. With the flow movement and the shear force applied to the fibre, the fibre moves by following the trajectory of the flow. As the flow speed is faster than the extrusion speed, the fibre is drawn and twists. The new surface is generated continuously and the molecular arrangement on the surface of the fibre is rearranged in the direction of the fibre.

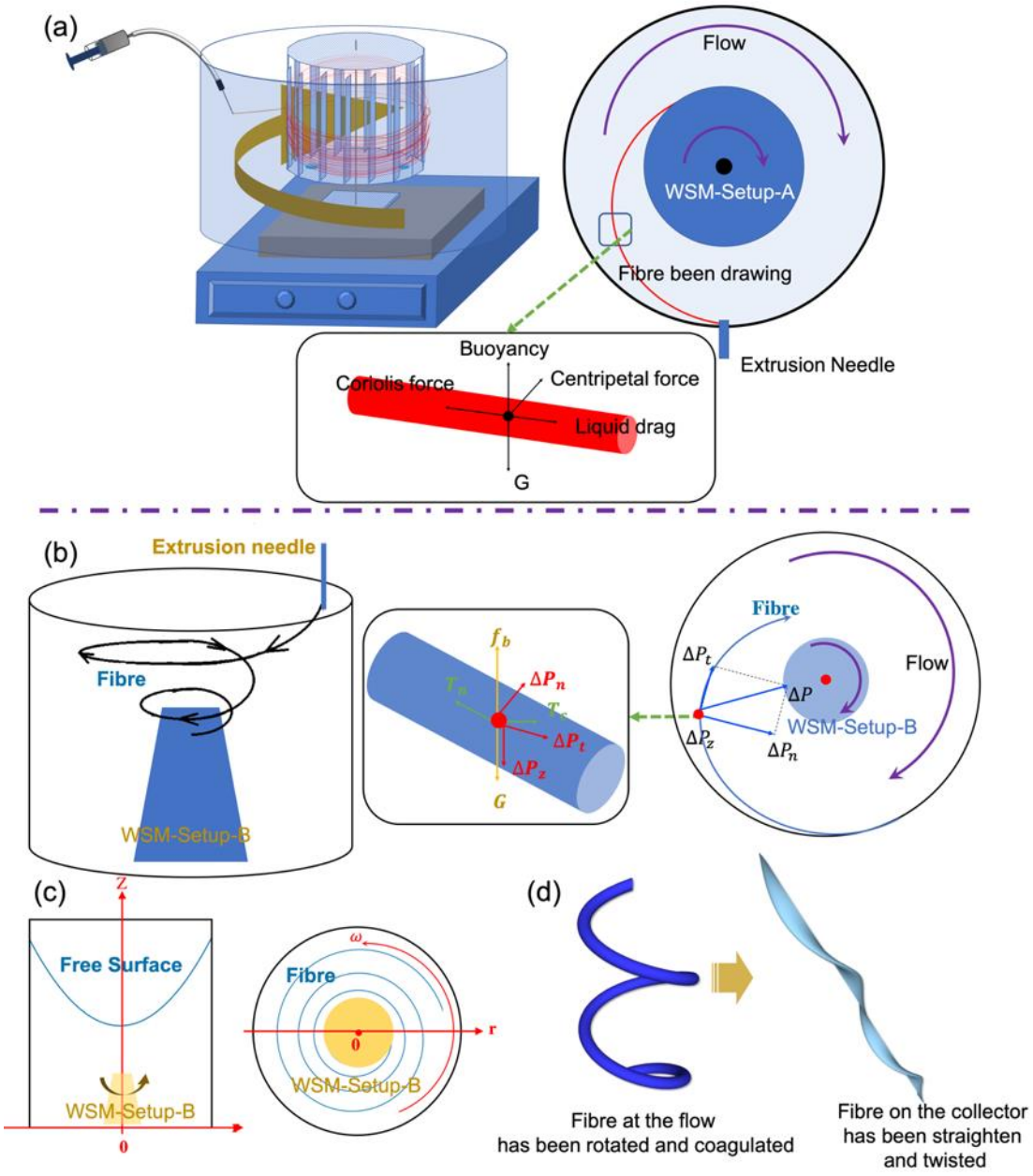

Fig. 3.2 The fibre extrusion process and force analysis of the fibre: (a) WSM Set-up A; (b-d) WSM Set-up B.

3.3.3 Alginate-based wheel-spun fibres

3.3.3.1 Alginate fibres from WSM Set-up A

Typically, for WSM Set-up A, the coagulation bath has a diameter of 20 cm, with the height of the solution surface at 12 cm, while the WSM itself has a diameter of 10 cm and a rotation speed of 45-60 rpm, with the extrusion needle placed at the edge of the coagulation bath.

3.3.3.2 Alginate fibres from WSM Set-up B

Typically, for WSM Set-up B, the coagulation bath has a diameter of 12 cm, with the height of the solution surface at 25 cm, while the WSM itself had a diameter of 6 cm, a rotator rotation speed of 60-120 rpm and an impeller rotation speed of 0-60 rpm, with the extrusion needle placed at the edge of the coagulation bath, no deeper than 5 mm from the surface.

3.3.4 Morphology of the wheel-spun alginate fibre

In this work, the twisting effect could be recognized simply using a SEM. The fibre with twisting effects shows a unique helix pattern on the surface of the fibre. This is because of the simultaneous twisting and coagulating. In Fig. 3.3, the morphology of each group of samples is presented. The SEM images indicate that only the fibres fabricated via WSM Set-up B have twisting effects, while a higher rotating speed can bring about more obvious patterns on the fibre's surface. In addition, the diameter of the fibre (Figure 3-4) should increase with a decrease in the rotation speed. In general, the fibre made by WSM Set-up A has a significantly smaller diameter than that from WSM Set-up B.

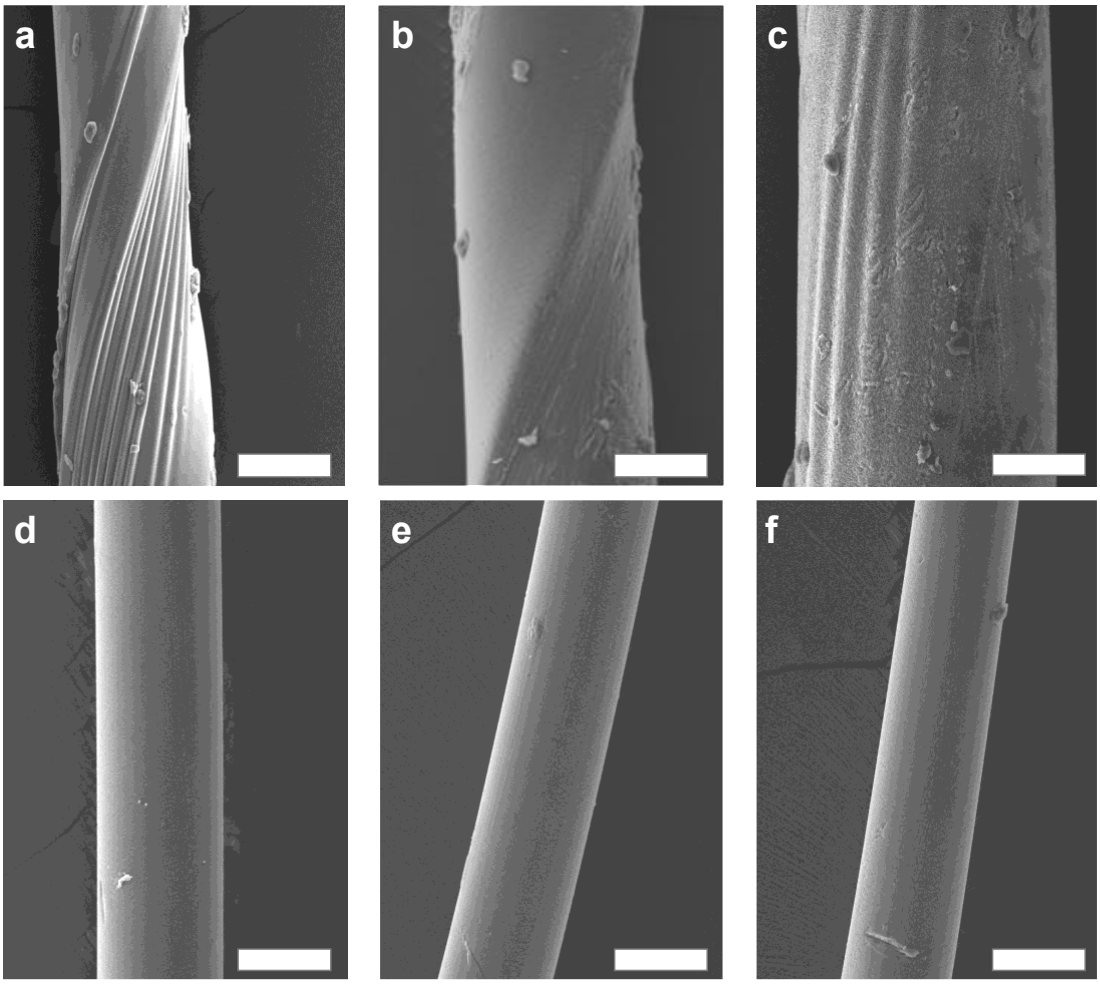

Fig. 3.3 SEM images for wheel-spun alginate fibre: (a-c) fibre fabricated via WSM Set-up B with a rotation speed (rotator/impeller) of 120/60, 90/45, 60/30 and 60/0 rpm; (e-f) fibre fabricated via WSM Set-up A, where the rotator rotation speed is 45 and 60 rpm; all bars = 100μm.

3.3.5 Mechanical properties of the wheel-spun fibre

The results of the wheel-spun alginate fibre's tensile performances are presented in Fig. 3.4. The fibre is classified into three groups: 1) The first group comprises Sample a, b and c, made using WSM Set-up B. 2) The second group comprises Sample d, made using WSM set-up B but without any flow effect (drawing and twisting); this group of fibre aims to simulate the traditional wet-spinning fibre. 3) The third group comprises Samples e and f, made by WSM Set-up A.

The tensile test indicates that the wheel-spun fibre possesses opposite properties with and without twisting effects. In Fig. 3.4b, the stress-strain curve presented, which refers to the samples in the first group, has an obvious yield point and a significantly higher strain than the remaining samples. The higher strain and level of Young's modulus and breaking stress bring a greater toughness to the twisted fibre. As Sample d displays similar fractured behaviour, unlike Samples e and f, this indicates that the key factor necessary to twist the fibre is the effect of the vortex generated by the impeller. Without the impeller, the fibre could not be twisted and drawn sufficiently; thus, it has the lowest performance among all groups. When comparing the fibres from Samples a, b and c, a higher impeller and rotator speed could bring about a higher breaking strain. However, the fibre in Sample b has the highest breaking stress, which indicates the extremity of the parameter setting.

WSM Set-up A, in our previous research [13], reveals itself to be a controllable property via changes to the needle gauge and alginate concentration. Further, in this current research, another factor has been found to change the fibre's mechanical properties, which is the rotator's rotation speed. The fibre in Sample f, with its higher rotation speed, has a smaller diameter, higher breaking strain and stress and a lower Young's modulus. All of those accord with the egg-box theory discussed in previous work (see Chapter 4 of the thesis).

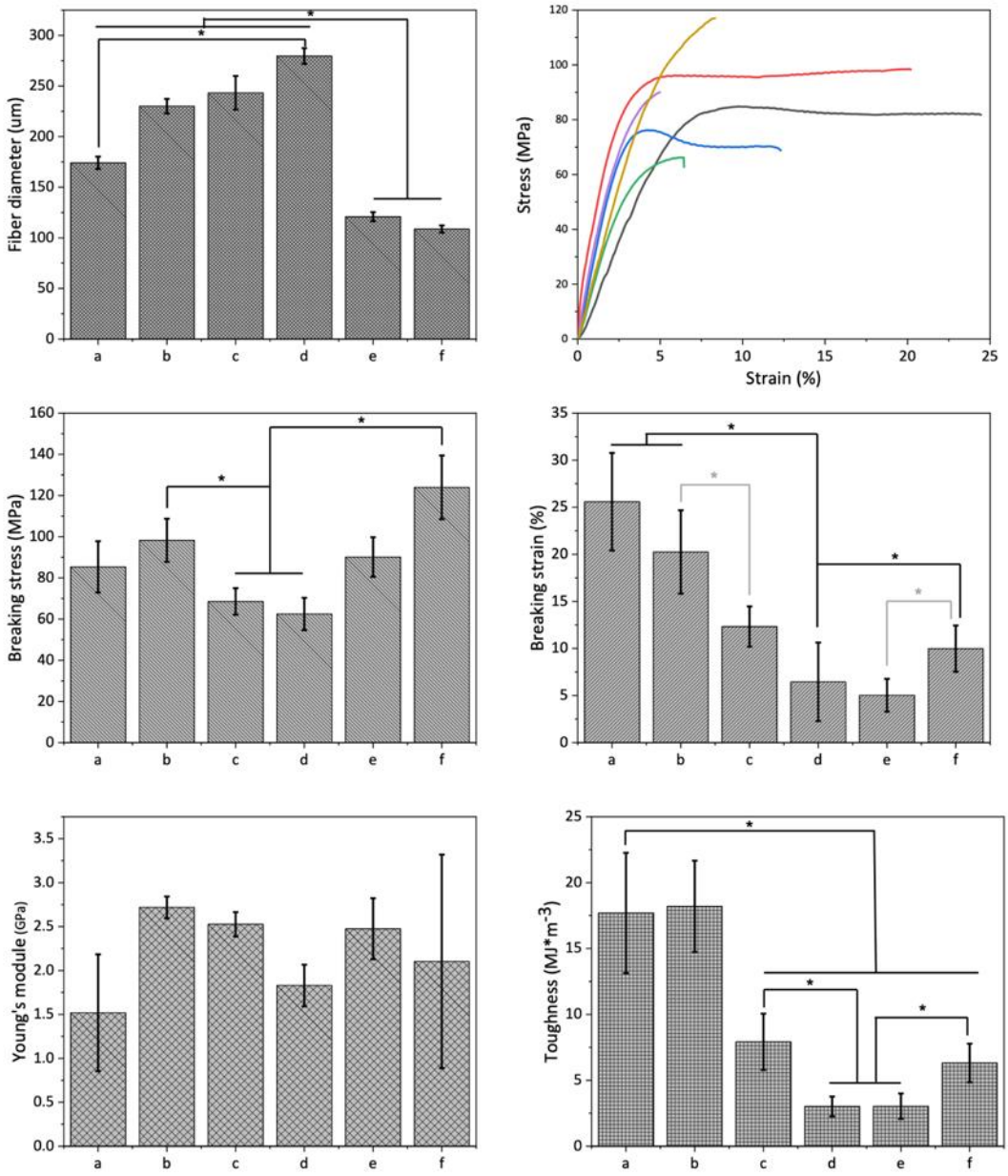

Fig. 3.4 Mechanical performance of wheel-spun alginate fibre with various parameters: (a) fibre's diameter; (b) stress-strain curves; stress (c) and strain (d) at breaking point; and Young's modulus € and fracture toughness (f).

3.4 Conclusion, limitations, and future work

3.4.1 Conclusion

In brief summary, two types of WSMs were designed by using EDM 3D printing technology in order to fabricate alginate-based fibre. Based on a theoretical analysis of each WSM set-up, both have good drawing effects, although Set-up B has uniquely controllable self-twisting properties. For Setup-A, the circulation generated by the motion of the blenders can draw the fibre in an accelerated manner, before being finally collected on the central collector. For Setup-B, the vortex generated by the rotation of the centrifugal impeller can draw the fibre down and move it to the middle of the coagulating bath with a logarithmic spiral trajectory. This trajectory, when created before the fibre is fixed onto the collector, will cause self-twisting effects.

The tensile properties of different alginate fibres made using both set-ups and various parameters have been presented, revealing significant differences. After interrogating the mechanical property changes in the fibre, drawing and twisting effects have also been demonstrated. Benefiting from these drawing and twisting effects, the wheel-spun alginate fibre has a higher strength and breaking strain than other alginate-based fibre, as reported recently. In addition, the twisting effects could further improve the strain of alginate fibre.

3.4.2 Limitations and future work

Although the fibre can be fabricated successfully, there is still much work to do in order to improve this research.

Firstly, because the alginate fibre is an amorphous polymer material, this means the drawing and twisting effects brought about by the wheel-spinning technique cannot perform effectively.

Although we have observed the morphology and tensile property changes with WSM-setup-B, the molecular arrangement, degree of crystallinity and orientation, which can change when using the wheel-spinning technique, cannot be measured qualitatively and quantitatively. In future research, the demonstration fibre should be changed from alginate to another crystallinity polymer such as silk fibroin, cellulose or PLLA.

Secondly, the mathematical model presented in this chapter does not include every situation that occurs during fibre fabrication. For example, in the current model, the flow speed and trajectory are identified as the fibre's speed and trajectory directly. However, the fibre, in fact, is accelerated by the shear force given by the flow, which means the speed of the fibre cannot be synchronized so it is the same as the flow. Rather, it should depend on the coefficient of viscosity for the coagulation solution, the density of the coagulation solution, the molecular weight of the polymer, the concentration of the extrusion solution, among others. For such a complex system, finite element analysis or multiphysics simulation should be introduced and applied.

Thirdly, the wheel-spinning technique should not restricted to the wet-spinning field, given that the core principle of the wheel-spinning set-up is to utilize the effect of flow to achieve *in situ* treatment of the fibre. Air is another flow besides liquid, while dry spinning or blow spinning are mature techniques in the textile industry as well. Therefore, introducing the wheel-spinning set-up to these fields, by using air flow to draw out and twist the fibre, is another worthwhile aim for the future.

References

[1] Silva, R., Vongsanga, K., Wang, X. & Byrne, N., 2016. Understanding key wet spinning parameters in an ionic liquid spun regenerated cellulosic fibre. Cellulose, 23(4), 2741-2751.

[2] Zhang, J., Seyedin, S., Qin, S., Lynch, P.A., Wang, Z., Yang, W., Wang, X. and Razal, J.M., 2019. Fast and scalable wet-spinning of highly conductive PEDOT: PSS fibers enables versatile applications. Journal of Materials Chemistry A, 7(11), 6401-6410.

[3] Gao, Q., Wang, M., Kang, X., Zhu, C. and Ge, M., 2020. Continuous wet-spinning of flexible and water-stable conductive PEDOT: PSS/PVA composite fibers for wearable sensors. Composites Communications, 17, 134-140.

[4] Zhang, H., Quan, L., Gao, A., Tong, Y., Shi, F. and Xu, L., 2019. The structure and properties of polyacrylonitrile nascent composite fibers with grafted multi walled carbon nanotubes prepared by wet spinning method. Polymers, 11(3), 422.

[5] Sayyar, S., Moskowitz, J., Fox, B., Wiggins, J. and Wallace, G., 2019. Wet-spinning and carbonization of graphene/PAN-based fibers: Toward improving the properties of carbon fibers. Journal of Applied Polymer Science, 136(36), 47932.

[6] Eom, W., Shin, H., Ambade, R.B., Lee, S.H., Lee, K.H., Kang, D.J. and Han, T.H., 2020. Large-scale wet-spinning of highly electroconductive MXene fibers. Nature Communications, 11(1), 1-7.

[7] Jeong, K., Kim, D.H., Chung, Y.S., Hwang, S.K., Hwang, H.Y. and Kim, S.S., 2018. Effect of processing parameters of the continuous wet spinning system on the crystal phase of PVDF fibers. Journal of Applied Polymer Science, 135(3), 45712.

[8] Chen, Z., Song, J., Xia, Y., Jiang, Y., Murillo, L.L., Tsigkou, O., Wang, T. and Li, Y., 2021. High strength and strain alginate fibers by a novel wheel spinning technique for knitting stretchable and biocompatible wound-care materials. Materials Science and Engineering: C, 112204.

[9] Yin, R., Tao, X. & Jasper, W., 2020. A theoretical model to investigate the performance of cellulose yarns constrained to lie on a moving solid cylinder. Cellulose, 27(16), 9683-9698.

[10] Liu, Q. & Parker, K.K., 2018. A viscoelastic beam theory of polymer jets with application to rotary jet spinning. Extreme Mechanics Letter, 25, 37-44. https://doi.org/10.1016/j.eml.2018.10.005.

[11] Schwartz, L.W. & Roy, R.V., 2004. Theoretical and numerical results for spin coating of viscous liquids. Physics of Fluids, 16, 569-584. https://doi.org/10.1063/1.1637353.

[12] Wu, Y., Li, C., Fan, F., Liang, J., Yang, Z., Wei, X. & Chen, S, 2019. PVAm nanofibers fabricated by rotary jet wet spinning and applied to bisphenol a recognition. ACS Omega, 4, 21361-21369. https://doi.org/10.1021/acsomega.9b02964.

[13] Chen, Z., Song, J., Xia, Y., Jiang, Y., Murillo, L. L., Tsigkou, O., ... & Li, Y., 2021. High strength and strain alginate fibers by a novel wheel spinning technique for knitting stretchable and biocompatible wound-care materials. Materials Science and

Engineering: C, 127, 112204.

Supporting information

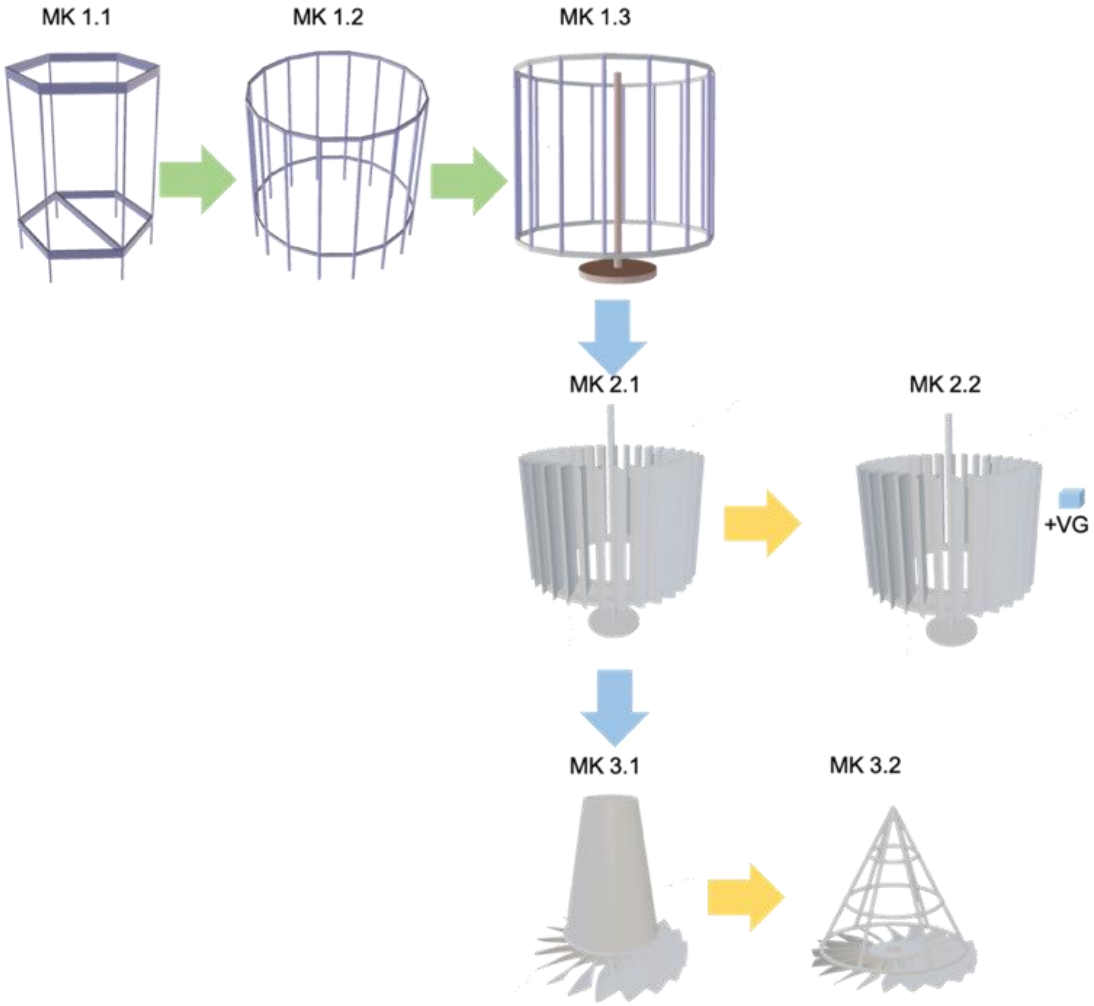

Fig. 3.5 The technology tree of the WSM.

In the main body, MK2.1 (WSM Set-up A) and MK 3.2 (WSM Set-up B) are discussed. The development of the WSM contains three key steps, set out as a technology tree in Fig. 3.5. The WSM can be classified according to three generations, from MK I to MK II and MK III. At the very beginning, we found that, if the extrusion solution is extruded into a beaker while the coagulation solution is stirred by a magnetic stirrer, the fibre can be obtained and gathered in the centre of the beaker. Based on this phenomenon, WSM MK I was fabricated, which is the initial version of the WSM. It is designed to collect the fibre via the vortex generated by the

magnetic stirrer. A hexahedral frame allows for the collection of the fibre, without causing any chaos. Further, some optimized designs were added, including an increase in the number of edges from 6 to 16, as well as additional casters and an axle for smooth rotation. The versions with these improvements are classified as MK 1.1, MK 1.2 and MK 1.3. MK I first improved the stability and dynamic range of the fibre-spinning process, after which MK II was designed and fabricated. In this version, the flow is not derived from the stir bar, but by using the blender placed behind the edge of the WSM. MK II also creates a circulation during its rotation. The flow goes into the interior of the WSM via the intervals on each edge, then exits from the holes at the bottom of the machine. When the fibre is extracted into the bath, the flow circulation guides the fibre to the machine in order to achieve a drawing effect and collection *in situ*. MK 2.1 and MK III have been designed and fabricated to achieve the fibre's twist effects. MK 2.1 is based on the original MK II but places a vortex generator in front of the extrusion needle. MK III is a new-design machine, consisting of an impeller in the lower part and a circular truncated cone in the higher part. MK 3.1 rotates with in a cylindrical bath, with the impeller causing a forced vortex to draw and spin the fibre before it is collected on the cone collector. MK 3.1 experienced a problem with fibre collection, because the linear velocity of the roller must be slower than the velocity of the flow due to the properties of the vortex. MK 3.2 was introduced to resolve this problem. This version generates a co-axial structure for the blenders and the roller, with the roller's rotation speed greater than that of the blenders, although both can be adjusted independently.

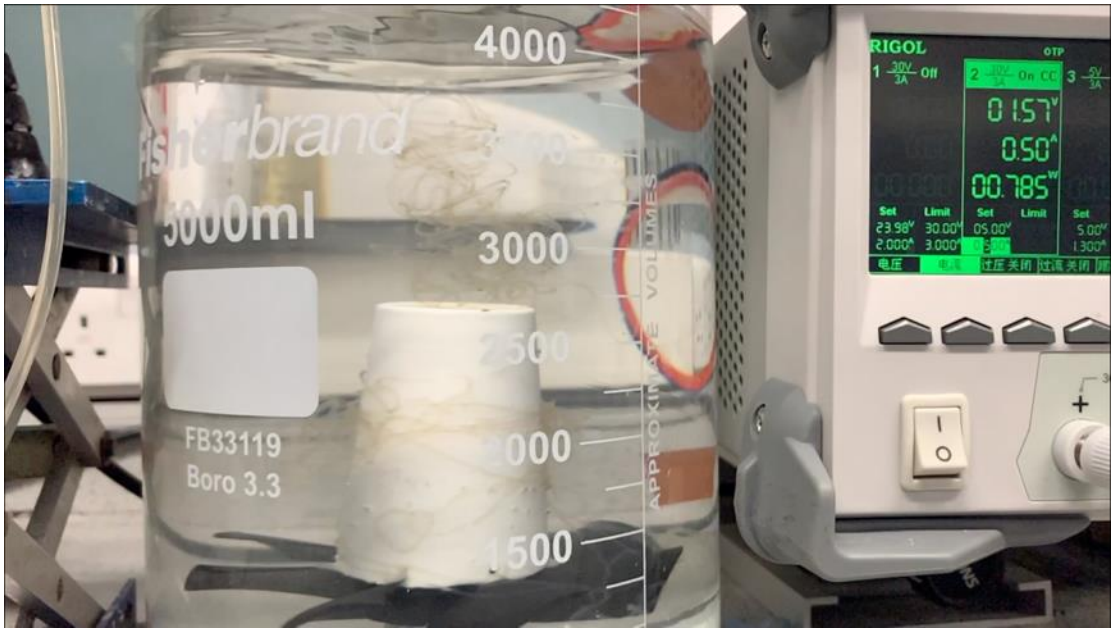

Fig. 3.6 A failed example of spinning via MK3.1. The rotation speed of the roller and blenders causes the collection speed to be slower than the vortex's linear speed at the centre, which leads to chaotic consequences for the fibre.

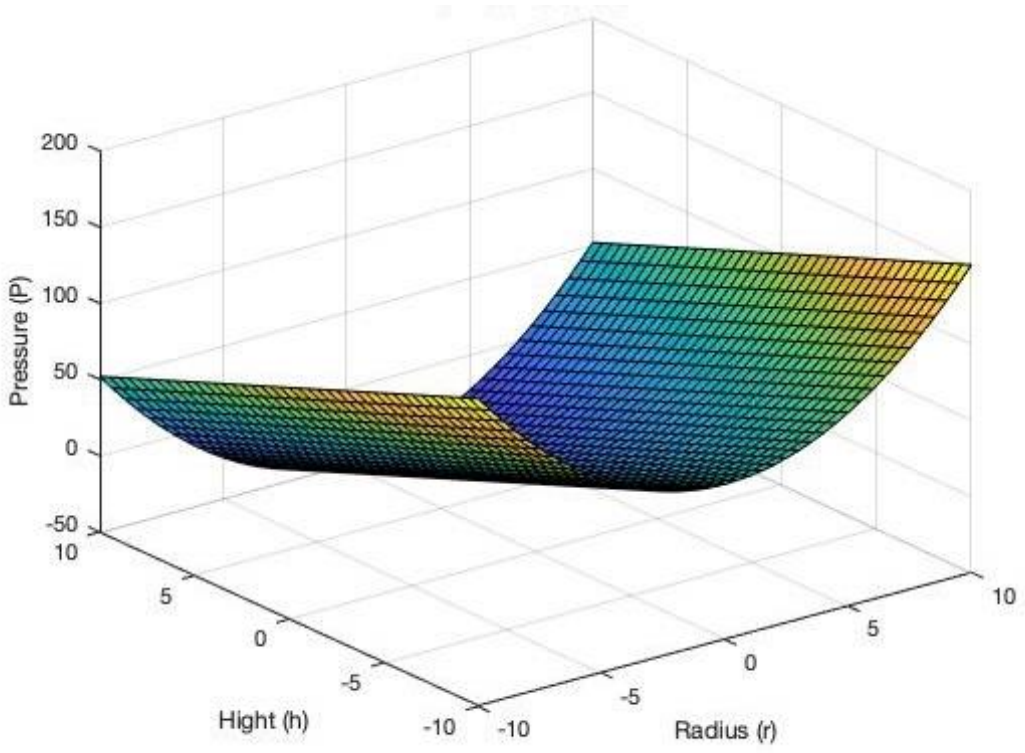

Fig. 3.7 Flow pressure under WSM rotation.

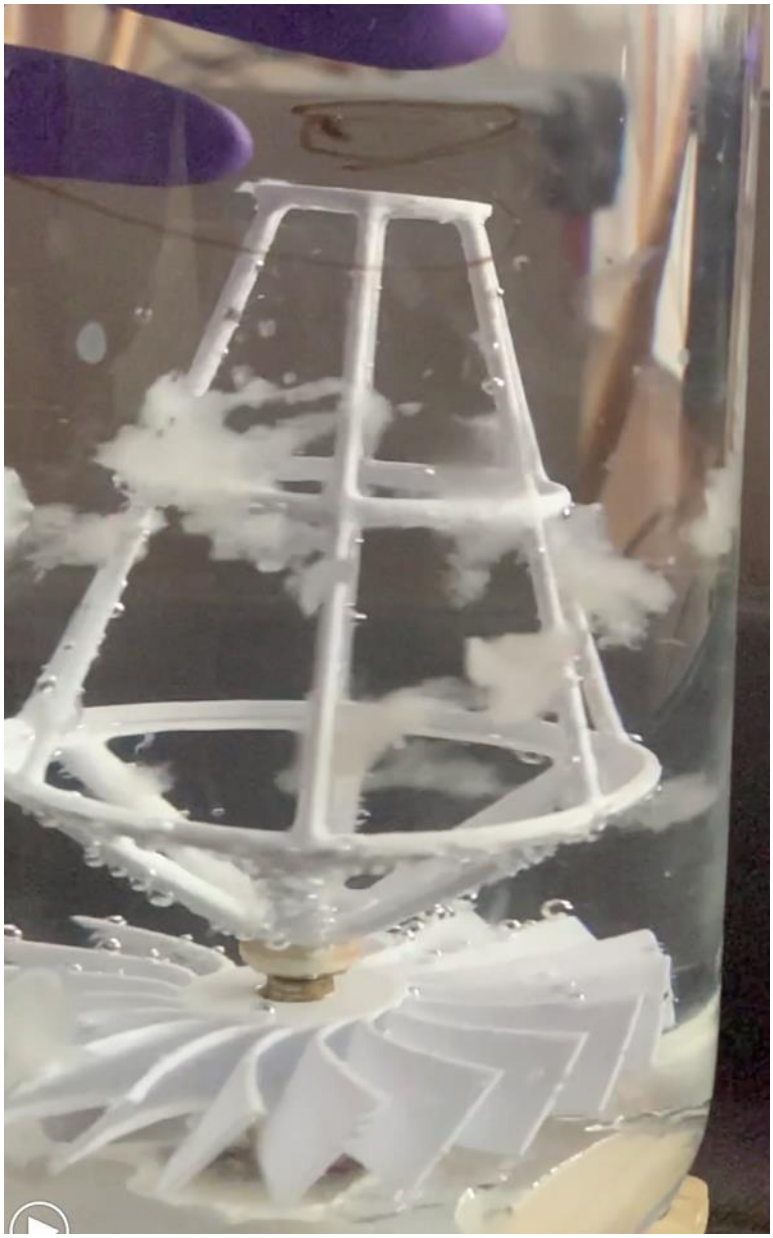

Fig. 3.8 The WSM’s twisting effect.

Chapter 4 High strength and strain alginate fibres by a novel wheel spinning technique for knitting stretchable and biocompatible wound-care materials

This chapter focuses on the third objective. The research has been completed and published at Materials Science and Engineering: C.

Authors: Zhongda Chen, Jun Song, Yumin Xia, Yuwei Jiang, Luis Larrea Murillo, Olga Tsigkou, Tao Wang, Yi Li

Journal: Materials Science and Engineering: C (2021)

DOI: https://doi.org/10.1016/j.msec.2021.112204

My contributions: I have prepared pure alginate fibres via WSM, designed all the experiments including fibre twisting, knitting fabrication, and done characterizations for the fibre. I also prepared the tables, the figures and the whole manuscript.

Co-author contributions: Mr. Jun Song supported the design of experiments, the presentation of data and the journal article. Mr. Yumin Xia supported the WSM design and relevant tensile tests. Miss. Yuwei Jiang supported the knitting fabrication and relevant PBS storage and degardation tests. Mr. Luis Larrea Murillo supproted the cell work and consequent characterizations. Prof. Tao Wang and Dr. Olga Tsigkou supported the design of in vitro study. Prof. Yi Li supervised the whole project in this section, and reviewed the manuscript.

Abstract

Alginate fibrous materials have been applied as wound dressing to enhance wound healing due to its nontoxic, biodegradable, and hemostatic nature. Conventional nonwoven fabrication tactics, however, showed weakness in inflammation, degradation stability and mechanical properties. Herein, the wet-spun alginate fibers were prepared by a novel wheel spinning technique, then knitted into wound dressing. Benefiting from optimized wet spinning parameters and the agglomeration of alginate multimers, the fibers were endowed with elevated mechanical performances and biodegradability, which allowed for the feasibility of knitting wound-care materials. Using the new wheel spinning technique, high strength alginate fibers with 173 MPa were produced with breaking strain up to 18% and toughness of 16.16 $MJ*m^{-3}$. Meanwhile, alginate fibers with high breaking strain reaching 35% were produced with tensile strength of 135 MPa and toughness of 37.47 $MJ*m^{-3}$. The overall mechanical performances of these alginate fibers with high breaking strain are significantly higher (up to 2 times) than those published in the literature in term of toughness. *In vitro* degradation evaluation revealed that this wet spun fibrous dressing had good aqueous absorbency (50%) and sustained biodegradation properties. Furthermore, the consequent cell viability study also proved that this alginate knitted fabric is biocompatible for being applied as wound dressing.

Keywords

Alginate hydrogel, wound-care, materials, wet spinning, knitting, egg-box dimers

Highlights

- A novel optimized wheel spinning device was introduced to prepare and collect wet spun alginate fibers.
- The observed nanospheres inside wet spun alginate fibers were consisted agglomerated egg-box multimers.
- The high strength and breaking strain alginate fiber brought forward the possibility of knitting into wound-care materials.
- *In vitro* study proved the good biodegradation and biocompatibility of alginate wound-care materials.

4.1 Introduction

Wound dressing has been regarded a clinical and daily consumable to protect and regenerate injured skin tissue for thousands of years [1,2]. Current wound dressing strategies always involve functionalized anti-infective or inflammatory components, depending on whether the wound is chronic or acute [3,4]. Developing topological formulations including sponges, films, bandages and nano/micro fibers is another focus for improving present therapeutic modalities [5–7]. Alginate nonwoven fabric is one of the mainstream dressing products especially for acute wounds [8]. However, nonwoven alginate hydrogel pads, as forms of mature wound dressing, suffered from poor mechanical properties, nor are they able to withstand external damage [9,10]. Further, the non-woven structure results in an unsatisfactory tissue adhesiveness due to a poor young's modulus, low toughness and highly rough morphology [11,12].

Regarded as a replacement option, wet spinning is a reliable technology in biomaterial manufacturing [13]. Widely recognized for being a traditional textile technique, the efficacy of wet spinning has been proven in the case of manufacturing biomedical polymers from single fiber to 3D scaffolds and even in cellular structures [14,15]. It is also favored due to alginate's resemblance of a hydrogel matrix texture and stiffness, which is comparable to the extracellular matrix though this could lead to another drawback concerning nonwoven dressing, namely, poor degradation behaviors [16]. Profiting from the topological structures, knitting fibrous fabric could kept highly stretchable structure and elastic modulus during dressing period towards transitional clinical applications [17].

As a typical natural polysaccharide extracted from *Sargassum*, alginate has had many applications in the textile, food, and biomedicine industries [18]. Alginate meets the criteria for good biocompatibility, biodegradability and hemostatic properties [19]. Due to alginate fibrous fabric can interact with wound effusion caused by tissue fluid leakage, as well as generate hydrophilic sodium alginate/calcium alginate gels when alginate comes into contact with the wound. This fabric can also allow oxygen to pass through, while blocking bacteria in order to maintain a productive environment for new tissue generation [20,21]. Furthermore, epithelial cells move faster towards a wounded area in a moist environment, which alginate fabric can create and sustain, than under dry conditions [22]. When compared with knitting fabric, the nonwoven form has a higher level of infilling at the same volume, causing the enrichment of calcium ions at the wound site, which can inhibit the healing process [23]. Thus, alginate fibrous fabrics are widely accepted as biomaterials for medical suture, wound dressing, and artificial skin purposes.

In this work, four groups of wheel spinning fibers were prepared and characterized with different alginate concentrations and needle gauges. Then, two groups of fibers with better performance can be granted to knit four groups of fabrics. Mechanical performances, degradation behaviors and cell viability were characterized in order to confirm the feasibility of this potential wound-care material and optimize the best parameters.

4.2 Materials and Methods

4.2.1 Materials and wheel spinning fibers

Sodium alginate powder (NaAlg, W201502) and calcium chloride ($CaCl_2$) were purchased from Sigma Aldrich, MO USA, and used as received. The alginate fiber was prepared on application of the optimized wet spinning method. Briefly, $CaCl_2$ aqueous solution was chosen as a coagulation bath. A schematic diagram of the wet spinning system set-up is presented in Figure 1a. Sodium alginate was dissolved in deionized water with a concentration of 20 or 50 g/L and stirred for 3 h to obtain a 2% and a 5% NaAlg solution (w/v). The NaAlg solution was then inserted into the syringe pump and extruded into a 2% $CaCl_2$ coagulation bath via a needle with a 0.5 mm (25G) or a 0.8 mm (21G) diameter tip. The injection speeds were 2 ml/min for the 25G needle and 3 ml/min for the 21G needle due to the difference in needle diameter. After being drawn and collected by a roller in the coagulation bath, the each single NaAlg fiber was washed twice by deionized water and dried on a fume board for further conditioning and testing (ISO 139:2005). The 2% NaAlg solution with the 21G and 25G needle were named as A1 and A2 sample group, and 5% NaAlg solution with 21G and 25G needle were named as A3 and A4 sample group. The Table 1 also demonstrated the parameters of fiber groups.

Table 1. The sample groups of wet spun alginate filaments.

	21G needle	25G needle
2% alginate solution	A1	A2
5% alginate solution	A3	A4

4.2.2 Yarns twisting

The direct counting method was applied to prepare the pure alginate yarn (ISO 2061:2015) [24]. NaAlg filaments were firstly soaked in deionized water for 2 min in order to remove static electricity and soften the surface of the filaments. Then, four, eight, or sixteen filaments were combined and twisted at 50 twists length in deionized water. Based on yarn's linear density (Tt) and the required twist factor (αt), the standard twists (*Tt*) could be calculated by equation (1).

$$Tt = \frac{\alpha t}{\sqrt{Tt}}, \quad (1)$$

4.2.3 Alginate dressing knitting

Four sample groups were designed for the alginate knitting fabrics. The knitting sample for group A3 was made by four or eight dry filaments. Due to the thinner and lower in toughness of A4 group of filaments, the knitting sample for this group was made by eight and sixteen dry filaments. The NaAlg wound dressing was knitted into a 1×1 rib derivate fabric via weft knitting. The wale density was 10 loops per 10 mm, and the course density was 12 rows per 9 mm. The knitting sample groups were marked according to fiber groups/twisting strands, i.e., A3/4, A3/8, A4/8, and A4/16.

4.2.4 Wound dressing performances evaluation

The Fourier transform infrared (FT-IR) spectra of fibers were measured by FT-IR spectrometer (Nicolet 5700, WI USA) with a Smart Orbit probe in the wavelength range from 400 to 4000 cm^{-1} in transmittance mode. The optical images of knitting fabric samples were taken by Nikon D810 single-lens reflex camera. The morphology of the fibers and knitting fabric samples, before and after the degradation experiment, was observed after vacuum platinum coating with use of Zeiss EVO 60 and Ultra 55 scanning electron microscopes (SEMs), Germany. The mechanical performances of the dry filaments and fabrics was characterized by a universal materials tester (Instron 5566, MA USA) at a crosshead speed of 5 mm/min.

The water storage ability of knitting fabrics was tested by immersing samples into a phosphate buffered saline (PBS) solution at room temperature for 30 min. Then, the wet sample was blotted with filter paper to remove any liquid on its surface. The water storage rate of the knitting fabric was determined by formula (2), and the water absorbency rate of knitting fabric was determined by formula (3).

$$R_{\text{storage}} = \left(\frac{w_1 - w_0}{w_0}\right) \times 100\%, \quad (2)$$

$$R_{\text{absorbency}} = \left(\frac{w_2 - w_0}{w_0}\right) \times 100\%, \quad (3)$$

Where w_1 is the weight of the sample full of liquid, w_0 is the weight of the pristine dry sample before immersion into the PBS solution, and w_2 is the weight of the sample which has been sopped of water. Each group had five samples to avoid experimental errors.

4.2.5 *In vitro* degradation

The knitting sample degradation behavior in PBS was determined by a temperature-controlled water bath shaker, set at a shaken rate of 55 times/ min and 33 ℃ [25], order to simulate a

wound surface environment. Weight loss on day 1, day 7, and day 14 was calculated by following formula (4).

$$R_{\text{weight loss}} = \left(\frac{w_3 - w_4}{w_3}\right) \times 100\%, \quad (4)$$

Where w_4 is the weight of the dry sample after the degradation test and w_3 is the weight of the pristine dry sample before the degradation test.

4.2.6 *In vitro* biocompatibility study

4.2.6.1 Cell culturing

NIH 3T3 cells were selected to study the cytotoxicity of the alginate knitting wound dressings. Briefly, the alginate fiber and fabric wound dressings were directly soaked in Dulbecco's Modified Eagle Medium (DMEM) at 37 °C at a concentration of 0.1 g/mL for 1 day. 3T3 cells were cultured into the wells with fabric samples and the blank control group, at a density of 7,000 cells per well for days 1, 4 and 7. The fabric was cut into round samples with a 15.6 mm diameter to fit the 24-well plates.

4.2.6.2 Cell viability and morphology

The cell viability and morphology were presented via Alamar blue assay and diamidino-2-phenylindole (DAPI, D9542, Sigma-Aldrich, Germany)/Phalloidin (ab176753, Abcam, UK) staining. Each group of cell viability evaluations was repeated five times. Cell morphology was observed by phase contrast light microscopy (Jena, Zeiss, Germany) at day 1, 4 and 7.

4.2.7 Statistics

The results of mechanical performances, degradation and cell viability were presented as means

± standard deviations. Statistical differences amongst sample groups were processed by Student's t-test in IBM SPSS (Ver. 24.000) using the least significant difference. Differences were considered significant (*) when $p < 0.05$, and very significant (**) when $p < 0.01$, and ultra-significant (***) when $p < 0.001$.

4.3 Results and Discussion

4.3.1 Wet spun alginate fibers

4.3.1.1 Surface morphology

Wet spinning is a technique that involves the extrusion of a macro molecular solution directly into a coagulation bath [26]. In this work, a novel wet spinning set-up, referred to wheel spinning machine (WSM), could create circulation during its rotation, which guided the fiber ejecting from the extruder to the coagulating bath. As the schematic diagram in Figure 1a shows, the trajectory of fiber followed a logarithmic spiral due to the Bernoulli's Principle [27,28]. This mechanism brought fiber a modest and continuous drawing rather than the instability of traditional wet spinning, lead to a better performance of fiber.

Four groups of fiber sample made by WSM were fabricated and characterized, then classified according to differences in alginate concentration and needle gauge. The change in needle gauge brought about differences in diffusion rate and the volume of calcium ions. The fiber was collected by a roller at a constant speed, and different needle gauge and extrusion speeds resulted in different drawing rates. Thus, the fibers fabricated via the same alginate concentration had similar diameters (Fig. 4.9-10).

The pristine alginate fiber is a smooth and flat single fiber without any spots or holes, as can be seen in the SEM images in Figure 1b. With greater magnification, some striped ditches on the filaments were observed, although this morphology did not affect the uniformed filaments' surface (Fig. 4.1b, d). Figure 1c presents the cross-section of the filament. The SEM image, with higher magnification, of the cross-sectioned NaAlg fibers revealed that alginate had a kind of porous structure, as shown in Fig. 4.2 c, e.

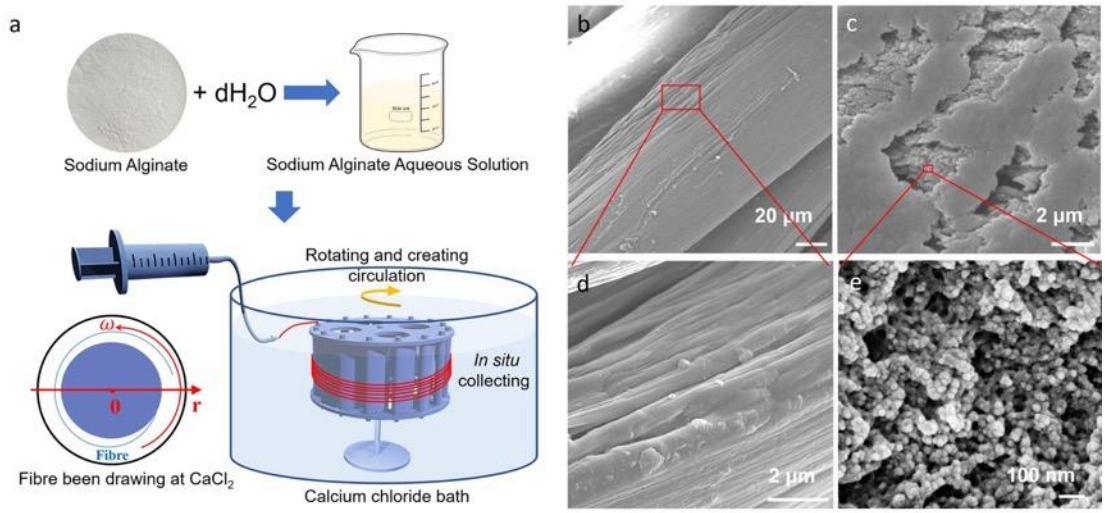

Fig. 4.1 Schematic diagram of wheel spinning and SEM images of pristine alginate filaments (a) The fiber was drawn and collected using by an optimized device. The trajectory of the fiber follows a logarithmic spiral. The surface morphology (b, d) and cross-section surface morphology (c, e) of wheel spinning alginate fiber.

Fig.4.9 indicates the diameter of each group of single fibers. The diameters of the single NaAlg fiber are located in the range of 40 μm - 80 μm (Fig. 4.10). The diameter of fiber was significantly affected by solution concentration. Only 5wt% alginate shows difference in fiber diameter when spinning via different sizes of needle. To further calculate wet-spun fiber parameters, the flow velocity was approx. 67 cm/s from 25G and 25 cm/s from 21G needle. The wheel spun drawing approx. 400 cm/s in coagulation bath, which means the drafting rate

of fiber from wheel was 5.9 times (25G) and 16 times (21G). This calculated result consists with previous drafting rate (7.5 times) reported by Foroughi *et al.*, [29].

4.3.1.2 Mechanism of wet spinning fabricating process

In this work, with the effect of Ca^{2+} during the wet spinning process, the calcium-dependent gelation of alginate could be formed via the cross-linkage of lateral egg-box dimers in different alginate molecular chains. When sodium alginate solution was squeezed into a calcium chloride bath, the buckle of the glucuronic acid unit acted as a two-dimensional structure, similar to a corrugated egg-shaped box, with gaps that could encapsulate and coordinate calcium ions (Fig. 4.2). As Figure 2 shows, the alginate chains consisted of a mixture of guluronic acid (GulA) and mannuronic acid (ManA), linked via (1→4) glycosidic linkages.[30] Within all three types of alginate subunit, only GulA/GalA units were able to form egg-box dimers. Based on the egg-box theory optimized by Mackie *et al.* in 1983, [30] GulA/GalA units create regular geometric holes arranged antiparallel to each other and allow the Ca^{2+} to be embedded through coordination with six sugar epoxy atoms (O2, O3, O6′). An egg-box based gelation of alginate was created with the participation of Ca^{2+}, a stable cross-linkage only formed by 6-8 continuous GulA [31]. From the SEM image in Figure 2 taken from alginate fiber's cross-section, it can be observed that the fiber comprised large numbers of nanospheres with diameter of 20 - 30 nm, which could be understood as the agglomeration of egg-box multimers. Given the low affinity towards Ca^{2+}, ManA affected the formation of lateral associations of egg-box multimers [32]. The polymerization and aggregation properties of alginate helped the calcium ions stick together strongly, forming a robust gel construction, as presented in Fig. 4.2. Thus, GulA

dominated the mechanical strength while ManA led to the gel elasticity and syneresis of the fiber [33,34]. Apart from the molecular length and distribution of calcium-binding blocks, the most effective factor in the fiber's mechanical properties was the concentration of alginate and calcium ions [35,36].

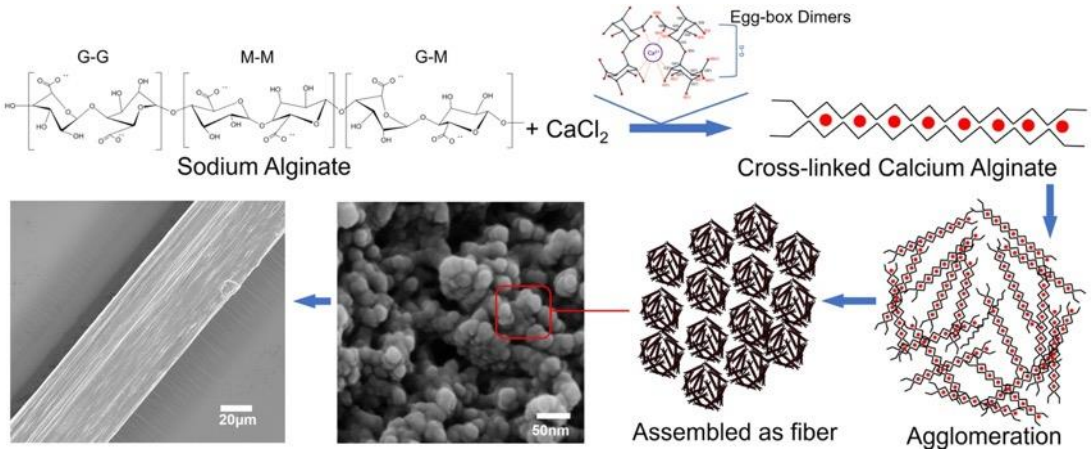

Fig. 4.2 The molecular-level mechanisms of alginate wet spinning fiber processing. The chemical reaction between the sodium alginate and calcium chloride solution; egg-box dimers formed by the specific alginate subunit; alginate molecular agglomeration and assembling towards cross-sectional SEM images of alginate fiber and single fiber.

The chemical change in the wet spinning process was characterized by identifying the shift in the chemical bonds in alginate molecules via FTIR spectra investigation. Figure 3a illustrates the FTIR spectra of the NaAlg powder and filaments, which were wet spun using 2% and 5% alginate solutions. The formation of hydrogen bonds, especially intramolecular hydrogen bonds, tended to shift the absorption frequency towards a lower wavelength and to increase the intensity and width of the absorption peaks [37]. The characteristic absorption band appeared in the range between 3400 cm^{-1} and 3200 cm^{-1} standed for the -OH stretching and the presence of glucose residues. Asymmetric and symmetric bands of carboxylate anions produced intense stretching vibrations of around 1600 cm^{-1} and 1430 cm^{-1}. Replacement of the sodium on the surface of the filaments with calcium was evidenced by the peaks shifting from 1592 cm^{-1} to

1621 cm^{-1} and from 1407 cm^{-1} to 1430 cm^{-1} or 1436 cm^{-1} in the spectra of the NaAlg powder and two fiber samples [38]. Specifically, the charge density and the radius of the atomic weight difference for these two kinds of cations caused the characteristic peaks to shifts.

The XRD pattern is given in Fig. 4.3b. As a kind of macromolecular polysaccharide, the alginate fibers maintained a relatively low crystalline state. However, the two broad diffraction peaks were still observed in the curves. The first diffraction peak at around 13.4° and the d-spacing was 0.66 and 0.68 nm for the 2% and 5% alginate fibers, could be attributed to the lateral packing among the molecular chains [39]. The other diffraction peak was located at around 22.9°. Comparing the relative intensities of these two diffraction peaks, the 5% alginate fiber had a slightly higher crystalline content level than that of the 2% specimen.

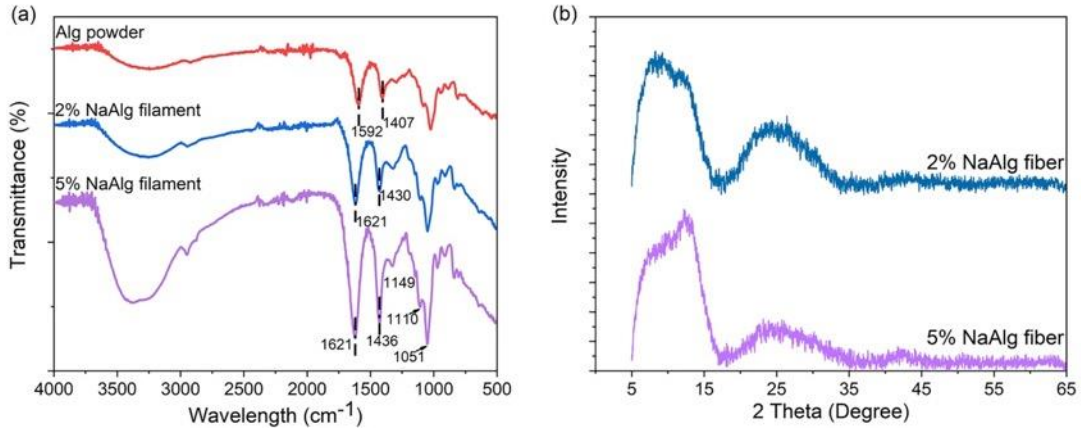

Fig. 4.3 FTIR & XRD of wet spun alginate fibers. (a) FTIR spectra curves of alginate powder and 2%, 5% wet spun alginate fibers; and (b) XRD patterns of 2% and 5% wet spun alginate fibers.

4.3.1.3 Strength and strain of the alginate fibers

During the fiber spinning process, four groups of fibers with different needle size and alginate concentrations were designed in order to investigate the influences on fibers' mechanical performance according to these parameters. Figure 4a demonstrated the typical stress-strain

curves of four groups of fibers. Fig. 4.4b, 4c highlighted the breaking stresses and strains for four groups of alginate fibers. The Fig. 4.5 reviewed some typical works of wet spun alginate fibers. It could be found the stress-strain curves in Fig. 4.4a was consistent with the curves of previous reports. The previous works tended to fabricate nanomaterials reinforced alginate fibers to enhance their mechanical performances [40,41]. However, those composite fibers did not achieve a balance between applicable breaking stress and strain, consequently those fiber were short of enough toughness suitable for specific applications. It should be noticed that most of previous studies only presented the stress and strain at breaking point, but the alginate fibers towards wound dressing seldom be broken when it was applied. The yielding behavior in the strain-stress curves should be paid more attention than that of breaking points, as it is highly related to the toughness of the fibers. In Fig. 4.4d, Young's modulus, and fracture toughness for four fiber groups were calculated and found to be in line with basic expectations. Yield strain for four groups fibers did not significantly different which indicated they had similar crystalline state and elastic stretch zone. The A4 (5 wt%, 25G) group had the highest yield stress (116 MPa) while the other groups had similar stress from 78 to 82 MPa. The A3 (5 wt%, 21G) group had the longest breaking strain (35%) while the other three groups had similar strains from 16% to 22%. The A4 group had the highest breaking stress (173 MPa) while the other groups had similar stress from 128 to 135 MPa. Thus, it can be stated that breaking stress and fracture toughness were increased due to the higher concentration of alginate in the extrusion solution, since the more polymer within the fiber, the tighter inner structure became.

Both A1 and A3 (21G) groups showed a significant higher strain rather than A2 and A4 (25G) groups, which indicated a larger needle size contributed to a higher strain by providing fiber an

unconsolidated structure. Overall, A1 and A2 (2 wt%) groups had mediocre and similar results in yield point, braking stress, Young's modulus and toughness. But A3 and A4 (5 wt%) groups had higher and opposite results, A3 was better in strain and toughness, while A4 was better in stress and Young's modulus. Considering the fibers with a high strain or stress and sufficiency were suitable for the further knitting process, group A3 and A4 were selected for knitting fibers.

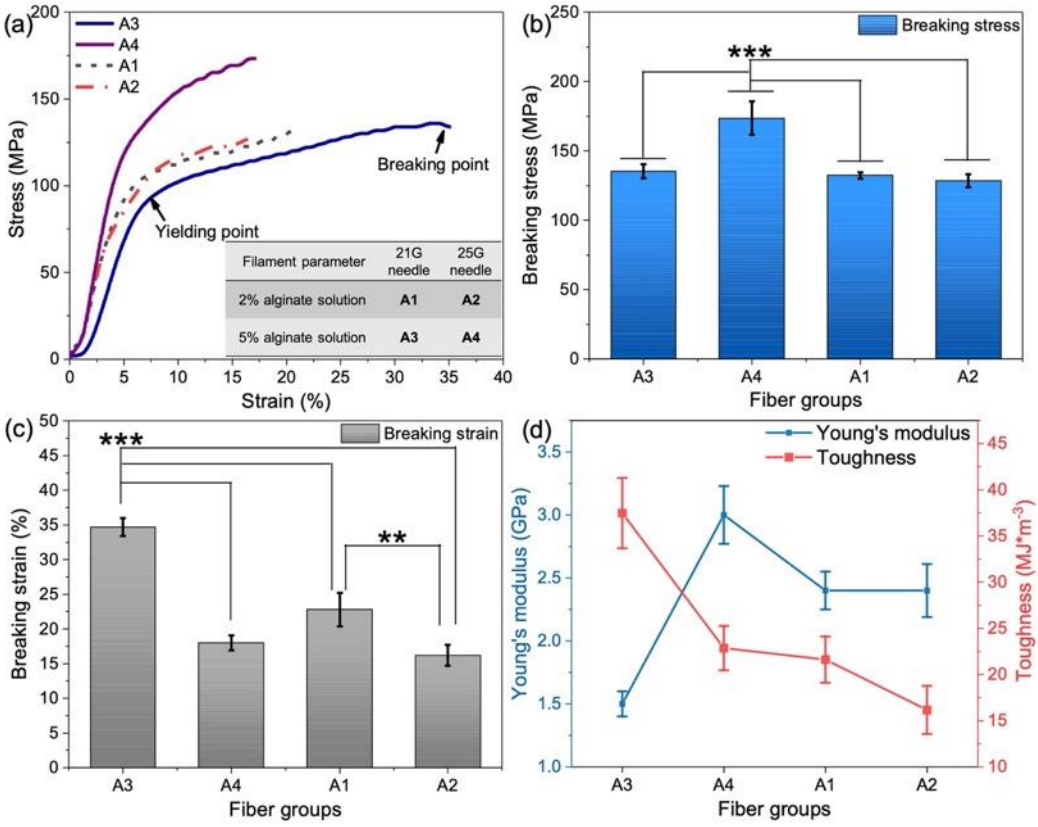

Fig. 4.4 Mechanical performances of four fiber groups: stress-strain curves (a); stress (b); strain (c); and Young's modulus and fracture toughness (d).

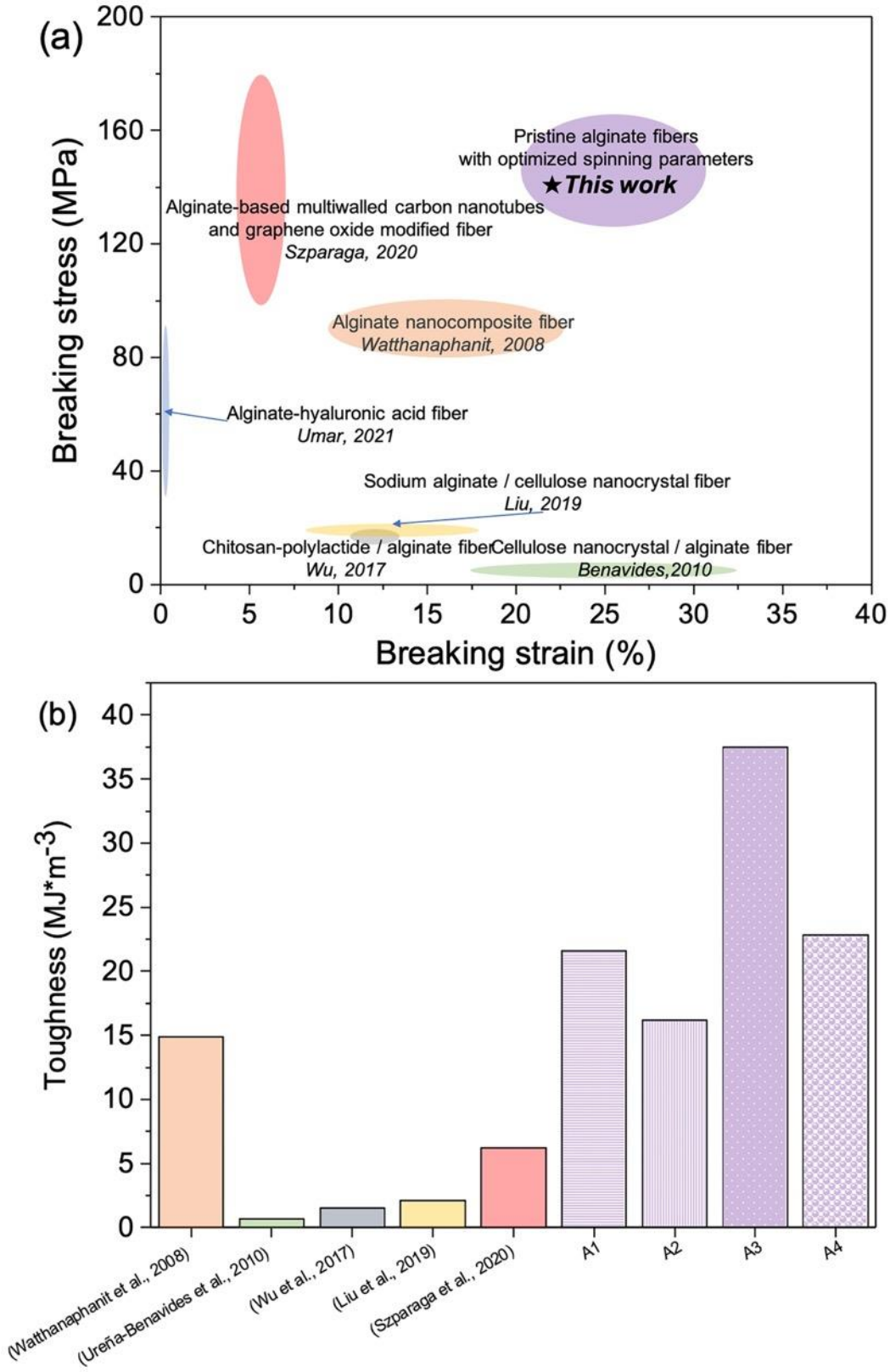

Fig. 4.5 The bubble chart and bar chart of comparison for previous studies and this work. (a) The bubble chart comparison of breaking stress and strain; (b) bar chart of comparison of toughness for previous studies and this work. (Watthanaphanit et al., 2008, Ureña-Benavides et al., 2010, Wu et al., 2017, Liu et al., 2019, Szparaga et al., 2020, Umar et al., 2021).

4.3.2 Alginate knitted fabric

4.3.2.1 Knitted fabric morphology

In the textile industries, the multiple-strand fiber often needs to be twisted before knitting, However, it is difficult to knit highly twisted alginate filaments. The knitting process always requires high toughness fibers due to the repeating bend into coils and loop the coils around each other. Conventional alginate fiber cannot meet this criterion. As a result, only very limited twisting steps were performed in this work. For the knitted alginate structure, the specimens were made up of loops enmeshed with each other; see the SEM results in Fig 4.6a-h.

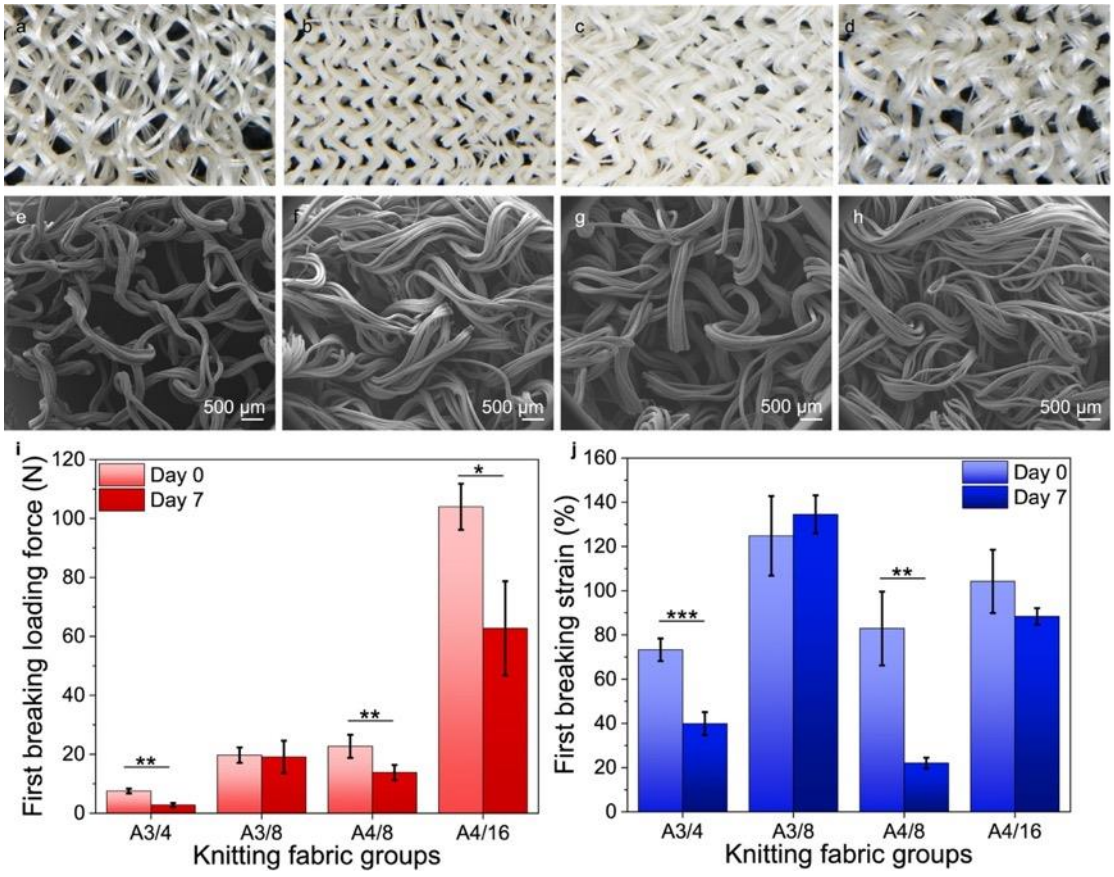

Fig. 4.6 Optical and SEM images of NaAlg knitting fabrics for the A3/4 group (a, e), the A3/8 group (b, f), the A4/8 group (c, g), the A4/16 group (d, h) and absorbency ability of the knitted samples in the tensile test for knitting fabric before and after degradation in PBS for seven days (i, j).

4.3.2.2 Tensile strength of knitted fabrics

The tensile strength of the four groups of samples is given in Fig. 46i, j. As the fabric thickness was difficult to control during the loading tests, the strains and loading forces are presented as tensile strength results. The load-strain curve showed zigzag shapes (Fig. 4.14). As shown in Fig.s 4.6a-d and 4.13, the loops in each row were connected with the loops in the next row, and the loading force of each loop was different during the stretching process of the knitting fabric. Due to the high elasticity of the knitted structure, the first loop that straightened broke because it was under the strongest force. When the loop was broken, the load force of the tensile machine dropped sharply. As the multi-strand yarn used in this experiment had not been tightly twisted, the yarn gradually broke one by one in the process of a loop breaking.

For the results of the dry samples which were obtained before the degradation test, the peak value for the load force in the A3/4 group of the sample (8N) was the lowest amongst the four groups. Comparing the yield strains and loading forces of the four groups of samples, it was concluded that the loop strength of the sample with a smaller number of strands was weaker if the same yarn was used. The loops broke quickly when the loading force reached its maximum value. The sample with a larger number of strands lasted longer in a higher tension range before breaking. According to the strain data, the elongation of the A4 group was higher than that of the A3 group.

For the results of the knitting fabrics which were obtained after the degradation test, the tendency among the four groups was similar as they were dry. The specimens in the A4/16 group maintained the best mechanical performances, whereas those in the A3/4 group were

performed the least well. The specimen for day 7 always had a lower broken loading force and a shorter strain than the specimen for day 1 in each group. This is acceptable as the alginate fabric was degraded in PBS solution. Although the mechanical performance of the knitting fabrics receded after degradation, the knitting fabrics were still had a much stronger mechanical performance than the commercial nonwoven specimens, as demonstrated in Figure S7, S8. The only exception is A3/8, where the strain after degradation was higher than that of the dry sample. This was because the loading force between the fibers was caused by friction in the low-density nonwoven structures. The friction between the fibers was far smaller than the loading force in the knitting fabrics. Considering the mechanical performance of four groups' fabrics were significantly different for either loading force for dry samples or after degradation, the significance was presented for comparing same group of dry and after degraded samples. Generally speaking, the strength of the knitting wound dressing was one of the advantages over reported wound dressing materials.

4.3.2.3 PBS storage and absorbency

The knitting fabric reported by this work showed good PSB absorbency. As Figure 7a, b illustrates, PBS solution was absorbed by the knitting fibers within 1/30 second that recorded by Krüss Optronic DSA100, Germany (Fig. 4.11, 4.12). The alginate fibers in the fabric swelled and filled the gaps among the knitting loops. With the continuous absorption of PBS, the dry alginate fibers experienced full gelation and became satiny in the end [7].

Water storage ability, which is an important property for a wound dressing to absorb exudate or blood, describes how much water this knitted structure could hold. The water storage ability

of the sample was characterized by a weight increase; see equation (2). Figure 7b sets out the PBS storage ability for each of the sample groups. Alginate is a type of hydrophilic material. The A3/4 group had the greatest PBS solution storage ability (502%), whereas the A3/8 group had the worst aqueous storage (383%). When the sample was immersed into a PBS solution, the large amount of sodium ions contained in the PBS solution were immediately exchanged with calcium alginate on the yarn surface of the sample. With the increase in the number of calcium ions lost to the solution, the content of calcium ions in the sample gradually decreased and the specimen weight was lost in the sample. As this chemical reaction began instantaneously, calcium alginate was replaced with sodium alginate in a short time. By comparing the A3/4 group with the A3/8 group and the A4/8 group with the A4/16 group, it can be concluded that, for the same yarn, the sample with fewer strands participating in the knitting processing had better water storage ability. This was because the parameters set by the machine were the same and the sample size was the same for the knitting samples. Concerning the same fabric size, the A3/8 group and the A4/16 samples used twice as many yarns as the A3/4 group and the A4/8 group. Therefore, the space inside the sample was also larger than that of the A3/8 group and the A4/16 group. When sodium alginate absorbed water, it swelled, and the swelled yarn occupied the interior spaces of the sample. As the samples for groups A3/8 and A4/16 sample had more yarns and less interior spaces, so their water storage capacity was not as good as the samples with fewer yarns. Comparing the samples knitted from the same strands of different yarns, the water storage performance of the A4/8 group was better than that of the A3/8 group. The A4/8 group samples were made from finer yarns, and the same area of samples weighed less that for the A3/8 group samples. For the typical commercial nonwoven structured

wound dressing, the void-age inside the fiber was relatively high. The nonwoven structure had a strong water-locking ability, due to its intricate fiber distribution and layer-by-layer network.

Water absorption was obtained according to formula (3). Groups A3/4, A3/8, A4/8 and A4/16 had a 53%, 70%, 52% and 50% PBS absorbency, respectively. Figure 7e indicates that the two A3 groups had better absorbency than the two A4 groups. Accordingly, the porosity of the fiber prepared by 21G needles was higher than that of the fiber prepared by 25G needles. High porosity means there was more volume inside the fiber for water molecules to enter.

4.3.3 *In vitro* evaluation of the wound dressing

4.3.3.1 Degradation weight changes

Figure 7a, c-d shows the wet weight of the degraded sample, where the water contained in the sample was among the knitting structures rather than that stored inside the fiber. From the data point of view, the results in Fig. 4.7c for the A3/4 and A4/8 groups are similar, with the weight increase around 800% at day 1 degradation. The results for the A3/8 and A4/16 sample groups were close, at 390% and 340%, respectively. The day 7 results were generally slightly lower than those from the day 1, but the trends were similar. The weight of the four groups of samples increased by 670%, 390%, 570% and 250%, respectively.

Weight loss was always used to characterize the degradation of sodium alginate and the dry weight of the samples before and after the degradation experiment was measured at days 1, 7 and 14. The results of the sample weight loss are shown in Figure 7d. From the day 1 results, the A3/4 and A4/8 groups showed had the highest weight loss, reaching 50%, followed by the A3/4 group with 47%. The sample weight loss of the A4/16 group was the lowest (46%).

Amongst the day 7 results, the sample weight loss of the A3/4 group was the highest (56%), although the other three groups had similar results (55%). In the 14-day group, the weight loss of the A3 (21G) sample was lower than that of the A4 (25G) sample. The four groups' results did not experience a significant difference on the same day. This is because the reason for the weight loss of the sample in the degradation test was the loss of calcium ions. The sodium ions in the PBS solution replaced the calcium ions in the insoluble calcium alginate within the solution. The generated sodium alginate was colloidal in the solution after water absorption, and the molecular structure of alginate acid was not damaged. Thus, when the sample was removed from the solution and dried, it was able to retain its general shape.

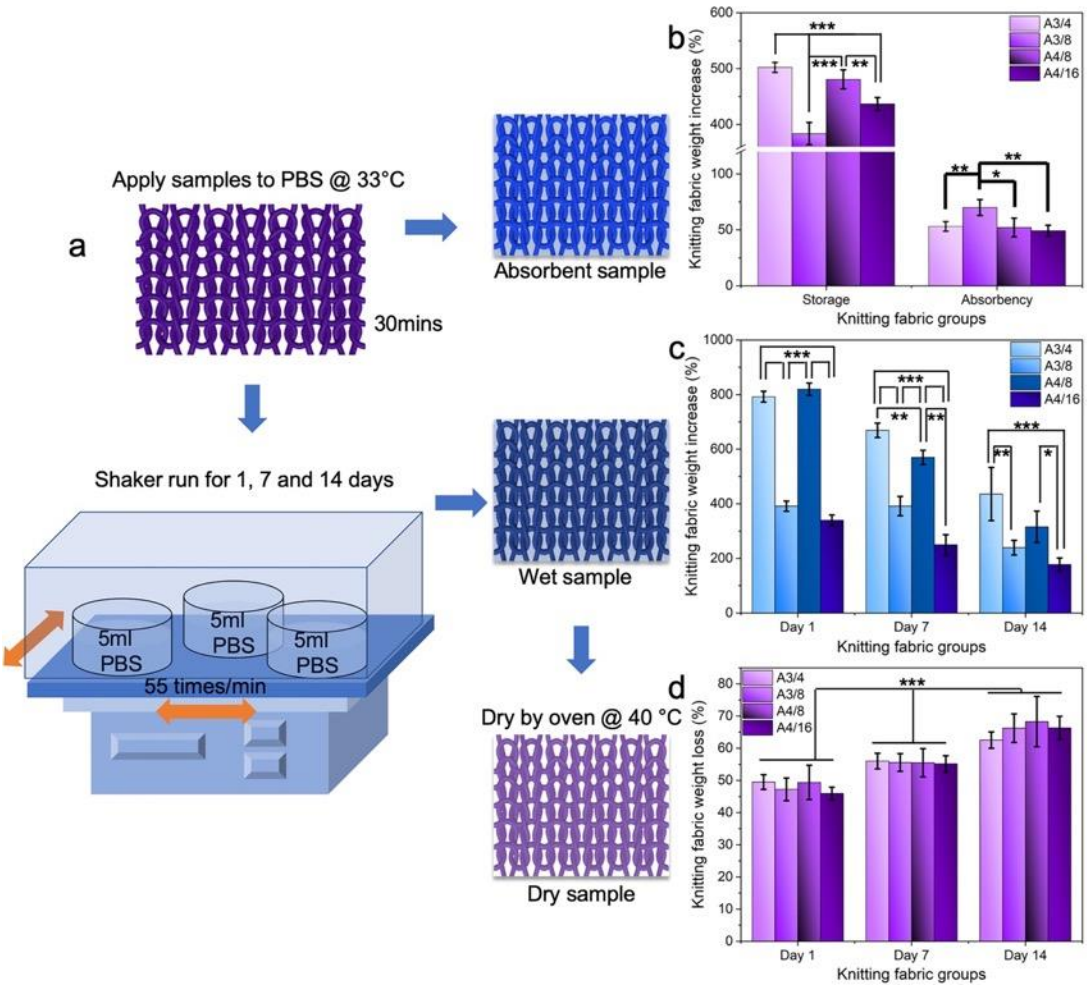

Fig. 4.7 Knitting fabric in vitro degradation behavior: (a) The diagram of degradation

performances. (b) Knitting fabric PBS storage and absorbency: pristine samples applied into 5ml PBS for 30 min. The weight increase of samples storage includes both the absorbance of PBS within the fibers and the PBS uptake due to capillary forces within the knitting structure. The absorbency is the PBS that has been absorbed into the fiber as the liquid was removed by tissue paper. (c) The wet sample weight increase changes, which means the PBS storage of the degraded knitting fabric during the degradation for day 1, 7 and 14. (d) The dry sample weight loss changes, which means the degraded alginate volume for day 1, 7 and 14.

4.3.3.2 Cell culture

Biocompatibility is one of the most important factors for alginate knitting wound dressing. In Figure 8b, the results of the cell viability study reveal that all four groups of knitting samples showed no cytotoxicity at either day 1, 4 or 7 when in contact with NIH 3T3 cell lines. The specimens of the A3 groups had slightly better cell viability in days 1 and 4. The A3/4 had a significance with A4/16. But there was no significant difference with the A4 groups. The blank control group had significantly ($p < 0.001$) better viability than all four sample groups. This finding could be explained by the fact that the knitting fabric covered the wells of the plates and stopped cell growth. By observing cell morphology via a light microscope in Fig. 8c, the cell nuclei and actin network were stained by DAPI/ Phalloidin. It was found that the cells were more starched in samples with fewer strands. It was possible that more interior spaces among the fibers could have allowed the cells to grow better. The mechanisms discussed in section 3.1 became functional when the dressing contacted the wound. Sodium ions on the wound exudated and were exchanged with calcium ions in the dressing, causing the calcium alginate to gradually convert to sodium alginate [42]. During this process, large quantities of sodium ions entered the fabric, and water was absorbed by the sodium alginate because of its saline absorbency.

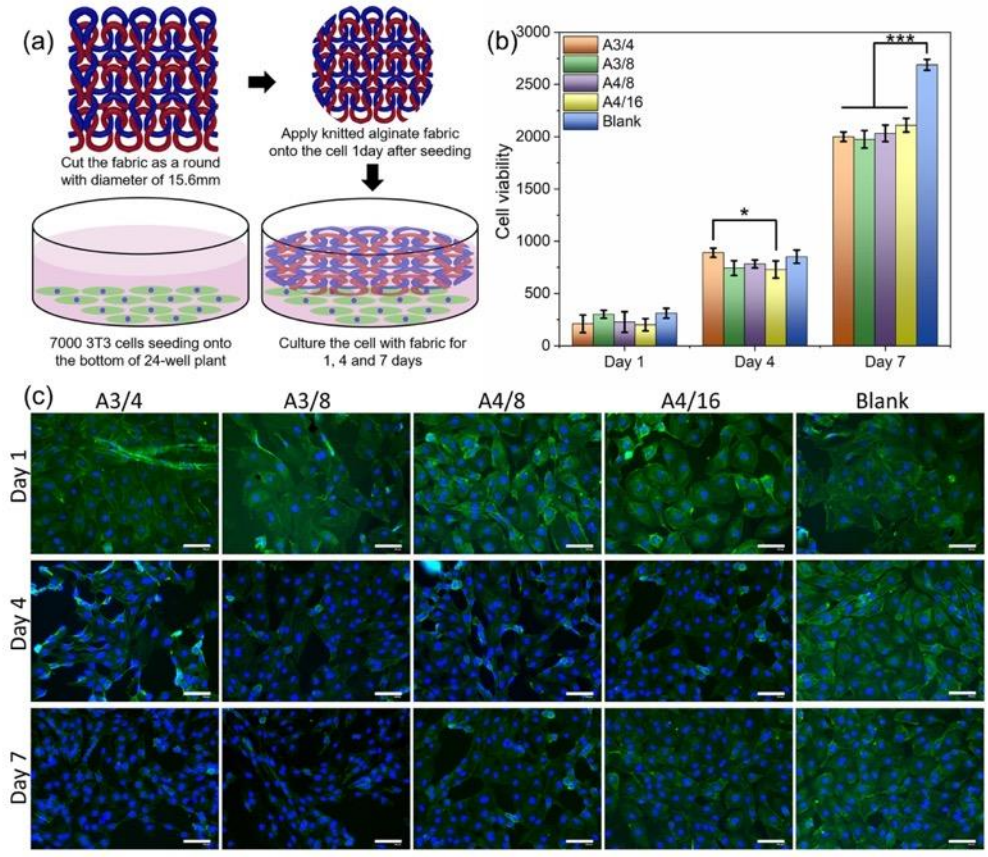

Fig. 4.8 The diagram for NIH 3T3 cell culture protocol (a); cell viability gotten by Alamar blue assay with n = 5 (b), and cell morphology, which was stained by DAPI (blue) / Phalloidin (green), for the four groups of knitting samples and the blank (without dressing materials) control group at days 1, 4, and 7; with n = 5, all bars = 100 μm.

4.4 Conclusion

In brief summary, alginate fibers with high strength and high breaking strain were spun by using a novel wheel spinning technique, then further knitted towards wound dressing material. This kind of knitted wound-care materials showed good mechanical performance, high PBS absorbency, sustained degradation rate and low cell cytotoxicity. Benefiting from a longer breaking strain and higher strength for the knitted structure, compared to a nonwoven structure, this material could offer better comfort to wounded individuals. This relatively tridimensional knitted structure, which limits the extent of the dressing-wound interface, could reduce the

number of calcium ions and accelerate tissue regeneration. Among the four groups of specimens, A4/8, with thinner fiber and a suitable number of strands, displayed better overall performance than the other groups in terms of mechanical property, PBS storage and absorbency, and degradation rate, which could be considered as an optimized material for wound-care.

Declaration of competing interest

None.

CRediT authorship contribution statement

Zhongda Chen and **Jun Song** contributed equally to this work.

Zhongda Chen: Conceptualization, Methodology, Investigation, Data curation and Writing - original draft.

Jun Song: Methodology, Visualization, Investigation and Writing - review & editing.

Yumin Xia: Methodology, Investigation.

Yuwei Jiang: Methodology, Investigation, Data curation.

Luis Larrea Murillo: Methodology, Investigation.

Olga Tsigkou: Supervision, Methodology, Investigation.

Tao Wang: Methodology.

Yi Li: Project administration, Conceptualization, Supervision, Data curation, Writing - review & editing.

Acknowledgments

The authors would like to express thanks to the support of the Electron Microscopy Center and

XRD suite in The University of Manchester.

References

[1] R.S. Ambekar, B. Kandasubramanian, Advancements in nanofibers for wound dressing: A review, Eur. Polym. J. 117 (2019) 304–336. https://doi.org/10.1016/j.eurpolymj.2019.05.020.

[2] D.J. Leaper, Traumatic and surgical wounds, BMJ. 332 (2006) 532–535. https://doi.org/10.1136/bmj.332.7540.532.

[3] G. Dabiri, E. Damstetter, T. Phillips, Choosing a Wound Dressing Based on Common Wound Characteristics, Adv. Wound Care. 5 (2016) 32–41. https://doi.org/10.1089/wound.2014.0586.

[4] Q. Pang, X. Zheng, Y. Luo, L. Ma, C. Gao, A photo-cleavable polyprodrug-loaded wound dressing with UV-responsive antibacterial property, J. Mater. Chem. B. 5 (2017) 8975–8982. https://doi.org/10.1039/C7TB01696D.

[5] M. Puthia, M. Butrym, J. Petrlova, A.-C. Strömdahl, M.Å. Andersson, S. Kjellström, A. Schmidtchen, A dual-action peptide-containing hydrogel targets wound infection and inflammation, Sci. Transl. Med. 12 (2020) eaax6601. https://doi.org/10.1126/scitranslmed.aax6601.

[6] J. Zhu, D. Tang, Z. Lu, Z. Xin, J. Song, J. Meng, J.R. Lu, Z. Li, J. Li, Ultrafast bone-like apatite formation on highly porous poly(l-lactic acid)-hydroxyapatite fibres, Mater. Sci. Eng. C. 116 (2020) 111168. https://doi.org/10.1016/j.msec.2020.111168.

[7] Y. Liu, C. Shao, Y. Wang, L. Sun, Y. Zhao, Bio-Inspired Self-Adhesive Bright Non-iridescent Graphene Pigments, Matter. 1 (2019) 1581–1591. https://doi.org/10.1016/j.matt.2019.08.018.

[8] L. Liu, L. Jiang, G.K. Xu, C. Ma, X.G. Yang, J.M. Yao, Potential of alginate fibers incorporated with drug-loaded nanocapsules as drug delivery systems, J. Mater. Chem. B. 2 (2014) 7596–7604. https://doi.org/10.1039/C4TB01392A.

[9] Y. Xi, J. Ge, M. Wang, M. Chen, W. Niu, W. Cheng, Y. Xue, C. Lin, B. Lei, Bioactive Anti-inflammatory, Antibacterial, Antioxidative Silicon-Based Nanofibrous Dressing Enables Cutaneous Tumor Photothermo-Chemo Therapy and Infection-Induced Wound Healing, ACS Nano. 14 (2020) 2904–2916. https://doi.org/10.1021/acsnano.9b07173.

[10] B. Qiao, Q. Pang, P. Yuan, Y. Luo, L. Ma, Smart wound dressing for infection monitoring and NIR-triggered antibacterial treatment, Biomater. Sci. 8 (2020) 1649–1657. https://doi.org/10.1039/C9BM02060H.

[11] T. Chen, Y. Chen, H.U. Rehman, Z. Chen, Z. Yang, M. Wang, H. Li, H. Liu, Ultratough, Self-Healing, and Tissue-Adhesive Hydrogel for Wound Dressing, ACS Appl. Mater. Interfaces. 10 (2018) 33523–33531. https://doi.org/10.1021/acsami.8b10064.

[12] Y. Yu, J. Guo, L. Sun, X. Zhang, Y. Zhao, Microfluidic Generation of Microsprings with Ionic Liquid Encapsulation for Flexible Electronics, Research. 2019 (2019) 1–9. https://doi.org/10.34133/2019/6906275.

[13] L. Shang, Y. Yu, Y. Liu, Z. Chen, T. Kong, Y. Zhao, Spinning and Applications of Bioinspired Fiber Systems, ACS Nano. 13 (2019) 2749–2772.

https://doi.org/10.1021/acsnano.8b09651.

[14] A. Watthanaphanit, P. Supaphol, T. Furuike, S. Tokura, H. Tamura, R. Rujiravanit, Novel Chitosan-Spotted Alginate Fibers from Wet-Spinning of Alginate Solutions Containing Emulsified Chitosan−Citrate Complex and their Characterization, Biomacromolecules. 10 (2009) 320–327. https://doi.org/10.1021/bm801043d.

[15] D. Puppi, F. Chiellini, Wet-spinning of biomedical polymers: from single-fibre production to additive manufacturing of three-dimensional scaffolds, Polym. Int. 66 (2017) 1690–1696. https://doi.org/10.1002/pi.5332.

[16] Y. Liu, J.-C. Zhao, C.-J. Zhang, Y. Guo, L. Cui, P. Zhu, D.-Y. Wang, Bio-based nickel alginate and copper alginate films with excellent flame retardancy: preparation, flammability and thermal degradation behavior, RSC Adv. 5 (2015) 64125–64137. https://doi.org/10.1039/C5RA11048C.

[17] Y. Yu, J. Guo, B. Ma, D. Zhang, Y. Zhao, Liquid metal-integrated ultra-elastic conductive microfibers from microfluidics for wearable electronics, Sci. Bull. 65 (2020) 1752–1759. https://doi.org/10.1016/j.scib.2020.06.002.

[18] Y. Qin, Alginate fibres: an overview of the production processes and applications in wound management, Polym. Int. 57 (2008) 171–180. https://doi.org/10.1002/pi.2296.

[19] R.P. Dumitriu, A.-M. Oprea, C. Natalia Cheaburu, M.-T. Nistor, O. Novac, C.M. Ghiciuc, L. Profire, C. Vasile, Biocompatible and biodegradable alginate/poly(N - isopropylacrylamide) hydrogels for sustained theophylline release, J. Appl. Polym. Sci. 131 (2014) n/a-n/a. https://doi.org/10.1002/app.40733.

[20] Y. Jin, A. Compaan, T. Bhattacharjee, Y. Huang, Granular gel support-enabled extrusion of three-dimensional alginate and cellular structures, Biofabrication. 8 (2016) 025016. https://doi.org/10.1088/1758-5090/8/2/025016.

[21] K.Y. Lee, D.J. Mooney, Alginate: Properties and biomedical applications, Prog. Polym. Sci. 37 (2012) 106–126. https://doi.org/10.1016/j.progpolymsci.2011.06.003.

[22] Y. Yang, T. Bechtold, B. Redl, B. Caven, H. Hu, A novel silver-containing absorbent wound dressing based on spacer fabric, J. Mater. Chem. B. 5 (2017) 6786–6793. https://doi.org/10.1039/C7TB01286A.

[23] L. Wang, E. Khor, A. Wee, L.Y. Lim, Chitosan-alginate PEC membrane as a wound dressing: Assessment of incisional wound healing, J. Biomed. Mater. Res. 63 (2002) 610–618. https://doi.org/10.1002/jbm.10382.

[24] Y.-M. Xia, Z.-D. Chen, Y. Li, Mechanical Properties Tests of Wet-spun Pure Alginate Filament and Yarns, in: Text. Bioeng. Informatics Symp. Proc. 2018 - 11th Text. Bioeng. Informatics Symp. TBIS 2018, 2018: pp. 37–46.

[25] M. Liu, H. Zhang, D. Min, X. Miao, F. Li, L. Dong, J. Xing, G. Guo, X. Wang, Dual layered wound dressing with simultaneous temperature & antibacterial regulation properties, Mater. Sci. Eng. C. 94 (2019) 1077–1082. https://doi.org/10.1016/j.msec.2018.09.049.

[26] A. Chalard, P. Joseph, S. Souleille, B. Lonetti, N. Saffon-Merceron, I. Loubinoux, L. Vaysse, L. Malaquin, J. Fitremann, Wet spinning and radial self-assembly of a carbohydrate low molecular weight gelator into well organized hydrogel filaments,

Nanoscale. 11 (2019) 15043–15056. https://doi.org/10.1039/C9NR02727K.

[27] R. Madurga, G. V. Guinea, M. Elices, J. Pérez-Rigueiro, A.M. Gañán-Calvo, Straining flow spinning: Simplified model of a bioinspired process to mass produce regenerated silk fibers controllably, Eur. Polym. J. 97 (2017) 26–39. https://doi.org/10.1016/j.eurpolymj.2017.09.037.

[28] E.S. Medeiros, G.M. Glenn, A.P. Klamczynski, W.J. Orts, L.H.C. Mattoso, Solution blow spinning: A new method to produce micro- and nanofibers from polymer solutions, J. Appl. Polym. Sci. 113 (2009) 2322–2330. https://doi.org/10.1002/app.30275.

[29] J. Foroughi, G.M. Spinks, G.G. Wallace, A reactive wet spinning approach to polypyrrole fibres, J. Mater. Chem. 21 (2011) 6421. https://doi.org/10.1039/c0jm04406g.

[30] W. Mackie, S. Perez, R. Rizzo, F. Taravel, M. Vignon, Aspects of the conformation of polyguluronate in the solid state and in solution, Int. J. Biol. Macromol. 5 (1983) 329–341. https://doi.org/10.1016/0141-8130(83)90056-9.

[31] I. Fraeye, T. Duvetter, E. Doungla, A. Van Loey, M. Hendrickx, Fine-tuning the properties of pectin–calcium gels by control of pectin fine structure, gel composition and environmental conditions, Trends Food Sci. Technol. 21 (2010) 219–228. https://doi.org/10.1016/j.tifs.2010.02.001.

[32] M.B. Stewart, S.R. Gray, T. Vasiljevic, J.D. Orbell, The role of poly-M and poly-GM sequences in the metal-mediated assembly of alginate gels, Carbohydr. Polym. 112 (2014) 486–493. https://doi.org/10.1016/j.carbpol.2014.06.001.

[33] L. He, Z. Shang, H. Liu, Z. Yuan, Alginate-Based Platforms for Cancer-Targeted Drug Delivery, Biomed Res. Int. 2020 (2020) 1–17. https://doi.org/10.1155/2020/1487259.

[34] K.I. Draget, O. Gåserød, I. Aune, P.O. Andersen, B. Storbakken, B.T. Stokke, O. Smidsrød, Effects of molecular weight and elastic segment flexibility on syneresis in Ca-alginate gels, Food Hydrocoll. 15 (2001) 485–490. https://doi.org/10.1016/S0268-005X(01)00046-7.

[35] J. Zhang, C.R. Daubert, E.A. Foegeding, Fracture Analysis of Alginate Gels, J. Food Sci. 70 (2005) e425–e431. https://doi.org/10.1111/j.1365-2621.2005.tb11471.x.

[36] T.R. Cuadros, O. Skurtys, J.M. Aguilera, Mechanical properties of calcium alginate fibers produced with a microfluidic device, Carbohydr. Polym. 89 (2012) 1198–1206. https://doi.org/10.1016/j.carbpol.2012.03.094.

[37] Y. Song, L. Xu, L. Xu, L. Deng, Radiation cross-linked gelatin/sodium alginate/carboxymethylcellulose sodium hydrogel for the application as debridement glue paste, Polym. Bull. (2021). https://doi.org/10.1007/s00289-020-03525-5.

[38] W.-P. Voo, B.-B. Lee, A. Idris, A. Islam, B.-T. Tey, E.-S. Chan, Production of ultra-high concentration calcium alginate beads with prolonged dissolution profile, RSC Adv. 5 (2015) 36687–36695. https://doi.org/10.1039/C5RA03862F.

[39] L. Li, Y. Fang, R. Vreeker, I. Appelqvist, E. Mendes, Reexamining the Egg-Box Model in Calcium−Alginate Gels with X-ray Diffraction, Biomacromolecules. 8 (2007) 464–468. https://doi.org/10.1021/bm060550a.

[40] E.E. Ureña-Benavides, P.J. Brown, C.L. Kitchens, Effect of Jet Stretch and Particle Load on Cellulose Nanocrystal−Alginate Nanocomposite Fibers, Langmuir. 26 (2010) 14263–14270. https://doi.org/10.1021/la102216v.

[41] G. Szparaga, M. Brzezińska, E. Pabjańczyk-Wlazło, M. Puchalski, S. Sztajnowski, I. Krucińska, Structure–Property of Wet-Spun Alginate-Based Precursor Fibers Modified with Nanocarbons, Autex Res. J. 20 (2020) 32–42. https://doi.org/10.2478/aut-2019-0003.

[42] M. Dakir, F. El Hanbali, F. Mellouki, M. Akssira, A. Benharref, J.F. QuIlez del Moral, A.F. Barrero, Antibacterial diterpenoids from Cedrus atlantica, Nat. Prod. Res. 19 (2005) 719–722. https://doi.org/10.1080/14786410512331330675.

Supporting Information

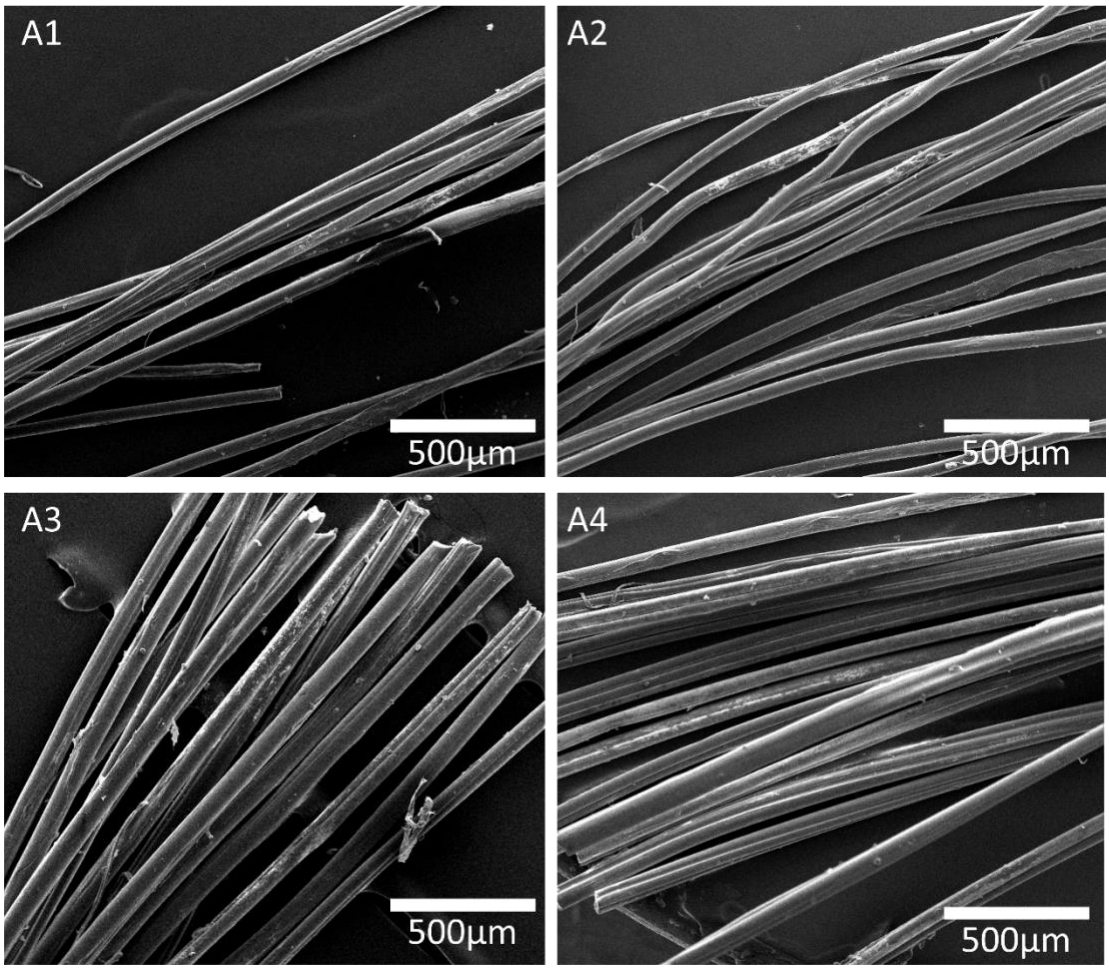

Fig. 4.9 Wheel spinning alginate fiber morphology.

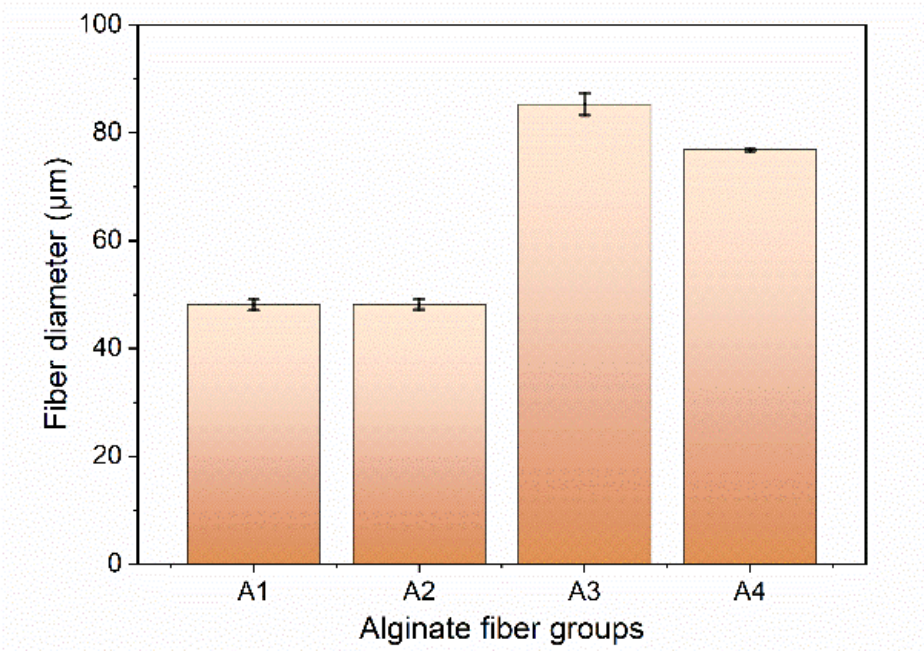

Fig. 4.10 Alginate fiber diameter with different spinning needle size and solution concentrations.

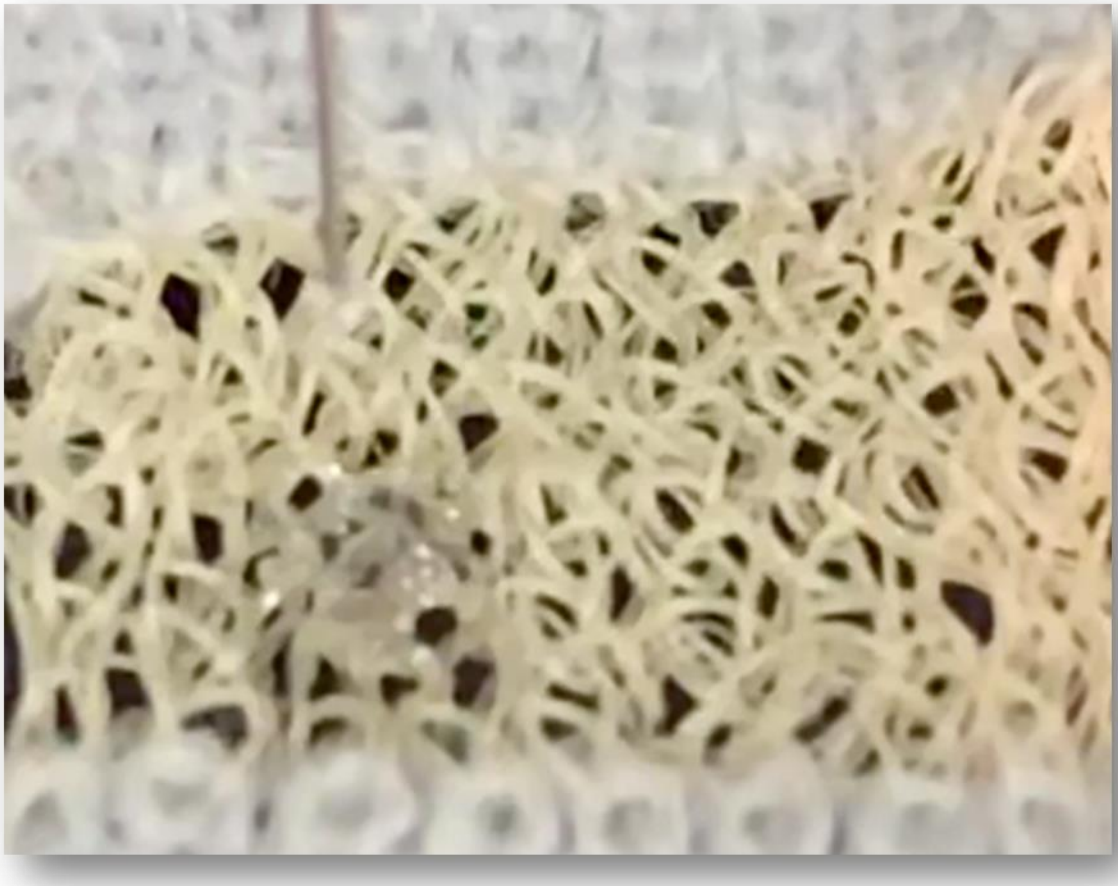

Fig. 4.11 The first frame of PBS water contact angle recorded by Krüss Optronic DSA100 attached crema.

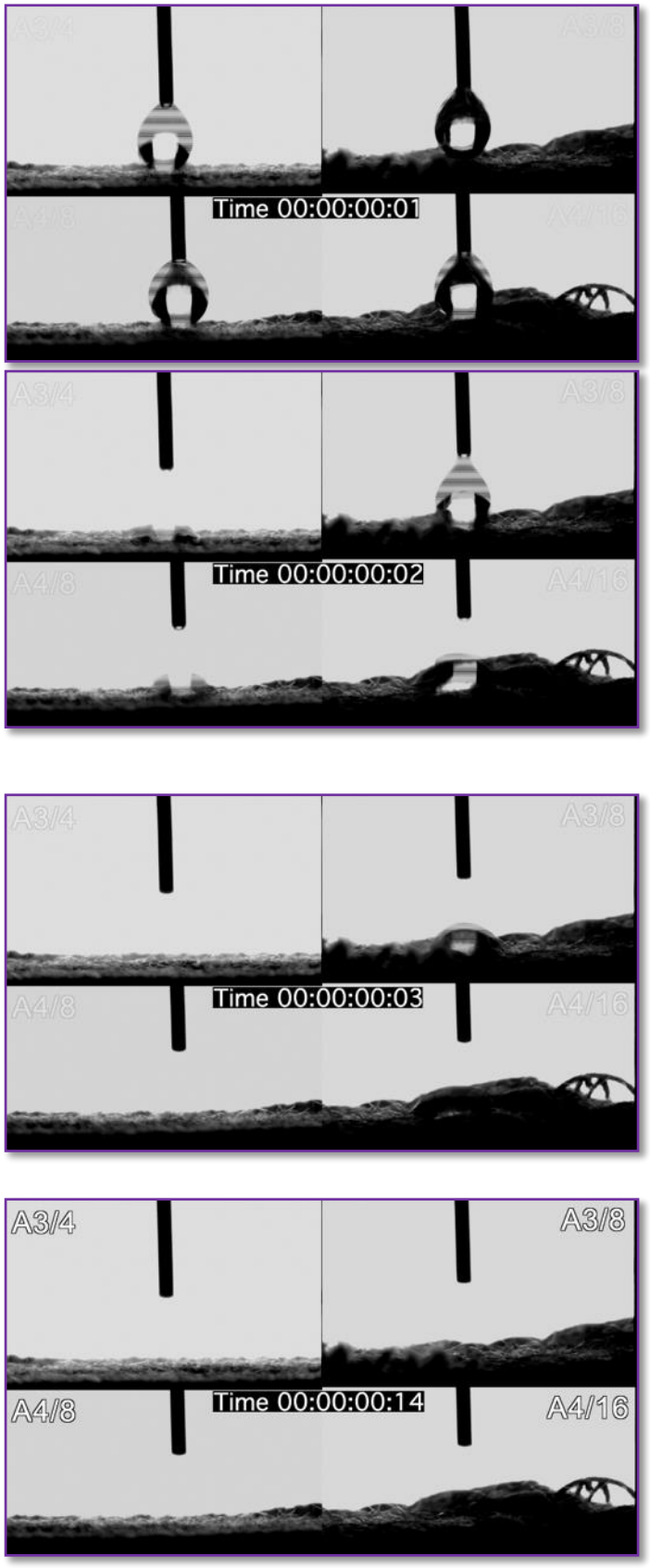

Fig. 4.12 The 1st, 2nd, 3rd, 14th frame of PBS solution contact angle recorded by Krüss Optronic DSA100 attached crema.

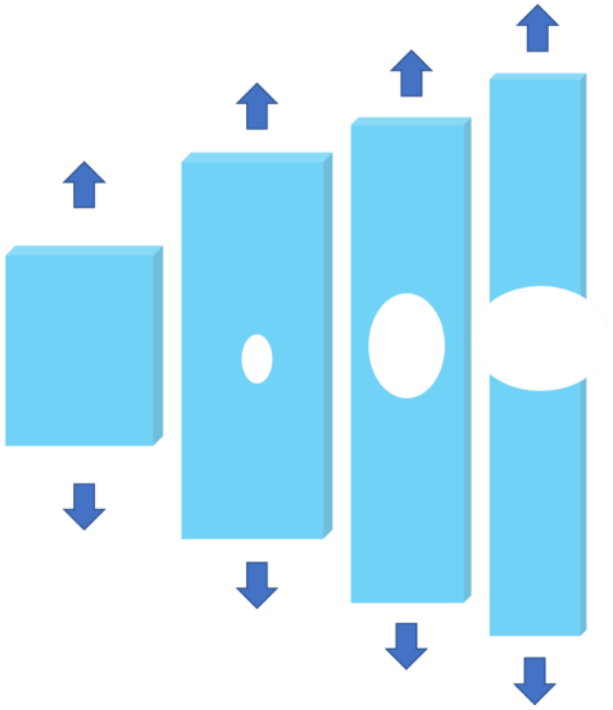

Fig. 4.13 Schematic diagram of knitted fabric breaking process. The breaking point is defined as first crack generated (second figure).

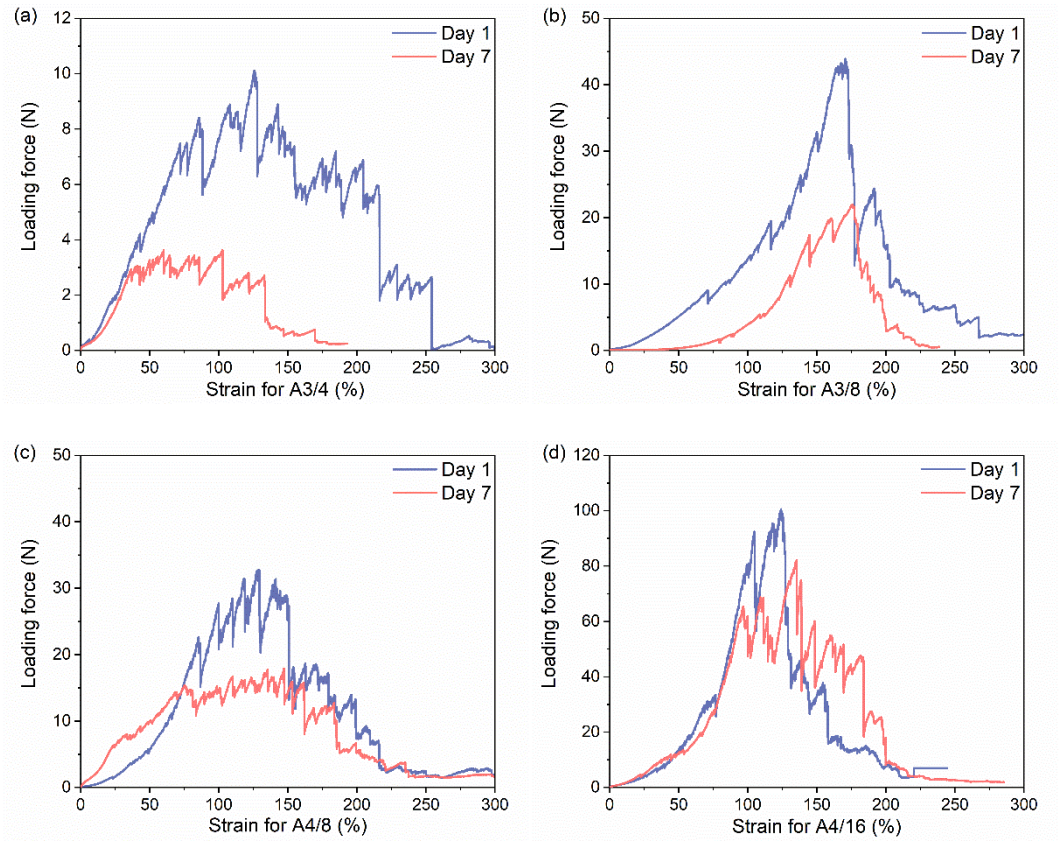

Fig. 4.14 Strain-loading curve for four groups of knitting fabrics.

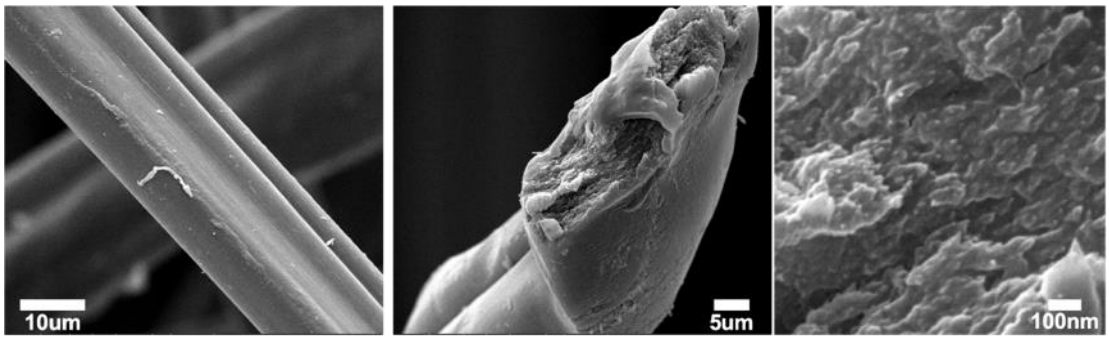

Fig. 4.15 SEM images of commercial alginate fiber.

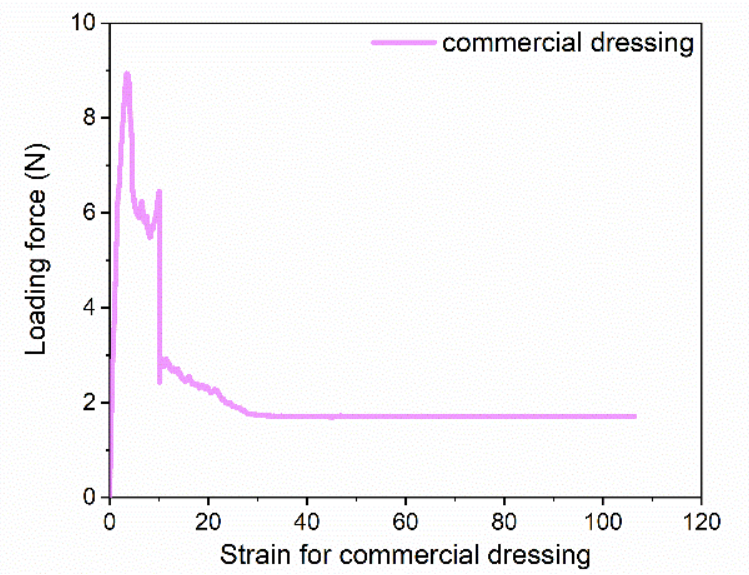

Fig. 4.16 Loading-strain curve for commercial non-woven wound dressing.

Table 4.1 The comparison of breaking stress and strain for previous studies and this work.

Wet spun tactics	Breaking stress (MPa)	Breaking strain (%)	References
Pure alginate nanocomposite fibers	80 - 100	8 - 24	(Watthanaphanit et al., 2008)
Cellulose nanocrystal / alginate fibers	2.4 - 7.5	13 - 37	(Ureña-Benavides et al., 2010)
Chitosan-polylactide / alginate fibers	14 - 20	10 - 14	(Wu et al., 2017)
Sodium alginate / cellulose nanocrystal fibers	15 - 24	8 - 18	(Liu et al., 2019)
Alginate-based multiwalled carbon nanotubes and graphene oxide modified fibers	100 - 180	3 - 8	(Szparaga et al., 2020)
Alginate-hyaluronic acid fiber	36 - 90	N/A	(Umar et al., 2021)
Pristine alginate fibers with optimized spinning parameters	**127 - 165**	**16 - 35**	**This work ★**

References for Table 4.1

[1] Liu, J., Zhang, R., Ci, M., Sui, S., & Zhu, P. (2019). Sodium alginate/cellulose nanocrystal fibers with enhanced mechanical strength prepared by wet spinning. *Journal of Engineered Fibers and Fabrics, 14,* 155892501984755. https://doi.org/10.1177/1558925019847553

[2] Szparaga, G., Brzezińska, M., Pabjańczyk-Wlazło, E., Puchalski, M., Sztajnowski, S., & Krucińska, I. (2020). Structure–Property of Wet-Spun Alginate-Based Precursor Fibers Modified with Nanocarbons. *Autex Research Journal, 20*(1), 32–42. https://doi.org/10.2478/aut-2019-0003

[3] Umar, M., Ullah, A., Nawaz, H., Areeb, T., Hashmi, M., Kharaghani, D., Kim, K. O., & Kim, I. S. (2021). Wet-spun bi-component alginate based hydrogel fibers: Development and in-vitro evaluation as a potential moist wound care dressing. *International Journal of Biological Macromolecules*, *168*, 601–610. https://doi.org/10.1016/j.ijbiomac.2020.12.088

[4] Ureña-Benavides, E. E., Brown, P. J., & Kitchens, C. L. (2010). Effect of Jet Stretch and Particle Load on Cellulose Nanocrystal−Alginate Nanocomposite Fibers. *Langmuir*, *26*(17), 14263–14270. https://doi.org/10.1021/la102216v

[5] Watthanaphanit, A., Supaphol, P., Tamura, H., Tokura, S., & Rujiravanit, R. (2008). Fabrication, structure, and properties of chitin whisker-reinforced alginate nanocomposite fibers. *Journal of Applied Polymer Science*, *110*(2), 890–899. https://doi.org/10.1002/app.28634

[6] Wu, H., Liu, J., Fang, Q., Xiao, B., & Wan, Y. (2017). Establishment of nerve growth factor gradients on aligned chitosan-polylactide /alginate fibers for neural tissue engineering applications. *Colloids and Surfaces B: Biointerfaces*, *160*, 598–609. https://doi.org/10.1016/j.colsurfb.2017.10.017

Chapter 5 Controllable release of vascular endothelial growth factor (VEGF) by a novel wheel spinning alginate/ silk fibroin fibre for wound healing

This chapter focuses on the fourth objective. The research has been completed and published at Materials & Design.

Title: Controllable release of vascular endothelial growth factor (VEGF) by a novel wheel spinning alginate/ silk fibroin fibre for wound healing

Authors: Jun Song [1], **Zhongda Chen [1]**, Zekun Liu, Yangpeiqi Yi, Olga Tsigkou, Jiashen Li, Yi Li

1 These authors contributed equally to this work.

Journal: Published on Materials & Design

DOI: https://doi.org/10.1016/j.matdes.2021.110231

My contributions: I have prepared alginate/ silk fibroin fibre via wheel spinning machine, designed all the experiments, prepared the fibrous mat enclosed VEGF, tested the release and degradation behaviour of the fibre. I also prepared the tables, the figures and the major section of manuscript.

Co-author contributions: Jun Song did the FTIR and XRD experiments, prepared the regenerative silk fibroin, and supported the presentation of data and the journal article. Mr. Zekun Liu and Mr. Yangpeiqi Yi gave the suggestion of fibre characterization. Dr. Olga

Tsigkou supported the design of VEGF study. Dr. Jiashen Li reviewed the manuscript. Prof. Yi Li supervised the whole project in this section, and reviewed the manuscript.

Highlights:

- Wheel spinning technique was used to produce wet spun alginate composite fibers.
- Alginate/ silk fibroin morphologies and concentrations control vascular endothelial growth factor release.
- The design of experimental factors and interactions address release mechanisms.
- Non-linear fitting was introduced to describe vascular endothelial growth factor release behavior.

Abstract

The acute wound healing process requires a quick and short-stage vascular endothelial growth factor (VEGF) supply, especially, in the early-stage of injury. To date, research has rarely met the demand for controlled VEGF quick release. Herein, a novel wheel spinning technique was introduced to fabricate alginate (Alg)/ silk fibroin (SF) composite fiber for loading VEGF and achieving controllable release. In turn, it was demonstrated that the parameter of wheel spinning and Alg/SF material morphological combination significantly influence VEGF release behavior and fiber degradation speed, which could be controlled by adjusting spinning solution concentration and modifying SF morphology. The loading concentration and SF structural features interacted with each other to affect the VEGF release behavior, indicating that growth factors such as VEGF could be released in a controllable fashion. It could therefore be developed as a novel approach to control the wound healing process.

Graphic Abstract

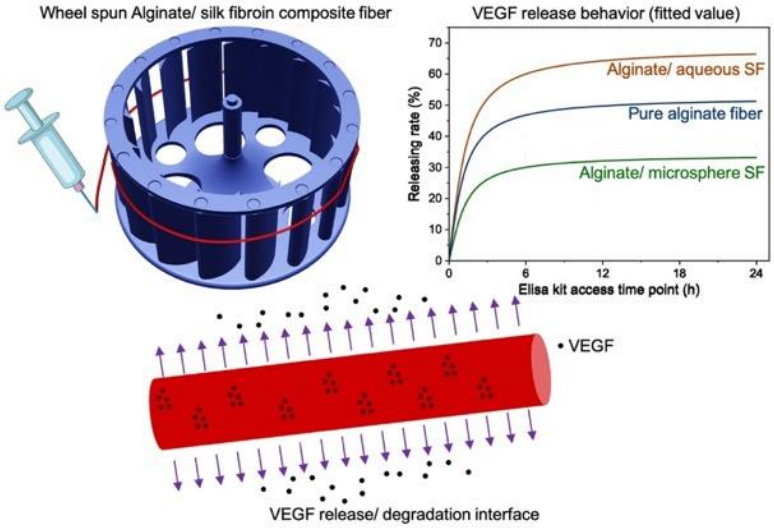

Key words: Composite fiber, wet spinning, alginate, silk fibroin, growth factor, design of experiment

5.1 Introduction

Human skin wound healing, especially for acute wound, is a phased process involving the contribution of varieties of growth factors and cytokines [1,2]. After neutrophils gathered on the wound interface through blood capillaries in minutes, monocytes and lymphocytes arrived within the next few hours [3]. These cell lineages not only defended against contaminations, but were also sources of growth factors [4]. VEGF is one of the essential growth factors in the early stages of acute wound healing necessary to achieve the proliferation of capillaries in the granulation tissue, so as to accelerate the rate of reendothelialization within a few minutes or hours [5,6].

Bioactive wound dressing is one of the clinical options available during the wound healing process, including multiple functions [7,8], i.e., enhancing an anti-inflammatory environment, maintaining cell adhesion and elevating cell proliferation, and loading and releasing growth factors. Natural polysaccharides and polypeptides are mainstream biodegradable and biocompatible wound healing materials with low immune response [9]. Next-generation wound healing systems should be able to maintain therapeutic levels of growth factor on a wounded interface desirable speed and volume [10]. As one of the cutting-edge commercial wound healing systems, the nonwoven macromolecule composite dressing has a three-dimensional cross-linked porous network which can absorb up to tens of times the dry weight of water [11].

Wet spinning is a historic and generic composite fiber manufacturing technology, in which a polymer solution is pumped through tiny holes of a spinneret under pressure into a coagulation bath until it reaches a critical concentration, after which it coagulates and solidifies into fibers [12]. However, a solution of high concentration ions and high temperature have typically led to protein denaturation and growth factor deactivation [13]. Involving another natural macromolecular to optimize wet spun composite fiber is an alternative strategy [14]. Extracted from seaweeds, alginate is a biocompatible, biodegradable and renewable wound healing material approved by the United States Food and Drug Administration and its counterparts globally [15,16]. Furthermore, alginate has shown the potential to be wet spun under a low-temperature and low-concentration calcium chloride coagulation bath to maintain the bioactivity of VEGF, which promotes wound angiogenesis [17]. Either silk fibroin aqueous solution or microspheres can be mixed with alginate spinning solution [18,19]. Notably, human wound exudate contains sodium ions while calcium alginate contains calcium ions. When applying calcium alginate wound dressing onto the wound interface, the calcium ions exchange sodium ions, such that the dressing generates a gel area on the wound surface in order to provide a barrier against invading microorganisms.

In this article, we hypothesize that the wet spun Alg/SF composite fiber loaded VEGF can achieve the controlled quick release of VEGF and stable low-speed degradation for wound healing applications. We further hypothesize that silk fibroin formations and wet spinning parameters may influence physical properties, biodegradability, and the growth factor release speed of composite fibers. Therefore, three kinds of Alg or Alg/SF based composite fibers were fabricated by a novel wheel spinning technique under conditions involving a low-concentration

coagulation bath at room temperature. The mechanisms of composite fiber fabrication were introduced. The VEGF was directly loaded into the spinning solutions for the application of wound healing dressing loaded growth factors. The experimental results and DoE effects of VEGF release performances were studied in Minitab with *in vitro* evaluation evidencing our hypothesis.

5.2 Materials and methods

5.2.1 Materials

The procurement of raw *Bombyx mori* silk was from Shengzhou Xiehe Silk, Zhejiang, P. R. China. Sodium alginate (Alg) powder (W201502) and lithium bromide (LiBr) were purchased from Sigma Aldrich, USA, and used without further purification. Ammonium sulfate ($(NH_4)_2SO_4$), calcium chloride ($CaCl_2$), and sodium carbonate (Na_2CO_3) were purchased from Fisher, UK.

5.2.2 Regenerated silk fibroin solution and microsphere preparation

Silk fibroin was dissolved using lithium bromide solution [20]. Natural *Bombyx mori* silk was degummed in a boiling 0.02 M Na_2CO_3 aqueous solution. The degummed silk was dissolved by 9.3 M LiBr aqueous solution at 60℃ for 4 h. Cellulose semi-permeable membranes (molecular weight cut-off 12,000-14,000, SERVAPOR, Germany) were applied in order to dialysis subject the dissolved high-concentration silk fibroin/LiBr solution to dialysis. The regenerated silk fibroin solution at around 6.8 wt% was filtrated and centrifuged twice before further processing.

The regenerated SF microspheres were prepared via wheel spinning, which is a modified wet spinning technique. Similar to the traditional wet spinning technique, 3 wt% regenerated SF solution was ejected into an ammonium sulfate coagulation bath (25 wt%) at 25°C. Upon completion of the wheel spinning process, the SF/$(NH_4)_2SO_4$ solution was left stand for 1 h to collect SF microsphere sediments. After washing softly using deionized water for removing ammonium sulfate, the SF microspheres were consequently transferred to a refrigerator at -20°C for 24 h. It was then possible to collect the dry particulate regenerated SF after an overnight lyophilizing.

5.2.3 Alginate/silk fibroin fiber fabrication

The designed wheel spinning device was used to prepare Alg and Alg/SF fibers [21]. As Figure 1b demonstrates, three kinds of Alg or Alg/SF wet spinning solution were extruded into a calcium chloride coagulation bath at a speed of 1 ml/min by means of a 30G needle. The wheel spun rotational speed was 200 rpm/min. For Alg/SF samples, the silk fibroin, which would either be regenerated microspheres or aqueous solution, was mixed with alginate solution at a certain ratio. The design of experiment for composite fibers is presented in Table 5.1.

For growth factor loading specimens, the recombinant human vascular endothelial growth factor (VEGF-165, Generon, UK) was added into Alg and Alg/SF solution before spinning (Fig. 5.1a). The concentration of growth factor added during spinning was fixed at 6.75 ng/mg for all sample groups. However, it was inevitable that growth factor would deplete during wheel spinning and further processing. Hence, the final actual loading amount was less than 6.75 ng/mg in this work. The loading efficiency is discussed in the result sections.

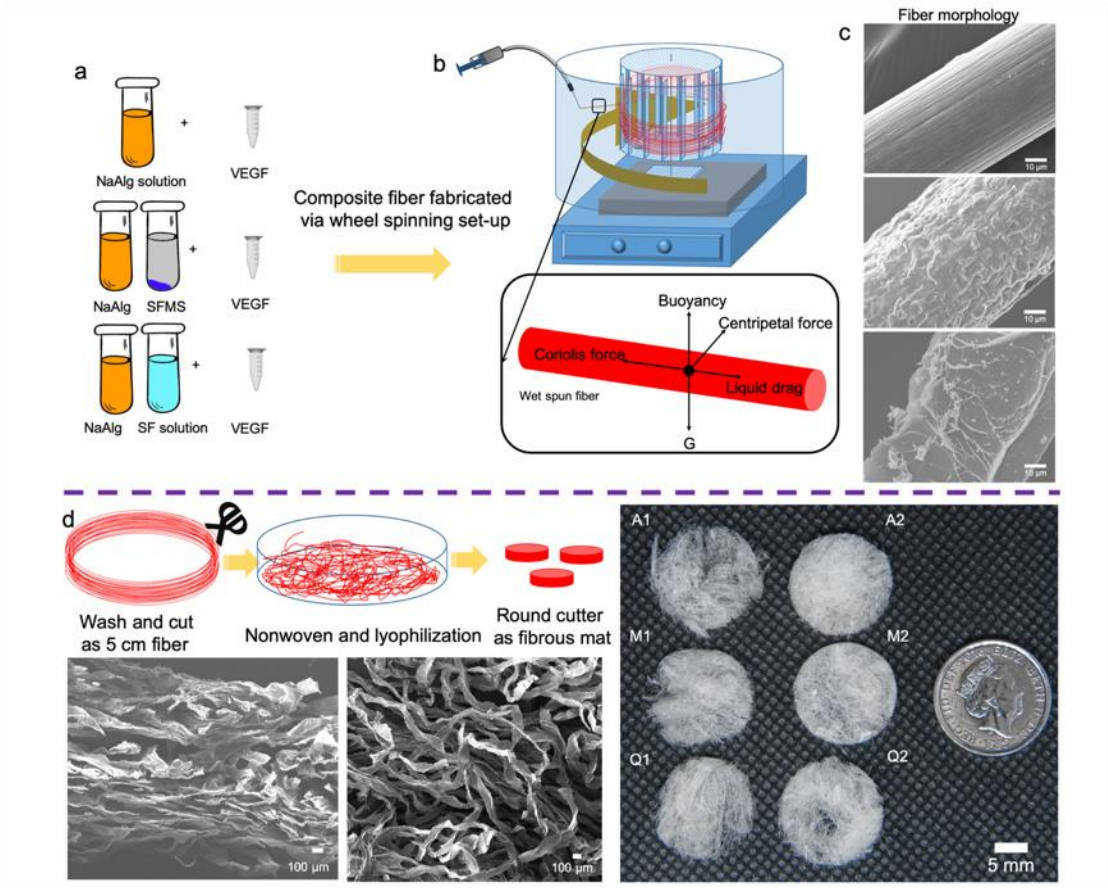

Fig. 5.1 (a, b) Wheel spinning schematic to fabricate alginate/silk fibroin fibers; (c) surface morphology of composite fibers; (d) schematic and surface morphology of alginate/silk nonwoven composite fiber.

5.2.4 Alginate/fibroin nonwoven fabrication

The acquired wheel spun fibers were washed softly and chopped into 5 cm short threads. As Table 1 shows, six sample groups were set, based on different Alg/SF concentrations and silk fibroin formations. The pure alginate samples were marked as A1 for 1 wt% Alg concentration and A2 for 3 wt% concentration. The sample groups containing microsphere or aqueous silk fibroin were marked as M1 (1 wt% Alg / microsphere SF), M2 (3 wt% Alg / microsphere SF), Q1 (1 wt% Alg / aqueous SF) and Q2 (3 wt% Alg / aqueous SF), respectively. The chopped short Alg or Alg/SF fibers were dispersed and formed as nonwoven composite mats in wet

condition. The nonwoven fibrous composite mats were lyophilized at -40℃ until thoroughly dry.

Table 5.1 Design of experiment for production of wheel spun alginate/ silk fibroin fibers.

Sample ID	Concentration $C_{Alg}+C_{SF}$		SF formation
	Alg concentration (wt%)	SF concentration (wt%)	
A1	1	0	N/A
A2	3	0	N/A
M1	0.5	0.5	Microsphere
M2	1.5	1.5	Microsphere
Q1	0.5	0.5	Aqueous
Q2	1.5	1.5	Aqueous

5.2.5 Fiber and composite characterizations

The surface morphology of Alg or Alg/SF fibers and nonwoven composite mats were observed by means of a field emission scanning electron microscopy (FE-SEM, Zeiss Ultra 55, Germany) at 1.5 kV after gold coating. Both fiber and nonwoven composite specimens were frozen sectioned in a cryostat (CM3050s, Leica Biosystem, UK) in order to observe cross-section morphology by Ultra 55.

For characterizing the difference between two kinds of Alg/SF fibers, the dried SF membrane, chopped Alg, and two kinds of Alg/SF fibers were mixed with potassium bromide powder and pressed into plates for Fourier transform infrared (FTIR) characterization using a Nicolet 5700 spectrophotometer (Thermo, USA) in transmittance mode.

X-ray diffraction (XRD) of dried pure SF membrane, chopped Alg and two kinds of Alg/SF fibers were scanned to investigate crystallization by using an X'Pert Pro's X-ray diffractometer (Panalytical, UK) with reflection mode Cu-Kα radiation operated at a voltage of 40 kV and a filament current of 40 mA, employing a scanning rate of 2°/min in a 2θ range from 5° to 50°. The mechanical properties of the chopped dry wheel spun fibers (25 mm) were performed by a universal materials tester (Instron 5566, MA USA) at a crosshead speed of 2 mm/min.

5.2.6 *In vitro* degradation

Nonwoven composite sample degradation behavior was determined by a temperature-controlled water bath shaker, set at a shaken rate of 55 times/ min and 33℃, to simulate a wound surface environment. Weight loss on day 1, day 7, and day 14 was calculated by the following Equation (1).

$$R_{\text{weight loss}} = \left(\frac{w_0 - w_t}{w_0}\right) \times 100\%, \quad (1)$$

where w_t is the weight of the nonwoven composite sample after the degradation test, and w_0 is the weight of the pristine sample before the degradation test.

Silk fibroin degradation behavior was traced via the Pierce™ Coomassie Plus (Bradford, Fisher, UK) assay kit, which can detect the concentration of SF in soaked medium and calculate the

remaining SF volume within the fiber. Thus, it was possible to obtain the SF degradation rate via the following Equation (2).

$$R_{\mathrm{SF}} = \frac{W_{SF} - C_b \times 1ml}{W_{SF}} \times 100\%, \quad (2)$$

where C_b is the concentration measured by the Bradford assay, and W_{SF} is the SF weight pristine nonwoven composite sample.

5.2.7 Measurement of VEGF release from alginate / silk fibroin composite fibers

The release of VEGF took place in a 24-well plate, with 1 ml of DMEM added into each well. Human VEGF enzyme-linked immunosorbent assay (ELISA) kits were purchased and assayed at four time points (1, 6, 18 and 24 h), according to the manufacturer's instruction (Bio-Techne, USA). To minimize the pipette operating impacts on the release of growth factor, each individual specimen was only used for collecting one set of time point data.

5.2.8 Statistics

Fiber degradation, cell work and VEGF releasing analysis were performed using IBM SPSS (version 24.000). These data were expressed in terms of mean ± standard deviation. A one-way ANOVA test was used to evaluate intergroup differences, and a p-value of <0.001 was considered statistically significant and presented as (*) in figures. The VEGF loading efficiency, VEGF release rate and Alg/SF fiber weight loss were graphed and analyzed using Minitab 17 (Minitab, LLC) and MATLAB 2018 (MathWorks, Inc) in order to reveal the relationship between the results and DoE factors [22].

5.3 Results and discussion

5.3.1 Alginate/silk fibroin fiber and composite fibers

5.3.1.1 Wheel spun alginate/silk fibroin fiber

Wet spinning is considered as a traditional chemical fiber manufacturing method, which can process regenerated polysaccharides or polypeptides, i.e., alginate or silk fibroin fibers. Some post-treatment steps such as stretching or finishing were applied to modify wet spun fibers. Instant and *in situ* treatment of wet spun fibers in a coagulation bath can also improve fiber quality as well as having been known to change scientists' and engineers' impression concerning the low-production efficiency of wet spinning technology.

Compared with synthesis polymers, the fabrication of natural polysaccharides and polypeptides are more facile, eco-friendly, economical and easy to production on a massive scale. Silk fiber has been applied as wound healing material, such as in surgical sutures several long decades [23]. Owing to the degumming treatment undertaken to remove sericin, the regenerated silk fibroin, a typical polypeptide, can avoid inflammation, which explains its use as a wound healing material [24]. Benefiting from a facile fabrication method, flexible structure, and adjustable physical and chemical properties, composite fibers can be functionalized by loading growth factor onto bioactive wound healing dressings. Wet spinning technology applies the liquid coagulation bath to solidification polymer solution. Some researchers have reported regenerated SF fibers can be prepared via wet spinning with ammonium sulfate or an organic solvent coagulation bath [25,26], which would severely break the molecular chain of fibroin and decrease its physical properties [27].

By involving a novel wheel spinning set-up, this project introduced a unique wheel spinning set up. As Figure 1b demonstrates, an Alg/SF polymer solution jet from the needle solidified and rolled on the rotator. This design reduced the size of the whole set up and elevated the efficiency of fiber collection. Figure 1b also presents the force analysis for wheel spun fiber in the $CaCl_2$ coagulation bath. Upon a solution jet of alginate or a mixture of alginate and silk fibroin being injected into the coagulation bath from the needle, the vertical buoyancy and gravity made the fiber stable in the bath. The injected solution was then quickly coagulated towards a hydrogel fiber due to the chemical reaction between alginic acid and calcium chloride. As the fiber slowly approached the center of the bath vat, the vortical rotator applied a Coriolis force and a tangential centripetal force to the fiber [28]. Coriolis and centripetal forces can lead to polymer fiber deformation. The direction of the Coriolis force was opposite to the liquid drag of fiber. The simulations on polymer solution which applied a Coriolis force were mainly focused on spinning coating fabrication [29]. A specific theorical model for wet spinning solution or similar polymer jets, when applying a Coriolis force, is neither established nor well acknowledged. Thus far, it can only be confirmed that polymer viscoelasticity is the key factor influencing fiber diameter and mechanical performances [30].

5.3.1.2 Surface morphology and mechanism of alginate/silk fibroin composite fibers

The continuous and robust surface morphology was another advantage of this wheel spinning set-up. It can be seen in Figure 1c that both Alg and Alg/SF fiber had a uniform fiber surface and diameter (Fig. 5.8). The pure alginate fiber was smooth, while two kinds of Alg/SF composite fiber revealed a wrinkled rough surface. There were also some highly oriented

grooves on the pure alginate fiber. Figure 2b demonstrates the chemical reaction between the sodium alginate spinning solution and the calcium chloride coagulation bath, which contributed to this oriented groove morphology. Specifically, when the alginate spinning solution was rapidly squeezed into the coagulation bath, the calcium ions' cross-linked alginate molecular chains went onto form lateral egg-box complex dimers (Fig. 5.9) on the spinning solution / coagulation bath interface [31]. These cross-linked alginate molecular chains were further agglomerated towards robust alginate nanospheres (Fig. 5.10) as indicated in the cross-section SEM image of alginate fiber in Fig. 5.2a [32]. In turn, the shear force from the needle of the spinning set-up led alginate nanospheres towards the oriented grooves.

In fact, most researchers in bio-materials have used lyophilized SF powder as a raw material [33]. In this work, the SF microsphere (SEMs in Fig. 5.11) was cross-linked through ammonium sulfate, then freeze-dried. However, this SF microsphere cannot be regarded in terms of typical lyophilisomes. Regenerated SF is a fibrils polypeptide, which is extremely sensitive to ions solution and facilitates conformational transition. As for ammonium sulfate, previous studies have reported the successful fabrication of a SF microporous membrane or wet spun fibers [34]. Combined with related reports, it was confirmed that a lower-concentration ion coagulation bath cannot transit SF conformation and orientate the SF molecule chains. Thus, the optimized wheel spinning set up was able to scatter the SF jet flow to microspheres. Combined with the alginate agglomerated egg-box multimers fabricated by wheel spun in the previous study [21], SF influenced the alginate aggregation when these either aqueous or microspheres SF microspheres were mixed with alginate spinning solution and wheel spun again as Fig. 5.2b shown. As an improvement of conventional chemical engineering technology, wheel spinning

set-up tries to fill the gap between macro materials and molecular level substances [35]. The SEM images in Fig. 5.2a present the cross-section of Alg/SF microsphere composite fiber. It is critical that the calcium chloride used for alginate spinning also preserved SF as a nanofibril, in other words, in a random-coil state [36]. As the cross-section SEM image of Alg/SF aqueous composite fiber in Fig. 5.2a confirms, the SF nanofibril self-assembled into nanoparticles, became attached to the alginate and spun into composite fibers.

5.3.2 Composite fiber wound healing material characterization

FTIR spectroscopy was conducted to investigate the different secondary structures of alginate and fibroin in three kinds of fiber specimens. In general, the FTIR curves of the two kinds of Alg/SF hybrid fibers were significantly different (Fig. 5.2c). The fiber fabricated by alginate and SF microspheres was more similar to pure alginate fiber, while the fiber fabricated by alginate and aqueous SF was akin to pure SF specimens. In the case of Amide I and Amide II regions of SF, previous literatures has indicated that typical characteristic peaks at ~1655 cm^{-1} and ~1540 cm^{-1} refer to the random coil conformation of peptide, while the characteristic peaks at ~1630 cm^{-1} and ~1520 cm^{-1} are characteristic indicate β-sheet conformation, respectively. The characteristic peak of Amide II was observed in fibers containing either microsphere or aqueous formation SF. However, the aqueous SF fiber remained as random coil in Alg/SF fiber, whereas the SF microsphere were subject to β-sheet conformation, resulting in a more stable state of fibroin. The Amide I adsorption peak of SF could only be observed in Alg/SF aqueous fiber. Conversely, the asymmetric band, i.e., the intense stretching vibration peak at 1600 cm^{-1}, of carboxylate anions could only be observed in pure alginate and Alg/ SF microsphere fibers. As the dotted box in the figure shows, the peaks at 1410 cm^{-1} were assigned to the symmetric

band of alginate, which could be detected in all three kinds of fibers. FTIR curves proved either microsphere SF or aqueous SF was successfully spun with alginate into fibers. The microsphere formation of SF was more stable than the aqueous formation of SF in Alg/SF fibers.

XRD for three kinds of fibers was also conducted, and the relevant patterns are introduced in Fig. 5.2d. All three fibers retained a low crystalline state. This is reasonable due to these two natural polymers not being crystallized during processing. A diffraction peak at around 13.4° could be observed in Alg or two Alg/SF fibers. This peak should be assigned to the lateral packing among alginate molecular chains. The Alg/SF microsphere specimen had a relative intensive peak at 20.7°, which was a typical diffraction peak for the Silk II state. According to the cross validation carried out using infrared spectroscopy, the demonstrated results of XRD are consistent with those of FTIR.

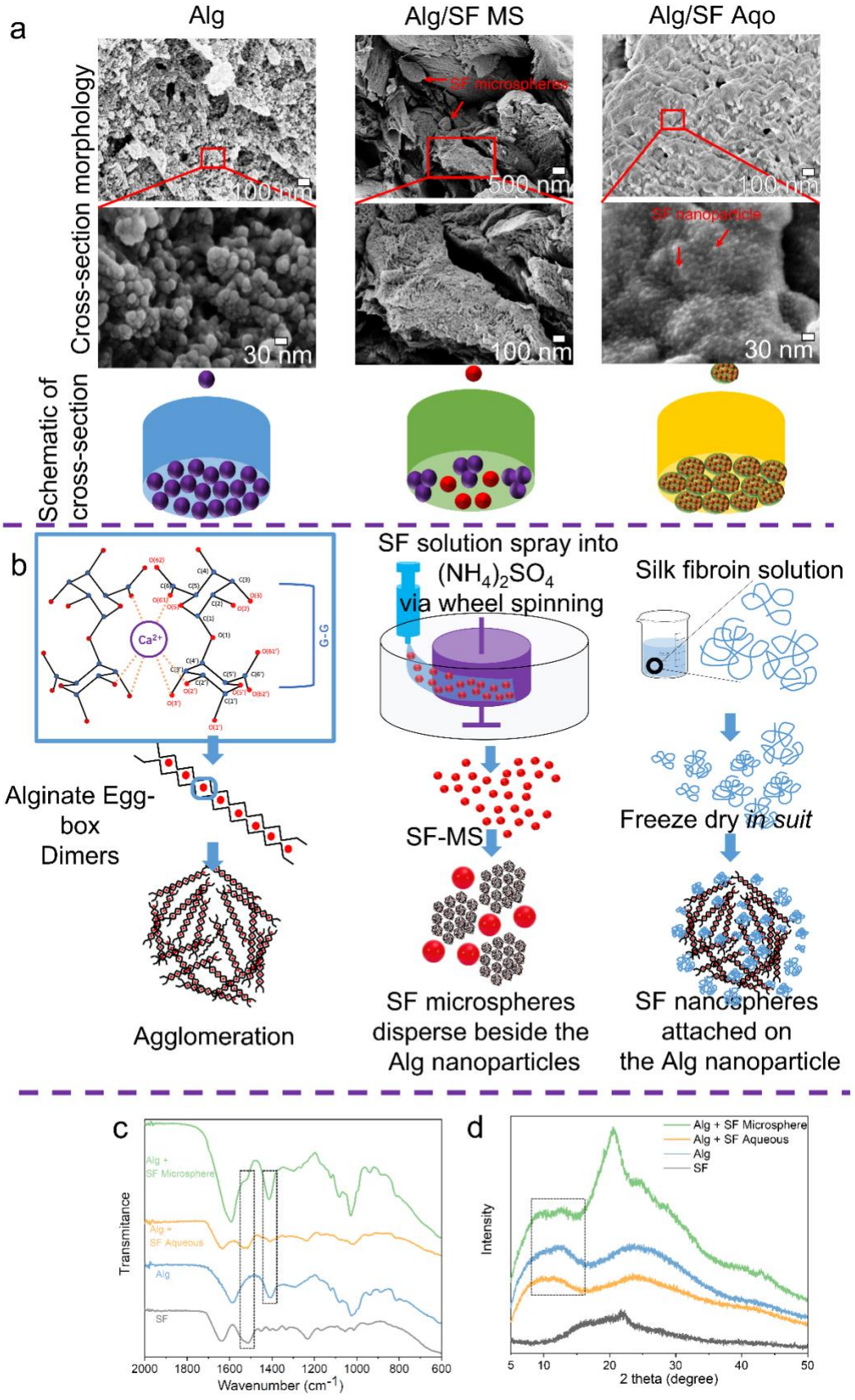

Fig. 5.2 (a) The cross-section surface morphology of three kinds of Alg/SF fibers. (b) The

alginate reacts in a calcium chloride coagulation bath to form lateral egg-box complex dimers at the spinning solution / coagulation bath interface. SF spinning solution jet flow was broken by the optimized wheel spinning set-up to microspheres. The aqueous SF was kept in a random-coil state and attached to the alginate, then spun into composite fibers. FTIR patterns (c) and XRD curves (d) of Alg/SF microsphere (green), Alg/SF aqueous (yellow), pure alginate composite fiber (blue) and pure silk fibroin microsphere (black) specimens.

5.3.3 Alginate/ silk fibroin composite fiber loaded VEGF

Traditional breathable, waterproof and topologically structured wound dressing could only meet the basic criteria of biocompatibility. In recent years, striking a balance between physical structure and bioactivity for wound healing materials has been a hot topic. Table 5.2 presents some of the parameters from previous work into different formats of alginate or silk fibroin materials which loaded VEGF onto bioengineered scaffolds. Most researchers report on growth factor loading amounts and releasing volumes at certain time points throughout the day. However, standard examination criteria have yet to be established concerning the releasing performances of growth factors. At present, there are only a few studies which critically review or present research on growth factor loading efficiency [37]. To this extent, Table 2 reviews and calculates VEGF loading efficiency and releasing speed based on data collected in the literature. Some researchers have reported relatively high loading efficiency in case of chemical conjugation [38]. However, the release rate of growth factors loaded by chemical methodology was difficult to control. Thus, it was only suitable for chronic wounds which need a slow release over a period of weeks. In this study, by controlling the degradation rate of alginate and silk fibroin, VEGF was loaded by using a physical method in order to achieve controllable quick release alongside slow degradation composite fibers. As the SEM images Fig. 5.2 demonstrated, three groups of Alg or Alg/SF fibers had different mesoscale morphology with each other due

to the wheel spinning method. These morphological differences provide the possibility to achieve the controlled release of VEGF.

Fig. 5.3 demonstrates the evaluation protocols for VEGF loading efficiency. VEGF loading efficiency was calculated by measuring the VEGF concentration that was lost in the coagulation bath using ELISA assay kits. Based on the interval plot in Figure 3b, d and consequent main effect results Fig. 5.12, there was no significant difference in VEGF loading efficiency among three kinds of composite fibers. The Alg/SF microsphere composite fiber had the worst VEGF loading rate. The higher-concentration sample usually enjoyed a slightly better loading rate than that the lower-concentration sample for the same Alg/SF composite fiber.

Table 5.2 Pervious reported VEGF releasing parameters for alginate or SF based scaffolds.

Alginate or SF based scaffolds	Time point (day)	Loading amount (ng/mg)	Loading efficiency (%)	Release ratio (%)	Release speed (%/day)	Ref
Silk fibroin core-shell electrospinning	1, 2, 4, 7, 10, 13, 16	0.28, 0.58	33-67%	7%, 11%	2.5, 7.5	[39]
Vancomycin/ Silk nanoparticle	1, 3, 7, 14, 21, 28	10	97%	14%	0.7	[40]

Silk fibroin/ calcium phosphate/ PLGA nanocomposite	1, 3, 7, 14, 28	4	65%	6%	0.8	[41]
Wheel spun Alg/SF composite fiber (★ this work)	Within 1 day	6.75	30%	9-22%	25-70	★
Injectable alginate composite hydrogel	1, 3, 5, 7, 14,	11800	N/A	51%	26	[42]
Hybrid Polycaprolactone/Alginate Scaffold	0 - 14	350	61-77%	5%	4.5	[43]
VEGF-conjugated alginate hydrogel	1, 3, 7, 14, 28	4.1	14-16%	4%, 15%	0.1	[38]
Alginate/laponite hydrogel microspheres	0, 3, 7, 14, 28	10	45%	11-16%	1.5-2.3	[44]

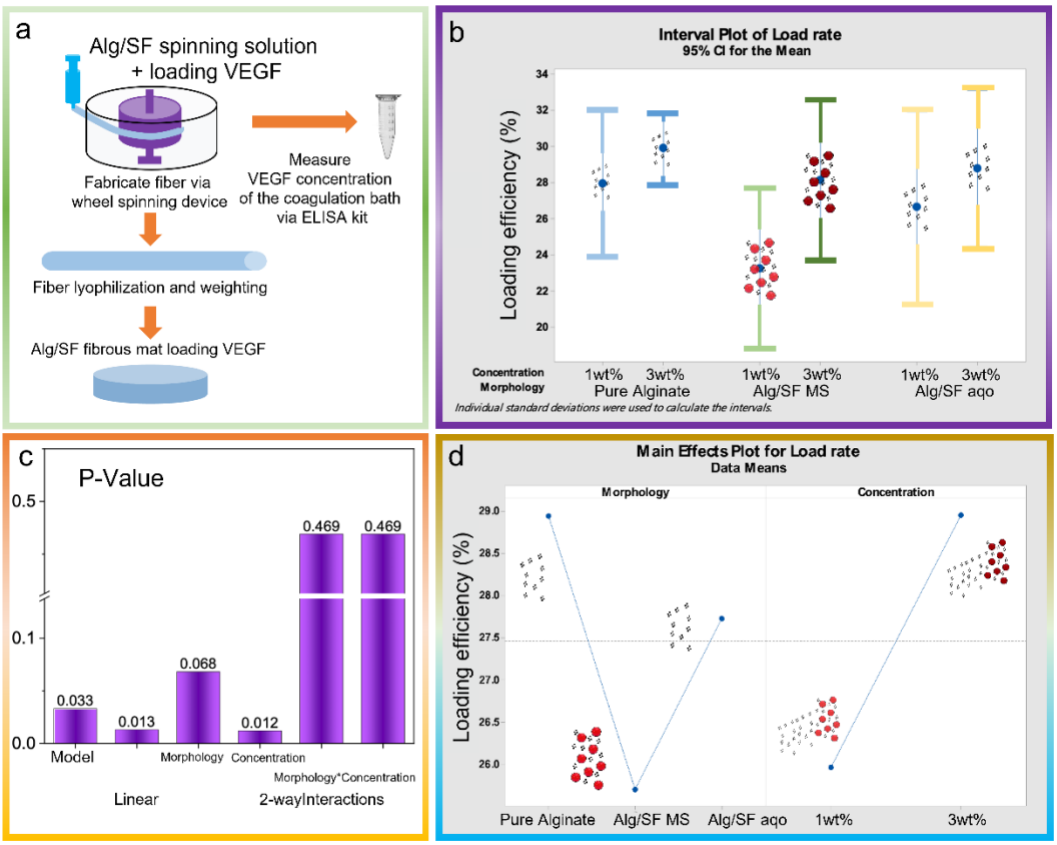

Fig. 5.3 VEGF loading efficiency was calculated by measuring VEGF concentration lost in the coagulation bath by using ELISA assay kits. (a) Measurement schematic for VEGF loading efficiency, (b) the results of loading efficiency affect via DoE parameters, main effect (c) P-Value and (d) plot of VEGF loading efficiency in Alg/SF composite fibers.

5.3.4 Controlled release of VEGF via silk fibroin inside alginate fiber

The 24-h release kinetics of VEGF loaded by Alg/SF composite fibers was measured by using ELISA assay kits at four time points, as exhibited in Figure 4. The Figure 4a demonstrated the evaluation protocols for VEGF releasing rate and speed. VEGF releasing speed could be defined as the quotient of the growth factor quantity released and time in a given period. Thanks to the calcium alginate formed during the wet spinning on fibers' surface, the Alg/SF fibers in this work can remain relatively stable in water or air environments. On the contrary, once the fiber or non-woven structure touches the human wound interface, sodium/calcium ions exchange would occur, and the release of VEGF will begin. This situation can essentially be

understood as a trigger mechanism. The physical loading method in this study followed the characteristics of an arctangent function image. Specifically, a large proportion (30%) of VEGF was released within 24 h. The VEGF release rate calculation time of this study was within one day, whereas the release tendency and release volume were similar to those of other studies, i.e., from half to one month. A large proportion of VEGF was released in the first hour, which could be defined as quick release.

Developing theoretical models for describing growth factor release mechanisms has received considerable attention in recent years [45]. A arctangent function in Equation (3) was selected for nonlinear fitting in order to conclude the potential principle in this study [46].

$$y = A \times \arctan(B \times x), \quad (3)$$

This function was highly simplified, but effective as shown in Figure 4b. The *Coefficients A* represented the VEGF final release volume and confirmed the asymptote (y = A×pi/2) in the functions graph, while the *Coefficients B* represented the initial VEGF release speed and the fractality degree in graph of functions.

Upon alginate fiber immersion into DMEM, the cross-linked calcium alginate on the fibers' surface was converted into soluble sodium alginate, while VEGF was released alongside the dissolution of composite fibers. It was also observed that the VEGF release rate and the composite fiber degradation rate were essentially consistent. Comparing the Alg/SF fibers with alginate ones, the addition of SF aqueous solution increased the release rate and reduced the degradation rate. These changes may be attributable to soluble SF in the fiber. Aqueous SF is known to improve fluidity inside the hydrogel, making it easier for VEGF to effuse from Alg/SF

aqueous composite fibers. The addition of SF reduced the relative concentration of alginate spinning solution. Thus, it was inevitable that the degradation rate would be lower than that of alginate fibers. Different from the SF aqueous, the addition of microspheres reduced both degradation speed and release rate at the same time. These changes may be due to the gaps between the interior SF microspheres and alginate, which made it difficult fo the composite fibers to disintegrate quickly after absorbing water. The alginate and SF concentration also affected the density of the fibers, as proven by the fiber diameter data in Figure S1. The alginate fiber was released quickly at a high concentration and degraded quickly, while the fiber of the Alg/SF microspheres released quickly at a low concentration and degraded quickly. Only Alg/SF aqueous fiber at a high concentration was released quickly and degraded slowly. In conclusion, the addition of two kinds of SF had positive effects on composite degradation and VEGF releasing performances.

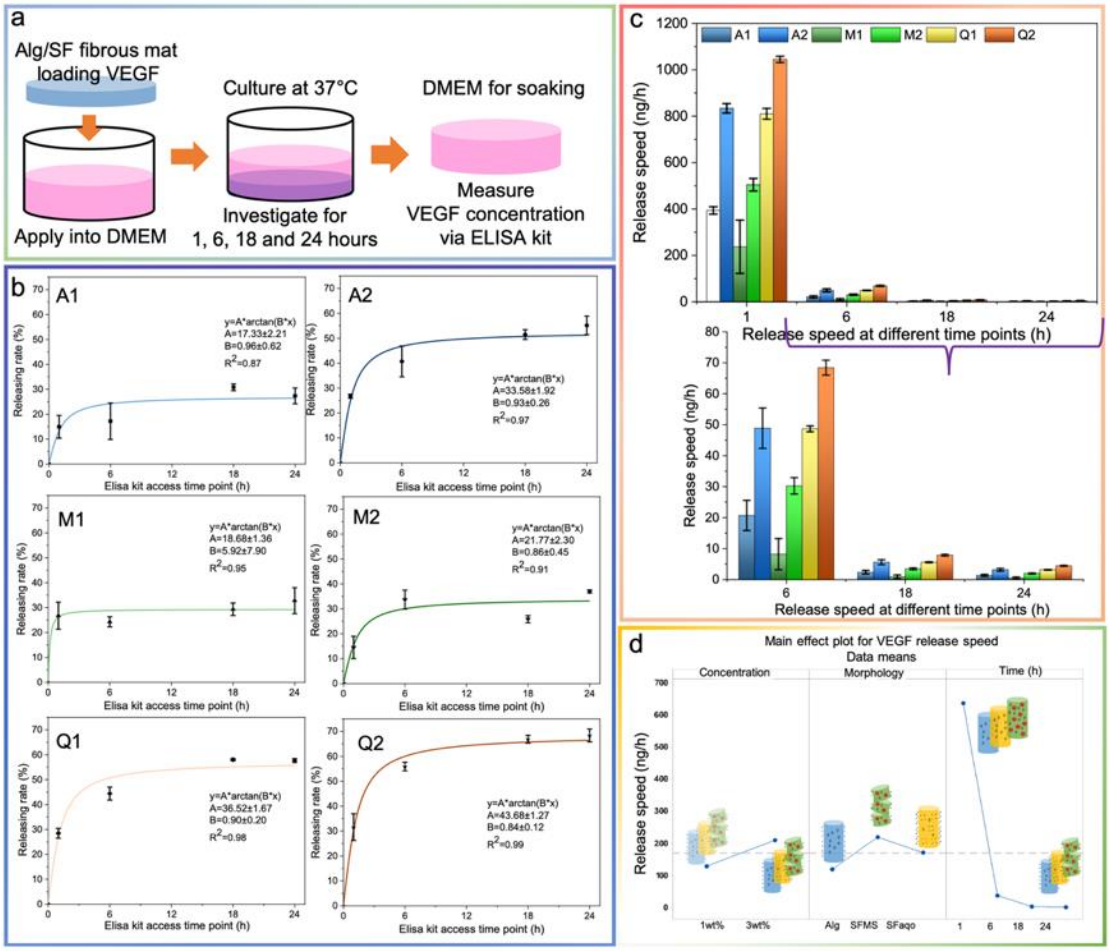

Fig. 5.4 VEGF release behavior from Alg/SF composite fiber. (a) VEGF release rate scatter diagram and non-linear fitting curves for six groups of Alg/SF composite fiber. The VEGF releasing rate was calculated by measuring VEGF concentration in composite fiber soaked in DMEM solutions using ELISA assay kits at four time points. (b) Schematic diagram and (c) release speed for evaluating VEGF release performances. The VEGF release speed was calculated by measuring the first-order derivative of non-linear fitting curves and transferred to the actual amount.

5.3.5 Effect of silk fibroin morphology and spinning solution concentration

Based on the DoE presented in Table 5.1, Alg/SF composite fiber morphology and spinning solution concentration can affect VEGF release tendency and composite fiber degradation performance. As Fig. 5.5a demonstrates, composite fiber morphology and concentration can affect weight loss significantly. Based on the evaluation of composite fiber VEGF release, it can also be confirmed that fiber morphology and concentration can affect release significantly.

The addition of SF microspheres reduced the release speed slightly, whereas the addition of aqueous SF increased the release speed sharply. Higher wheel spinning solution concentration caused a higher release rate, but the addition of SF microspheres weakened the effect. In the first hour of evaluating VEGF release, the spinning solution concentration did not affect the release too much.

Although our wound healing materials experienced slow degradation and quick VEGF release performances, it should be noted that excessively applying of VEGF, especially over a short period, causes edema or other complications [47]. Regarding the diversity and complexity of human wounds, the desired VEGF volume should be diverse too [48]. Our wound healing composite fibers can be adjusted by loading volume and comprise a mix of different kinds of fibers to ensure the quick release of necessary VEGF.

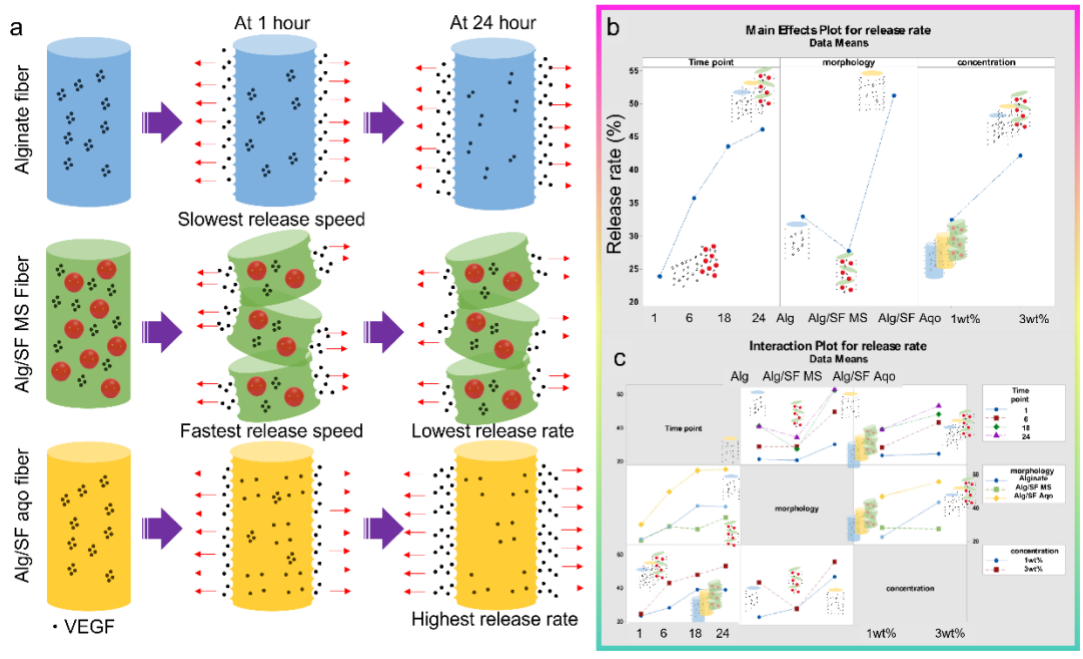

Fig. 5.5 (a) Main DoE effect plot for Alg/SF composite fiber release rate, (b) interaction effect plot.

5.3.6 *In vitro* degradation evaluation for alginate/silk fibroin composite fiber

For the purpose of evaluating *in vitro* degradation performances, the samples were incubated in DMEM solution which mimics the human interstitial fluid in order to measure the quantitative changes. The schematic diagram in Fig. 5.6a demonstrates the degradation study for Alg/SF composite fibers. The addition of either microsphere or aqueous SF reduced the level of weight loss while evaluating degradability, especially between the SF aqueous groups. The higher concentration fibers displayed a slower degradation speed, although it was faster in the first hour (Fig. 5.13). It was found that the specimens of Alg/SF microsphere groups degraded faster than those of Alg/SF aqueous groups although the SF microspheres were cross-linked and more stable than in the SF aqueous groups. This was due to the insoluble SF microspheres in the fibers acting as they disintegrate. Further, the microscale SF ingredient indeed accelerated the breakdown of composite fibers. However, after the SF microsphere brought about disintegration, the Alg/SF microsphere composite fibers experienced a slower degradation speed than the Alg/SF aqueous fibers. Comparing the degradation performances of three kinds of fibers, the pure alginate fiber quickly degraded at the beginning while the two kinds of Alg/SF hybrid fibers exhibited a relatively steady degradation performance during the 24-h-long evaluation. Furthermore, the Bradford assay was performed and the specific SF weight loss and degradation share were calculated for Alg/SF aqueous group. The vertical axis in Figure 5c represents SF degradation according to a logarithmic scale. It was obvious that the aqueous SF in composite fibers quickly degraded (500-550 μg) in the first hour of the experiment whereas alginate slowly degraded in the hours that followed.

Due to the SF and alginate are both acknowledged implantation materials with good biocompatibility [16,49], we believe the cell work to prove the basic *in vitro* cell viability is not

necessary. However, the cell adhesion results are presented in the supporting information (Figure S12 & S13) because undue cell adhesion performances should be regraded a passive characteristic for wound healing materials.

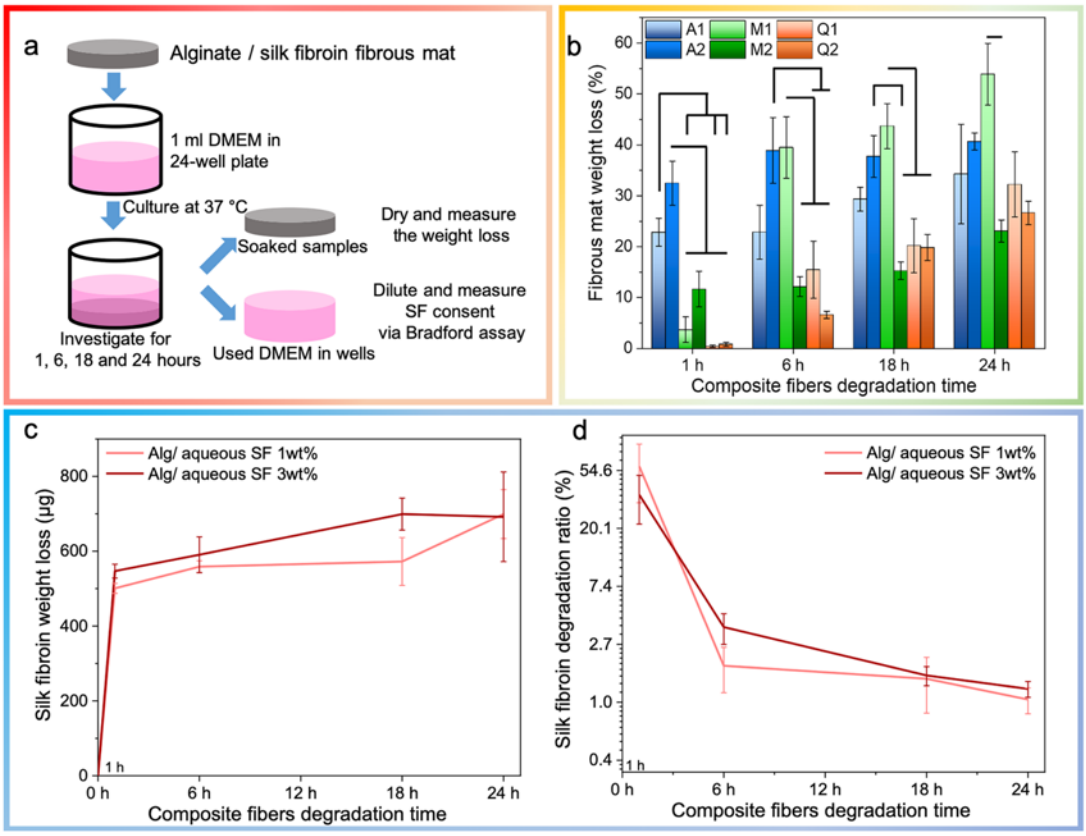

Fig. 5.6 (a) Schematic diagram and (b) weight loss results for the composite fiber biodegradability study. The weight loss among composite fibers was investigated by drying and measuring samples soaked at four time points. The DMEM used in wells was diluted SF consent measured via the Bradford assay. (c) SF weight loss and (d) degradation ratio was consequently calculated and presented.

5.3.7 How wheel spinning set-up affects physical properties of Alg/SF fibers

Based on the DoE study (Fig. 5.14-18) of Alg/SF wheel spun fibers, the wheel rotation speed does affect the mechanical properties of wheel spun fibers as Fig. 5.7 shown. The fibers' stain and stress show opposite changes with the speed of the three formulas of fibers increasing. For pure alginate fibers, the drawing rate of fibers becomes higher due to higher shear force from

the coagulation bath flow, when the rotation speed increases. As the result, the pure alginate fabricated by higher rotation speed could have a more consolidated structure which causes a lower strain. For Alg/SF wheel spun fibers, the mechanical properties are totally opposite. Thus, we assume the Alg/SF, a heterogeneous matter, would become more unconsolidated. These unconsolidated structures are beneficial to the VEGF quick release. This is the reason why the 60 rpm specimens, especially for Alg/SF groups, were selected for further VEGF loading and releasing study in this work. Two different morphologies of SF were applied to further control the VEGF releasing, degradation, mechanical behavior of Alg/SF fibers.

However, the influence of the rotation speed is significantly less important than the influence from the fiber themselves, i.e., spinning concentration and silk fibroin morphologies. Combining with the demonstrated SEM and XRD data, as well as the previously established alginate aggregation theory [21], it could be confirmed the three kinds of fibers are under low crystallinity and low orientation states. This may be due to the soft drafting effect of wheel spinning on the fiber, along with the relatively low temperature and low ions concentration. All these conditions of force, temperature, and solvent avoid the induced re-crystallization. The relatively low crystallinity and low orientation fiber is conducive to the VEGF quick release.

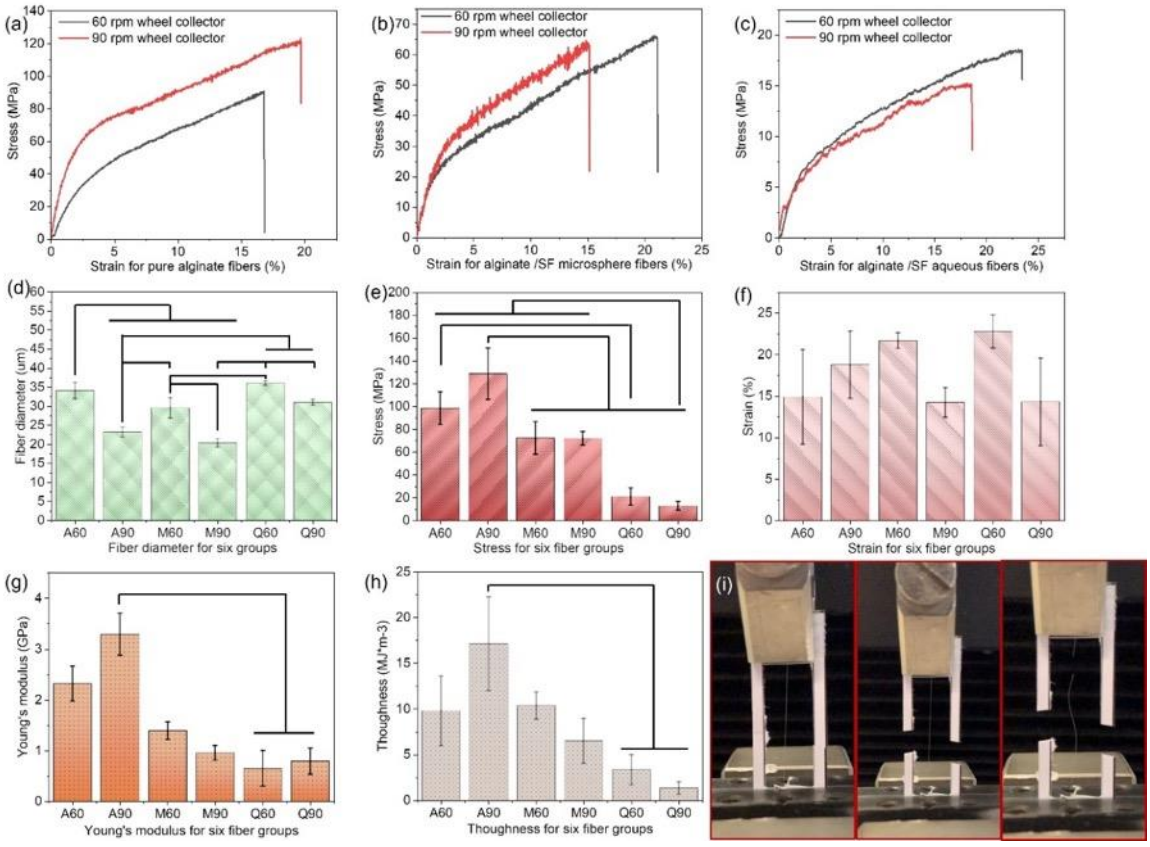

Fig. 5.7 (a-c) stress-strain curves of pure alginate or Alg/SF wheel spun fibers. (d) fiber diameter counts of pure alginate or Alg/SF wheel spun fibers. (e-h) stress, strain, Young's modulus, and toughness of pure alginate or Alg/SF wheel spun fibers. (i) the optical images of tensile test for Alg/SF fibers.

5.4 Conclusion

In summary, Alg/SF composite fibers loaded with VEGF were successfully fabricated by using a new wheel spinning technique which parameters were optimized. We have demonstrated that the release of VEGF is controllable by engineering the Alg/SF composite fibers with different loading concentration and SF materials with different structure features. The mechanisms and impacting factors for VEGF release behavior from SF morphology and spinning solution concentration have been identified by analyzing the DoE results, indicating that Alg/SF composite fibers with different VEGF release rates could be utilized to develop new approaches to control the wound healing process.

Declaration of competing interest

The authors declare that they have no known competing financial interests or personal relationships that could have appeared to influence the study reported in this article.

Supporting Information

The Supporting Information is available free of charge at XXXXXX

Author Contributions

Jun Song and **Zhongda Chen** contributed equally to this work. All authors have read and approved the final manuscript.

Acknowledgments

Zhongda Chen and Jun Song acknowledge Mr. Luis Larrea Murillo who did the cell work of this project and financially supported by EPSRC & MRC Centre for Doctoral Training (CDT) program in the Division of Evolution and Genomic Sciences, The University of Manchester. The authors would like to express thanks to the support from Dr. Louise Carney and the Electron Microscopy Center and XRD suite in Department of Materials, The University of Manchester. SPSS, Minitab, and MATLAB were used under the license in The University of Manchester.

References

[1] P. Martin, R. Nunan, Cellular and molecular mechanisms of repair in acute and chronic wound healing, Br. J. Dermatol. 173 (2015) 370–378. https://doi.org/10.1111/bjd.13954.

[2] S. WERNER, R. GROSE, Regulation of Wound Healing by Growth Factors and Cytokines, Physiol. Rev. 83 (2003) 835–870. https://doi.org/10.1152/physrev.2003.83.3.835.

[3] J.S. Boateng, K.H. Matthews, H.N.E. Stevens, G.M. Eccleston, Wound Healing Dressings and Drug Delivery Systems: A Review, J. Pharm. Sci. 97 (2008) 2892–2923. https://doi.org/10.1002/jps.21210.

[4] P. Martin, Wound Healing--Aiming for Perfect Skin Regeneration, Science (80-.). 276 (1997) 75–81. https://doi.org/10.1126/science.276.5309.75.

[5] A.J. Rufaihah, N.A. Johari, S.R. Vaibavi, M. Plotkin, D.T. Di Thien, T. Kofidis, D. Seliktar, Dual delivery of VEGF and ANG-1 in ischemic hearts using an injectable hydrogel, Acta Biomater. 48 (2017) 58–67. https://doi.org/10.1016/j.actbio.2016.10.013.

[6] N. Kamaly, B. Yameen, J. Wu, O.C. Farokhzad, Degradable Controlled-Release Polymers and Polymeric Nanoparticles: Mechanisms of Controlling Drug Release, Chem. Rev. 116 (2016) 2602–2663. https://doi.org/10.1021/acs.chemrev.5b00346.

[7] W. Xu, Q. Song, J.-F. Xu, M.J. Serpe, X. Zhang, Supramolecular Hydrogels Fabricated from Supramonomers: A Novel Wound Dressing Material, ACS Appl. Mater. Interfaces. 9 (2017) 11368–11372. https://doi.org/10.1021/acsami.7b02850.

[8] X. Qiu, J. Zhang, L. Cao, Q. Jiao, J. Zhou, L. Yang, H. Zhang, Y. Wei, Antifouling Antioxidant Zwitterionic Dextran Hydrogels as Wound Dressing Materials with Excellent Healing Activities, ACS Appl. Mater. Interfaces. 13 (2021) 7060–7069. https://doi.org/10.1021/acsami.0c17744.

[9] M. Umar, A. Ullah, H. Nawaz, T. Areeb, M. Hashmi, D. Kharaghani, K.O. Kim, I.S. Kim, Wet-spun bi-component alginate based hydrogel fibers: Development and in-vitro evaluation as a potential moist wound care dressing, Int. J. Biol. Macromol. 168 (2021) 601–610. https://doi.org/10.1016/j.ijbiomac.2020.12.088.

[10] A. Vijayan, S. A., G.S.V. Kumar, PEG grafted chitosan scaffold for dual growth factor delivery for enhanced wound healing, Sci. Rep. 9 (2019) 19165. https://doi.org/10.1038/s41598-019-55214-7.

[11] J. Xia, H. Zhang, F. Yu, Y. Pei, X. Luo, Superclear, Porous Cellulose Membranes with Chitosan-Coated Nanofibers for Visualized Cutaneous Wound Healing Dressing, ACS Appl. Mater. Interfaces. 12 (2020) 24370–24379. https://doi.org/10.1021/acsami.0c05604.

[12] J. Hu, S. Chen, A review of actively moving polymers in textile applications, J. Mater. Chem. 20 (2010) 3346. https://doi.org/10.1039/b922872a.

[13]A. Joshi, Z. Xu, Y. Ikegami, K. Yoshida, Y. Sakai, A. Joshi, T. Kaur, Y. Nakao, Y. Yamashita, H. Baba, S. Aishima, N. Singh, H. Ijima, Exploiting synergistic effect of externally loaded bFGF and endogenous growth factors for accelerated wound healing using heparin functionalized PCL/gelatin co-spun nanofibrous patches, Chem. Eng. J. 404 (2021) 126518. https://doi.org/10.1016/j.cej.2020.126518.

[14] D.P. Tong, Process for the production of alginate fibre material and products made therefrom, US4562110A, 1985. https://patents.google.com/patent/US4562110A/en.

[15] Y.-M. Xia, Z.-D. Chen, Y. Li, Mechanical Properties Tests of Wet-spun Pure Alginate Filament and Yarns, in: Text. Bioeng. Informatics Symp. Proc. 2018 - 11th Text. Bioeng. Informatics Symp. TBIS 2018, 2018: pp. 37–46.

[16] Y. Luo, Y. Li, X. Qin, Q. Wa, 3D printing of concentrated alginate/gelatin scaffolds with homogeneous nano apatite coating for bone tissue engineering, Mater. Des. 146 (2018) 12–19. https://doi.org/10.1016/j.matdes.2018.03.002.

[17] L.-B. Jiang, S.-L. Ding, W. Ding, D.-H. Su, F.-X. Zhang, T.-W. Zhang, X.-F. Yin, L. Xiao, Y.-L. Li, F.-L. Yuan, J. Dong, Injectable sericin based nanocomposite hydrogel for multi-modal imaging-guided immunomodulatory bone regeneration, Chem. Eng. J. 418 (2021) 129323. https://doi.org/10.1016/j.cej.2021.129323.

[18] Z. Cao, X. Chen, J. Yao, L. Huang, Z. Shao, The preparation of regenerated silk fibroin microspheres, Soft Matter. 3 (2007) 910. https://doi.org/10.1039/b703139d.

[19] J. Song, X.-Q. Wang, J.-S. Li, Preparation of the silk fibroin 3D scaffolds with large pore sizes and high interconnectivity, in: Text. Bioeng. Informatics Symp. Proc. 2018 - 11th Text. Bioeng. Informatics Symp. TBIS 2018, 2018.

[20] J. Song, Z. Chen, L.L. Murillo, D. Tang, C. Meng, X. Zhong, T. Wang, J. Li, Hierarchical porous silk fibroin/poly(L-lactic acid) fibrous membranes towards vascular scaffolds, Int. J. Biol. Macromol. 166 (2021) 1111–1120. https://doi.org/10.1016/j.ijbiomac.2020.10.266.

[21] Z. Chen, J. Song, Y. Xia, Y. Jiang, L.L. Murillo, O. Tsigkou, T. Wang, Y. Li, High strength and strain alginate fibers by a novel wheel spinning technique for knitting stretchable and

biocompatible wound-care materials, Mater. Sci. Eng. C. 127 (2021) 112204. https://doi.org/10.1016/j.msec.2021.112204.

[22] N. Sarlak, M.A.F. Nejad, S. Shakhesi, K. Shabani, Effects of electrospinning parameters on titanium dioxide nanofibers diameter and morphology: An investigation by Box–Wilson central composite design (CCD), Chem. Eng. J. 210 (2012) 410–416. https://doi.org/10.1016/j.cej.2012.08.087.

[23] D.N. Rockwood, R.C. Preda, T. Yücel, X. Wang, M.L. Lovett, D.L. Kaplan, Materials fabrication from Bombyx mori silk fibroin, Nat. Protoc. 6 (2011) 1612–1631. https://doi.org/10.1038/nprot.2011.379.

[24] T. Asakura, K. Ohgo, T. Ishida, P. Taddei, P. Monti, R. Kishore, Possible Implications of Serine and Tyrosine Residues and Intermolecular Interactions on the Appearance of Silk I Structure of Bombyx m ori Silk Fibroin-Derived Synthetic Peptides: High-Resolution 13 C Cross-Polarization/Magic-Angle Spinning NMR Study, Biomacromolecules. 6 (2005) 468–474. https://doi.org/10.1021/bm049487k.

[25] J. Yan, G. Zhou, D.P. Knight, Z. Shao, X. Chen, Wet-Spinning of Regenerated Silk Fiber from Aqueous Silk Fibroin Solution: Discussion of Spinning Parameters, Biomacromolecules. 11 (2010) 1–5. https://doi.org/10.1021/bm900840h.

[26] D.M. Phillips, L.F. Drummy, R.R. Naik, H.C. De Long, D.M. Fox, P.C. Trulove, R.A. Mantz, Regenerated silk fiber wet spinning from an ionic liquid solution, J. Mater. Chem. 15 (2005) 4206. https://doi.org/10.1039/b510069k.

[27] F. Zhang, Q. Lu, X. Yue, B. Zuo, M. Qin, F. Li, D.L. Kaplan, X. Zhang, Regeneration of high-quality silk fibroin fiber by wet spinning from CaCl2 –formic acid solvent, Acta Biomater. 12 (2015) 139–145. https://doi.org/10.1016/j.actbio.2014.09.045.

[28] Q. Liu, K.K. Parker, A viscoelastic beam theory of polymer jets with application to rotary jet spinning, Extrem. Mech. Lett. 25 (2018) 37–44. https://doi.org/10.1016/j.eml.2018.10.005.

[29] L.W. Schwartz, R.V. Roy, Theoretical and numerical results for spin coating of viscous liquids, Phys. Fluids. 16 (2004) 569–584. https://doi.org/10.1063/1.1637353.

[30] Y. Wu, C. Li, F. Fan, J. Liang, Z. Yang, X. Wei, S. Chen, PVAm Nanofibers Fabricated by Rotary Jet Wet Spinning and Applied to Bisphenol A Recognition, ACS Omega. 4 (2019) 21361–21369. https://doi.org/10.1021/acsomega.9b02964.

[31] W. Mackie, S. Perez, R. Rizzo, F. Taravel, M. Vignon, Aspects of the conformation of polyguluronate in the solid state and in solution, Int. J. Biol. Macromol. 5 (1983) 329–341. https://doi.org/10.1016/0141-8130(83)90056-9.

[32] M.B. Stewart, S.R. Gray, T. Vasiljevic, J.D. Orbell, The role of poly-M and poly-GM sequences in the metal-mediated assembly of alginate gels, Carbohydr. Polym. 112 (2014) 486–493. https://doi.org/10.1016/j.carbpol.2014.06.001.

[33] M. Farokhi, F. Mottaghitalab, Y. Fatahi, A. Khademhosseini, D.L. Kaplan, Overview of Silk Fibroin Use in Wound Dressings, Trends Biotechnol. 36 (2018) 907–922. https://doi.org/10.1016/j.tibtech.2018.04.004.

[34] W. Chen, F. Li, L. Chen, Y. Zhang, T. Zhang, T. Wang, Fast self-assembly of microporous silk fibroin membranes on liquid surface, Int. J. Biol. Macromol. 156 (2020) 633–639. https://doi.org/https://doi.org/10.1016/j.ijbiomac.2020.04.053.

[35] B. Liu, B.Z. Tang, Aggregation-Induced Emission: More Is Different, Angew. Chemie Int. Ed. 59 (2020) 9788–9789. https://doi.org/10.1002/anie.202005345.

[36] P.F. Ng, K.I. Lee, S. Meng, J. Zhang, Y. Wang, B. Fei, Wet Spinning of Silk Fibroin-Based Core–Sheath Fibers, ACS Biomater. Sci. Eng. 5 (2019) 3119–3130. https://doi.org/10.1021/acsbiomaterials.9b00275.

[37] G. Song, C. Zheng, Y. Liu, M. Ding, P. Liu, J. Xu, W. Wang, J. Wang, In vitro extracellular matrix deposition by vascular smooth muscle cells grown in fibroin scaffolds, and the regulation of TGF-β1, Mater. Des. 199 (2021) 109428. https://doi.org/10.1016/j.matdes.2020.109428.

[38] N. Yin, Y. Han, H. Xu, Y. Gao, T. Yi, J. Yao, L. Dong, D. Cheng, Z. Chen, VEGF-conjugated alginate hydrogel prompt angiogenesis and improve pancreatic islet engraftment and function in type 1 diabetes, Mater. Sci. Eng. C. 59 (2016) 958–964. https://doi.org/10.1016/j.msec.2015.11.009.

[39] Y. Zhang, J. Huang, L. Huang, Q. Liu, H. Shao, X. Hu, L. Song, Silk Fibroin-Based Scaffolds with Controlled Delivery Order of VEGF and BDNF for Cavernous Nerve Regeneration, ACS Biomater. Sci. Eng. 2 (2016) 2018–2025. https://doi.org/10.1021/acsbiomaterials.6b00436.

[40] N. Hassani Besheli, S. Damoogh, B. Zafar, F. Mottaghitalab, H. Motasadizadeh, F. Rezaei, M.A. Shokrgozar, M. Farokhi, Preparation of a Codelivery System Based on Vancomycin/Silk Scaffold Containing Silk Nanoparticle Loaded VEGF, ACS Biomater. Sci. Eng. 4 (2018) 2836–2846. https://doi.org/10.1021/acsbiomaterials.8b00149.

[41] M. Farokhi, F. Mottaghitalab, M.A. Shokrgozar, J. Ai, J. Hadjati, M. Azami, Bio-hybrid silk fibroin/calcium phosphate/PLGA nanocomposite scaffold to control the delivery of vascular endothelial growth factor, Mater. Sci. Eng. C. 35 (2014) 401–410. https://doi.org/10.1016/j.msec.2013.11.023.

[42] Y. Wu, T. Chang, W. Chen, X. Wang, J. Li, Y. Chen, Y. Yu, Z. Shen, Q. Yu, Y. Zhang, Release of VEGF and BMP9 from injectable alginate based composite hydrogel for treatment of myocardial infarction, Bioact. Mater. 6 (2021) 520–528. https://doi.org/10.1016/j.bioactmat.2020.08.031.

[43] G. Marchioli, A. Di Luca, E. de Koning, M. Engelse, C.A. Van Blitterswijk, M. Karperien, A.A. Van Apeldoorn, L. Moroni, Hybrid Polycaprolactone/Alginate Scaffolds Functionalized with VEGF to Promote de Novo Vessel Formation for the Transplantation of Islets of Langerhans, Adv. Healthc. Mater. 5 (2016) 1606–1616. https://doi.org/10.1002/adhm.201600058.

[44] R. Zhang, L. Xie, H. Wu, T. Yang, Q. Zhang, Y. Tian, Y. Liu, X. Han, W. Guo, M. He, S. Liu, W. Tian, Alginate/laponite hydrogel microspheres co-encapsulating dental pulp stem cells and VEGF for endodontic regeneration, Acta Biomater. 113 (2020) 305–316. https://doi.org/10.1016/j.actbio.2020.07.012.

[45] A.M. Craciun, L. Mititelu Tartau, M. Pinteala, L. Marin, Nitrosalicyl-imine-chitosan hydrogels based drug delivery systems for long term sustained release in local therapy, J. Colloid Interface Sci. 536 (2019) 196–207. https://doi.org/10.1016/j.jcis.2018.10.048.

[46] D. Ailincai, M. Agop, I.C. Marinas, A. Zala, S.A. Irimiciuc, L. Dobreci, T.-C. Petrescu, C. Volovat, Theoretical model for the diclofenac release from PEGylated chitosan hydrogels, Drug Deliv. 28 (2021) 261–271. https://doi.org/10.1080/10717544.2021.1876181.

[47] J.F. Dye, From Secondary Intent to Accelerated Regenerative Healing: Emergence of the Bio-intelligent Scaffold Vasculogenic Strategy for Skin Reconstruction, in: Vasc. Tissue Eng. Regen. Med., Springer International Publishing, Cham, 2020: pp. 1–68. https://doi.org/10.1007/978-3-319-21056-8_20-1.

[48] C. Chen, Y. Wang, D. Zhang, X. Wu, Y. Zhao, L. Shang, J. Ren, Y. Zhao, Natural polysaccharide based complex drug delivery system from microfluidic electrospray for wound healing, Appl. Mater. Today. 23 (2021) 101000. https://doi.org/10.1016/j.apmt.2021.101000.

[49] Y. Guo, J. Guan, H. Peng, X. Shu, L. Chen, H. Guo, Tightly adhered silk fibroin coatings on Ti6Al4V biometals for improved wettability and compatible mechanical properties, Mater. Des. 175 (2019) 107825. https://doi.org/10.1016/j.matdes.2019.107825.

Supplementary Information

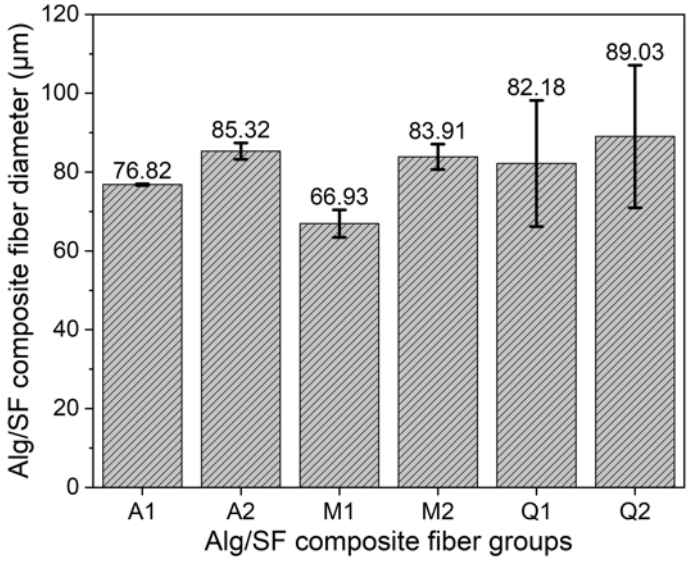

Fig. 5.8 Freeze-dried Alg/SF composite fiber diameter for alginate, Alg/SF microsphere and aqueous with different wheel spun solution concentration samples.

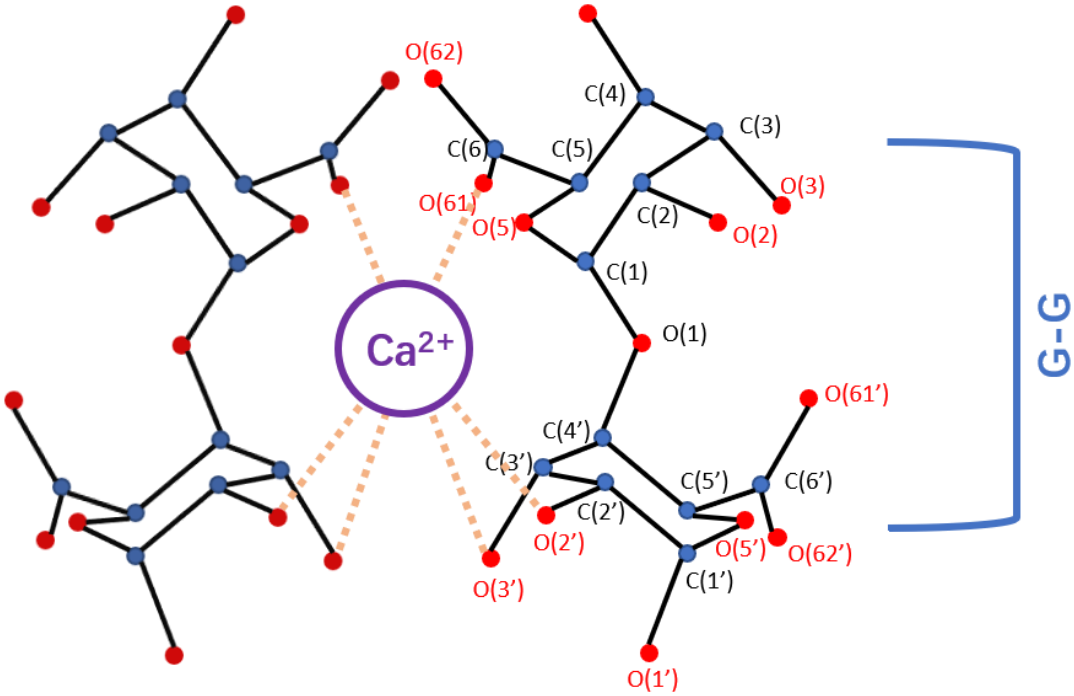

Fig. 5.9 The schematic diagram of alginate cross-linkage of lateral egg-box dimers.

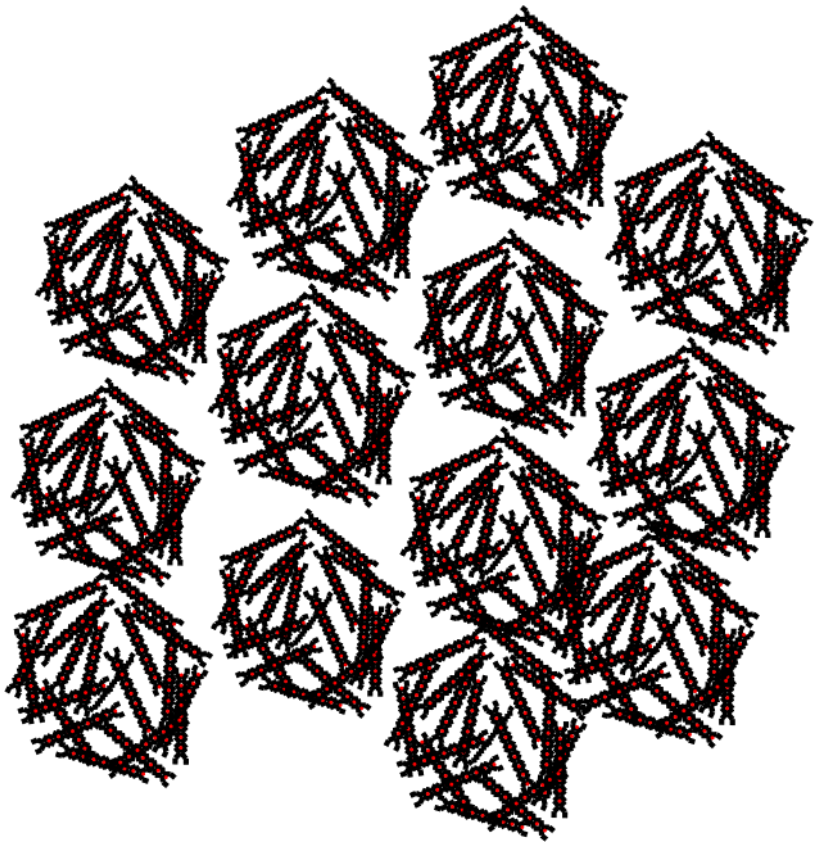

Fig. 5.10 The schematic diagram of agglomeration of alginate egg-box multimers.

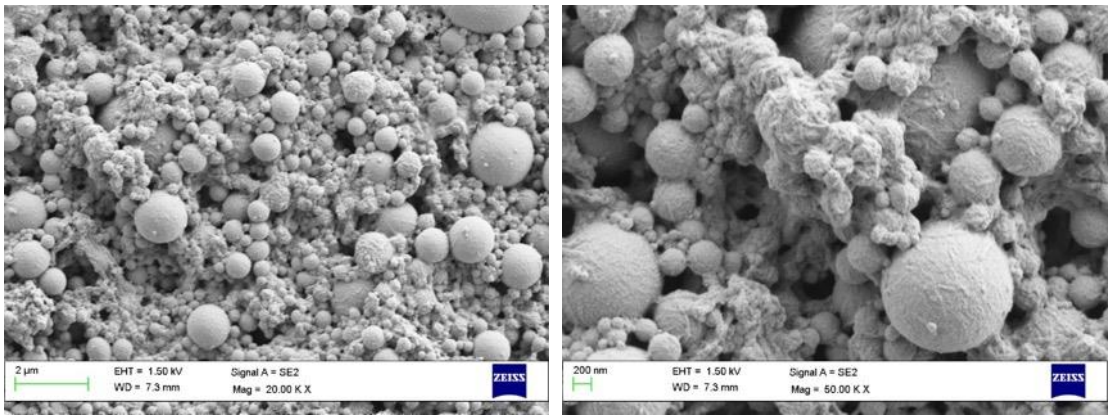

Fig. 5.11 SEM images of silk fibroin microspheres prepared and used in this study.

General Factorial Regression: Load rate versus Morphology, Concentration

Factor Information

Factor	Levels	Values
Morphology	3	1, 2, 3
Concentration	2	1, 2

Analysis of Variance

Source	DF	Adj SS	Adj MS	F-Value	P-Value
Model	5	107.11	21.421	3.14	0.033
Linear	3	96.33	32.109	4.71	0.013
Morphology	2	42.78	21.388	3.14	0.068
Concentration	1	53.55	53.551	7.86	0.012
2-Way Interactions	2	10.78	5.390	0.79	0.469
Morphology*Concentration	2	10.78	5.390	0.79	0.469
Error	18	122.65	6.814		
Total	23	229.76			

Model Summary

S	R-sq	R-sq(adj)	R-sq(pred)
2.61032	46.62%	31.79%	5.10%

Fig. 5.12 ANOVA table for the results of loading efficiency.

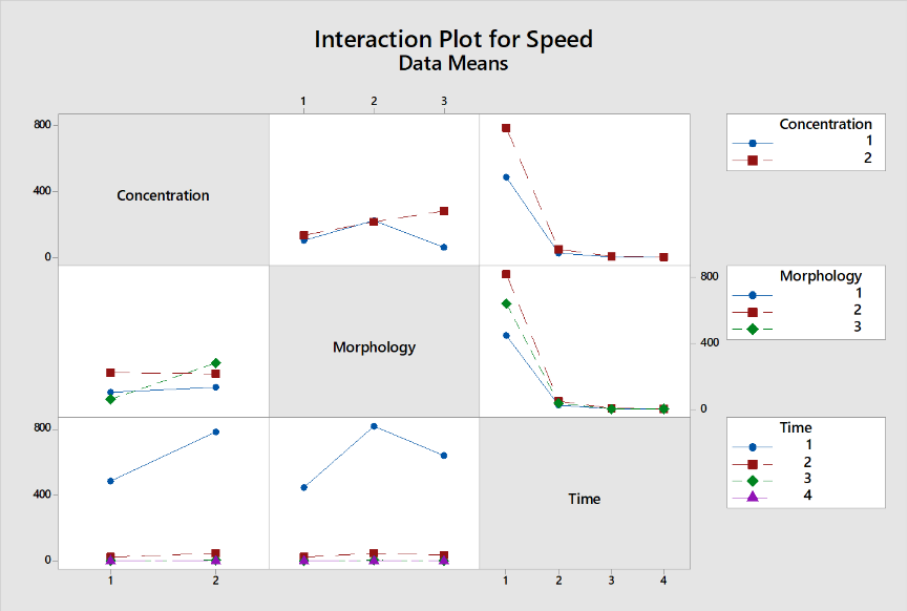

General Factorial Regression: Speed versus Concentration, Morphology, Time

Factor Information

Factor	Levels	Values
Concentration	2	1, 2
Morphology	3	1, 2, 3
Time	4	1, 2, 3, 4

Analysis of Variance

Source	DF	Adj SS	Adj MS	F-Value	P-Value
Model	23	6669824	289992	451.96	0.000
Linear	6	5486215	914369	1425.07	0.000
Concentration	1	119334	119334	185.99	0.000
Morphology	2	120386	60193	93.81	0.000
Time	3	5246494	1748831	2725.60	0.000
2-Way Interactions	11	758744	68977	107.50	0.000
Concentration*Morphology	2	176224	88112	137.33	0.000
Concentration*Time	3	283565	94522	147.31	0.000
Morphology*Time	6	298955	49826	77.65	0.000
3-Way Interactions	6	424865	70811	110.36	0.000
Concentration*Morphology*Time	6	424865	70811	110.36	0.000
Error	48	30798	642		
Total	71	6700622			

Model Summary

S	R-sq	R-sq(adj)	R-sq(pred)
25.3304	99.54%	99.32%	98.97%

Fig. 5.13 The main effect plots and ANOVA table of VEGF release speed via design of experiments for Alg/SF composite fibers.

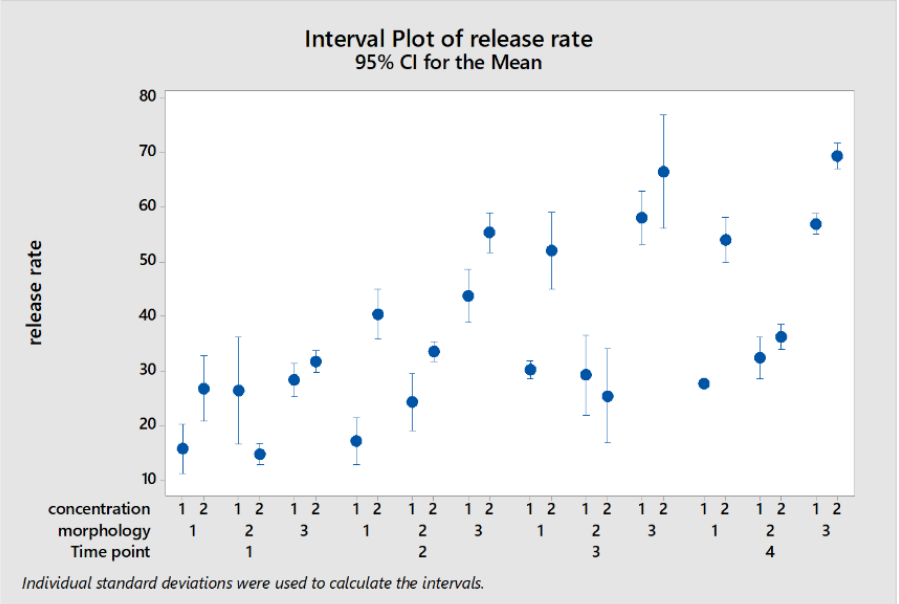

General Factorial Regression: release rate versus Time point, morphology, concentration

Factor Information

Factor	Levels	Values
Time point	4	1, 2, 3, 4
morphology	3	1, 2, 3
concentration	2	1, 2

Analysis of Variance

Source	DF	Adj SS	Adj MS	F-Value	P-Value
Model	23	17566.9	763.78	177.50	0.000
Linear	6	14332.1	2388.69	555.14	0.000
Time point	3	5353.9	1784.63	414.75	0.000
morphology	2	7291.2	3645.61	847.25	0.000
concentration	1	1687.0	1687.03	392.07	0.000
2-Way Interactions	11	3139.2	285.38	66.32	0.000
Time point*morphology	6	1224.8	204.14	47.44	0.000
Time point*concentration	3	555.4	185.12	43.02	0.000
morphology*concentration	2	1359.0	679.48	157.91	0.000
3-Way Interactions	6	95.6	15.94	3.70	0.004
Time point*morphology*concentration	6	95.6	15.94	3.70	0.004
Error	48	206.5	4.30		
Total	71	17773.4			

Model Summary

S	R-sq	R-sq(adj)	R-sq(pred)
2.07434	98.84%	98.28%	97.39%

Fig. 5.14 The main effects and ANOVA table of VEGF release rate via design of experiments for Alg/SF composite fibers.

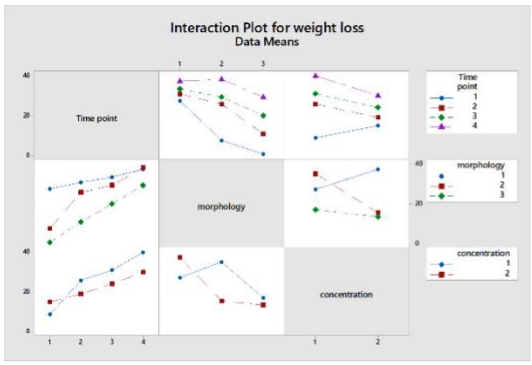

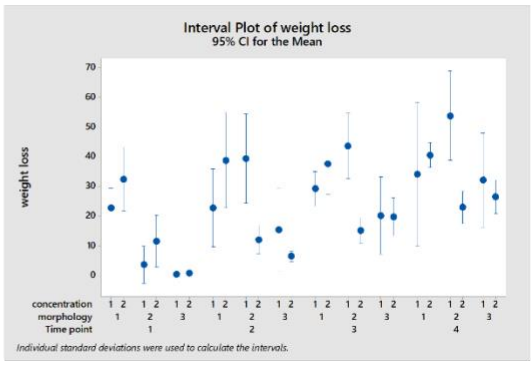

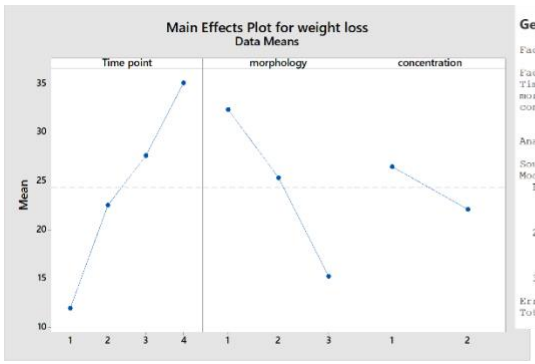

General Factorial Regression: weight loss versus Time point, morphology, concentration

Factor Information

Factor	Levels	Values
Time point	4	1, 2, 3, 4
morphology	3	1, 2, 3
concentration	2	1, 2

Analysis of Variance

Source	DF	Adj SS	Adj MS	F-Value	P-Value
Model	23	14305.8	621.99	33.05	0.000
Linear	6	8988.2	1498.03	79.59	0.000
Time point	3	5095.7	1698.58	90.25	0.000
morphology	2	3547.6	1773.78	94.25	0.000
concentration	1	344.9	344.88	18.32	0.000
2-Way Interactions	11	4296.3	390.57	20.75	0.000
Time point*morphology	6	956.0	159.34	8.47	0.000
Time point*concentration	3	678.1	226.05	12.01	0.000
morphology*concentration	2	2662.1	1331.07	70.72	0.000
3-Way Interactions	6	1021.3	170.22	9.04	0.000
Time point*morphology*concentration	6	1021.3	170.22	9.04	0.000
Error	48	903.4	18.82		
Total	71	15209.2			

Fig. 5.15 The main effect plots, results, and ANOVA table of composite fiber weight loss via design of experiments for wheel spun Alg/SF composite fibers.

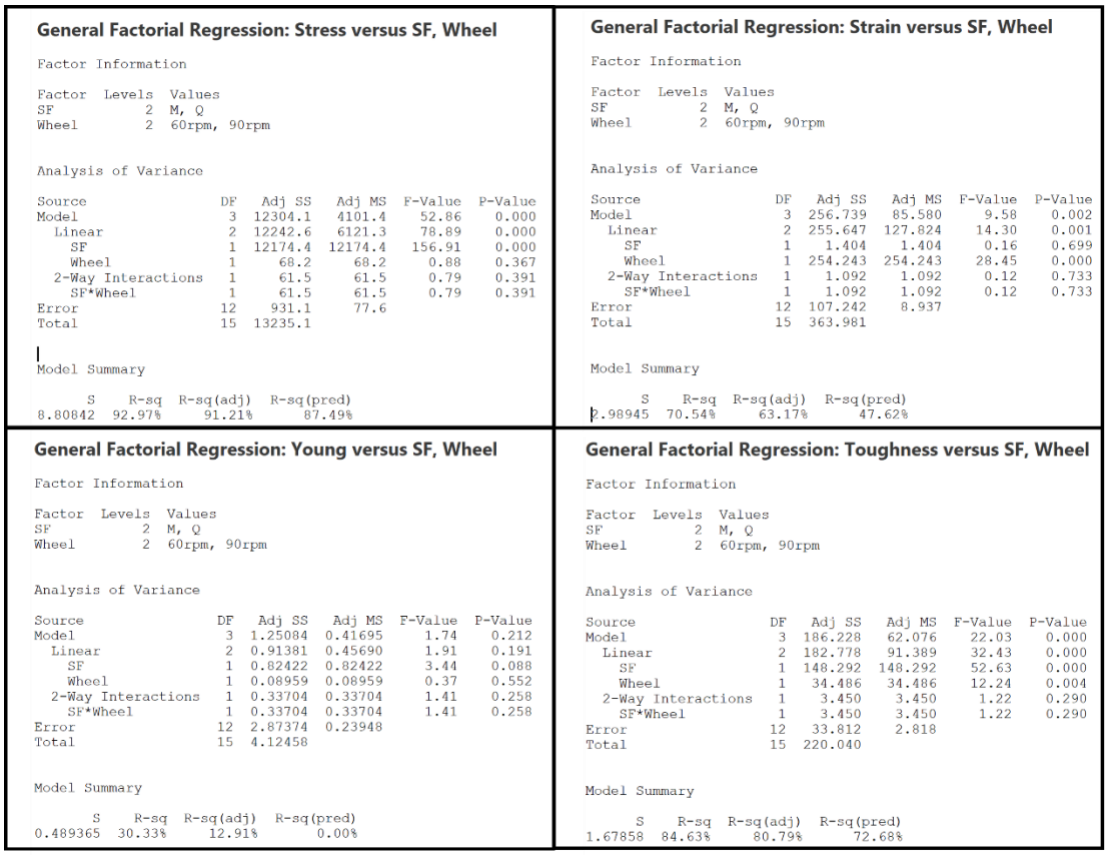

General Factorial Regression: Stress versus SF, Wheel

Factor Information

Factor	Levels	Values
SF	2	M, Q
Wheel	2	60rpm, 90rpm

Analysis of Variance

Source	DF	Adj SS	Adj MS	F-Value	P-Value
Model	3	12304.1	4101.4	52.86	0.000
Linear	2	12242.6	6121.3	78.89	0.000
SF	1	12174.4	12174.4	156.91	0.000
Wheel	1	68.2	68.2	0.88	0.367
2-Way Interactions	1	61.5	61.5	0.79	0.391
SF*Wheel	1	61.5	61.5	0.79	0.391
Error	12	931.1	77.6		
Total	15	13235.1			

Model Summary

S	R-sq	R-sq(adj)	R-sq(pred)
8.80842	92.97%	91.21%	87.49%

General Factorial Regression: Strain versus SF, Wheel

Factor Information

Factor	Levels	Values
SF	2	M, Q
Wheel	2	60rpm, 90rpm

Analysis of Variance

Source	DF	Adj SS	Adj MS	F-Value	P-Value
Model	3	256.739	85.580	9.58	0.002
Linear	2	255.647	127.824	14.30	0.001
SF	1	1.404	1.404	0.16	0.699
Wheel	1	254.243	254.243	28.45	0.000
2-Way Interactions	1	1.092	1.092	0.12	0.733
SF*Wheel	1	1.092	1.092	0.12	0.733
Error	12	107.242	8.937		
Total	15	363.981			

Model Summary

S	R-sq	R-sq(adj)	R-sq(pred)
2.98945	70.54%	63.17%	47.62%

General Factorial Regression: Young versus SF, Wheel

Factor Information

Factor	Levels	Values
SF	2	M, Q
Wheel	2	60rpm, 90rpm

Analysis of Variance

Source	DF	Adj SS	Adj MS	F-Value	P-Value
Model	3	1.25084	0.41695	1.74	0.212
Linear	2	0.91381	0.45690	1.91	0.191
SF	1	0.82422	0.82422	3.44	0.088
Wheel	1	0.08959	0.08959	0.37	0.552
2-Way Interactions	1	0.33704	0.33704	1.41	0.258
SF*Wheel	1	0.33704	0.33704	1.41	0.258
Error	12	2.87374	0.23948		
Total	15	4.12458			

Model Summary

S	R-sq	R-sq(adj)	R-sq(pred)
0.489365	30.33%	12.91%	0.00%

General Factorial Regression: Toughness versus SF, Wheel

Factor Information

Factor	Levels	Values
SF	2	M, Q
Wheel	2	60rpm, 90rpm

Analysis of Variance

Source	DF	Adj SS	Adj MS	F-Value	P-Value
Model	3	186.228	62.076	22.03	0.000
Linear	2	182.778	91.389	32.43	0.000
SF	1	148.292	148.292	52.63	0.000
Wheel	1	34.486	34.486	12.24	0.004
2-Way Interactions	1	3.450	3.450	1.22	0.290
SF*Wheel	1	3.450	3.450	1.22	0.290
Error	12	33.812	2.818		
Total	15	220.040			

Model Summary

S	R-sq	R-sq(adj)	R-sq(pred)
1.67858	84.63%	80.79%	72.68%

Fig. 5.16 The ANOVA tables of mechanical properties of wheel spun Alg/SF fibers.

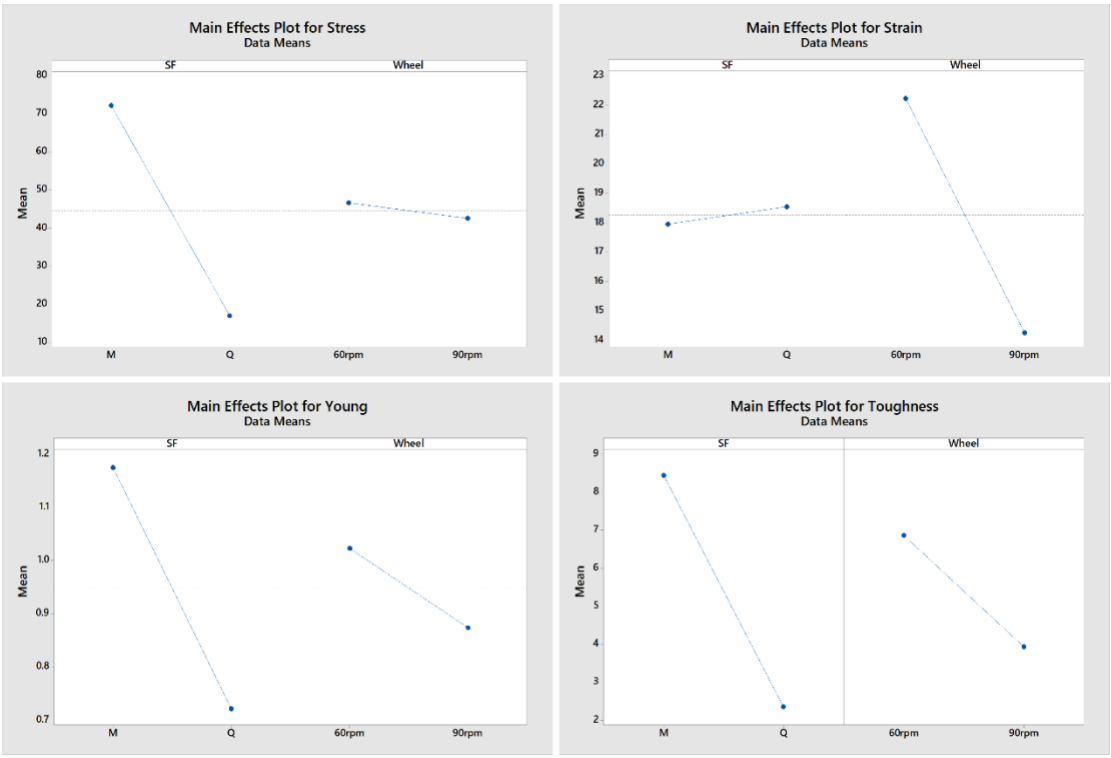

Fig. 5.17 The main effects plots of mechanical properties of wheel spun Alg/SF fibers.

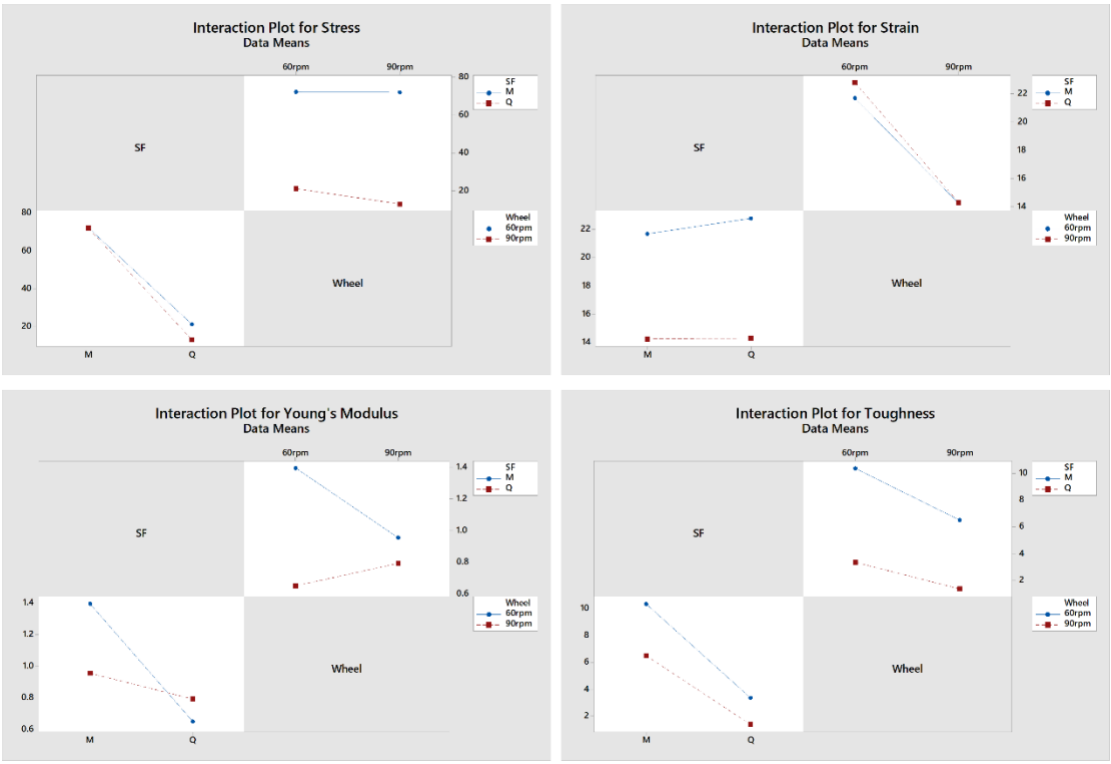

Fig. 5. 18 The DoE interaction plots of mechanical properties of wheel spun Alg/SF fibers.

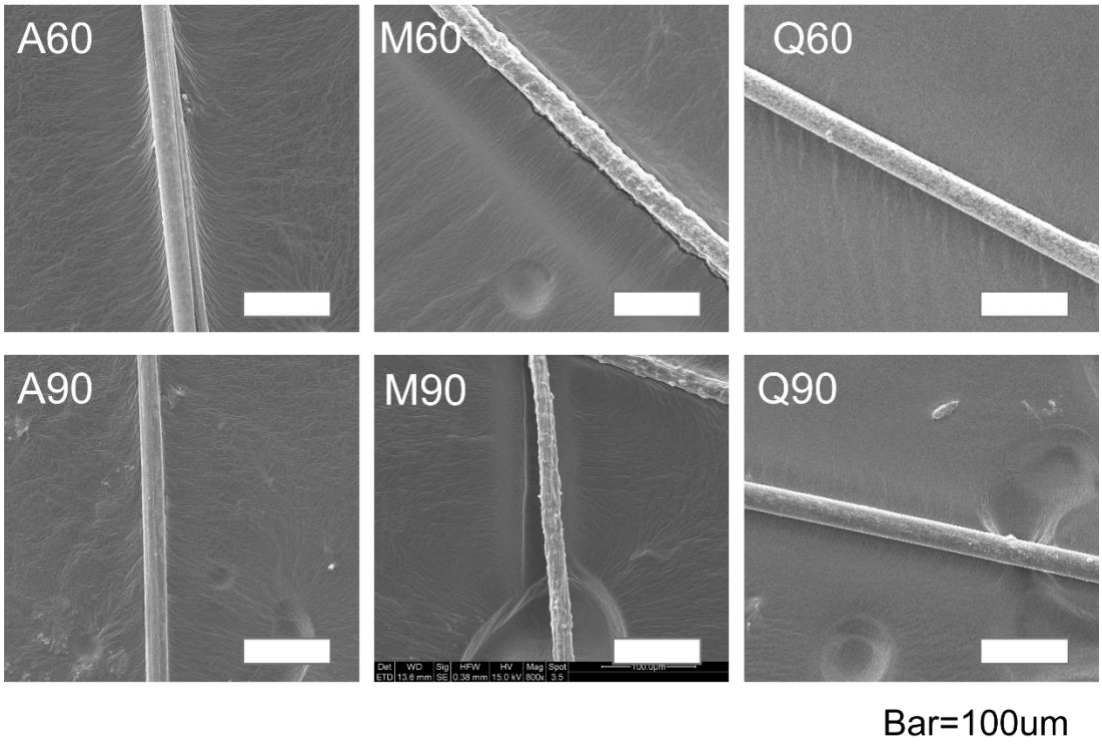

Fig. 5.19 SEM images of dry wheel spun Alg/SF fibers for tensile tests.

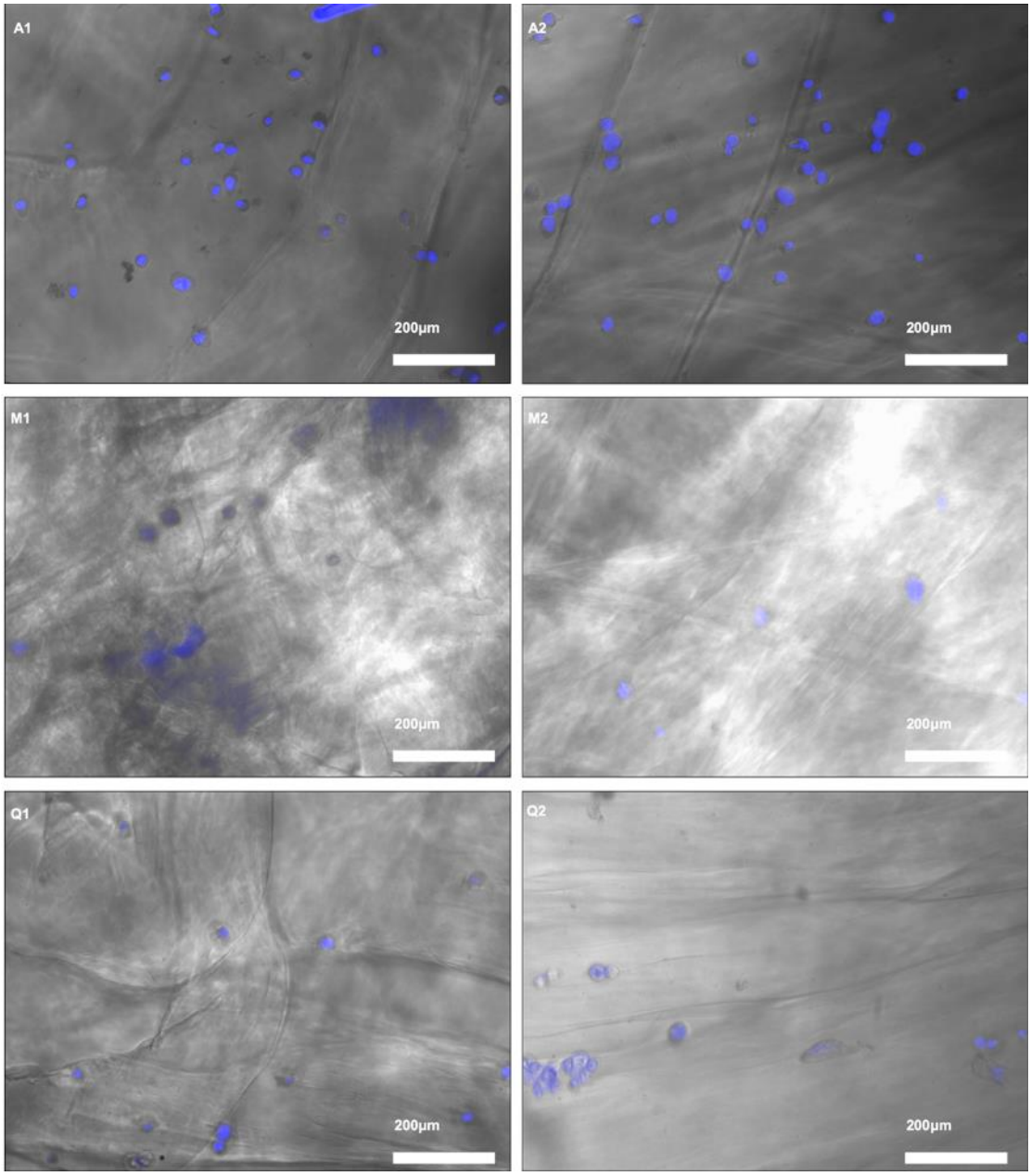

Fig. 5.20 Overview phase contrast light microscopy images of HCAEC cells on Alg/SF composite fibers. The cytomembrane was stained blue by DAPI assay. The composite fiber could also be observed in these images. It could be observed on pure alginate fiber that certain cells were attached easily on the alginate surface. HCAECs maintained round-shape morphology on Alg/SF microsphere composite fibers. The cells had spreading morphology on Alg/SF aqueous specimens, but the cell counts seemed less than on that of Alg/SF microsphere specimens. The densities for different concentrations fibers had little differences.

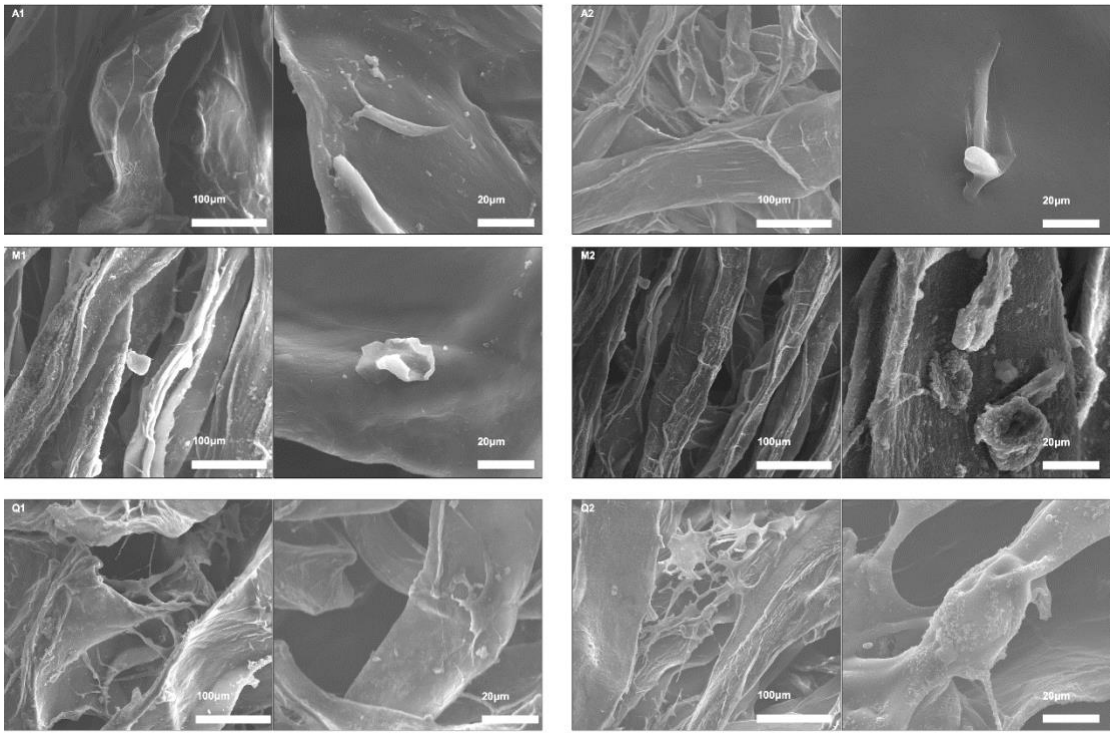

Fig. 5.21 Cell morphology and adhesion on six groups of Alg/SF composite fibers by SEM with different magnifications.

Chapter 6 Conclusion and Future Works

6.1 Summary

The project described in this thesis focuses on the design and development of the wheel-spinning technique and the characterization and assessment of wheel-spun fibres and their related wound-care applications.

Firstly, a review of the literature on the materials (sodium alginate and silk fibroin), the wet-spinning technique, the process of wound healing, and the types and structure of wound dressings was presented in Chapter 2, in turn lending this project a framework and a foundation.

Then, in Chapter 3, the fabrication and design of the wheel-spinning machine (WSM) was discussed, including the analysis of the force that the fibre was subject to during the spinning process, the drawing effect given by each design for the WSM set-ups, and the twisting effect given by WSM Set-up B. Moreover, the fibre derived from alginate in the case of each WSM design with various parameters was characterized by using Raman, FTIR, SEM and tensile machine approaches in order to demonstrate the twisting and drawing effect of wheel-spun fibres from various set-ups.

After that, in Chapter 4, the alginate fibres made with WSM Set-up A were collected and sketchy-twisted into four or eight strands of yarns, then fabricated as knitting fabric for use as generic wound-dressing material. The advantage of wheel-spun alginate fibre is obvious, given its higher tensile strength and strain. Indeed, a mini-review to compare each kind of alginate-based fibre recently indicated that wheel-spun alginate fibre possesses a significantly higher tensile strength and strain, compared to other fibres, resulting in a higher breaking energy and

a capacity to knit the fibre into fabric using a hand-knitting machine. During the study, it was discovered that needle size and alginate concentration can change the fibre's tensile properties. Meanwhile, it was also found that the inner morphology of alginate fibre consists of numerous aggregated nanospheres with diameters around 30-50 nm. Based on the "egg-box" theory, it can be understood as an aggregation of "egg-box" dimers. This theory can help explain tensile property changes while varying the spinning parameters. Furthermore, the knitting structure of alginate fabric offers more flexibility, softness and elastic properties compared with normal non-woven alginate wound dressing. The subsequent biodegradation and biocompatibility test confirmed its suitability as wound-dressing material.

In Chapter 5, alginate-silk fibroin composite fibre was made using WSM Set-up A with a 30G (inner diameter 0.159 mm) needle, with the collected fibre freeze-dried into a non-woven mat. Vascular endothelial growth factor (VEGF) was enclosed in the fibre by mixing with extrusion solution in advance. Benefiting from a low-temperature and aqueous environment during the fibre-spinning process, the VEGF remained bioactive by directly being added to the solution. In this chapter, two types of silk fibroin with different morphologies were introduced, namely, aqueous solution and microspheres, together with controlling the solution concentration, in order to vary the VEGF release behaviour by changing the fibre's inner structure. The VEGF release rate was found to be suitable for an actual wound where all the VEGF must be released in less than 24 h; this finding has not been reported by previous research. The release rate was determined by using an arctangent function, after which the instantaneous release speed was calculated to further understand the fibre's properties. Finally, it was established that release

behaviour and degradation behaviour can be controlled by silk fibroin morphology and spinning-solution concentration, in line with “egg-box” theory as discussed in Chapter 4.

In summary, as an interdisciplinary project, this work includes knowledge and technologies from biomaterial, textile and biomedical engineering. In turn, it has developed two types of wound-care materials for different types of wounds, with the use of wheel-spun fibres.

6.2 Limitations and future work

There are several aspects that can be explored in more depth in the future, as listed below:

(1) The WSM design could include the following optimizations:

   a) The angle and shape of the blend in the case of WSM Set-up A needs further optimization;

   b) The construction of the rotation part of WSM Set-up B requires further exploration;

   c) How to control the twisting effect via each parameter during the fibre-spinning process should be subject to systematic investigation.

(2) The wheel-spun alginate-silk fibroin fibre could be applied to the controlled release of epidermal growth factor and transforming growth factor-beta (TGF-β). As such, how this could facilitate the development of a multi-functional wound dressing needs further study.

(3) The remaining bioactivity of the growth factors enclosed in the fibre needs systematic investigation.

(4) Cell works and animal studies in the case of controlled-release fibre require further evaluation.